PERTURBATION SPECTROSCOPY OF THE ARGON ION LASER

Malcolm H. Dunn

A Thesis Submitted for the Degree of PhD
at the
University of St Andrews

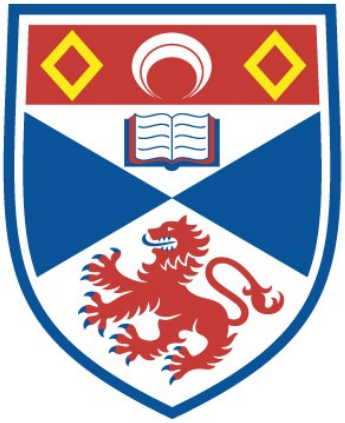

1974

PERTURBATION SPECTROSCOPY OF THE ARGON ION LASER

A thesis presented by

M H Dunn, BA

to the

University of St Andrews

in application for the degree of

Doctor of Philosophy

June 1974

ABSTRACT

The technique of perturbation spectroscopy has been applied to study the argon ion laser discharge. In this technique the laser radiation field present within the active medium is switched on and off, and this modulates the population of the upper laser level. By studying the magnitude of these modulations as discharge conditions within the active medium are changed, the population inversions on the $4p^2D_{5/2} - 4s^2P_{3/2}$ and $4p^4D_{5/2} - 4s^2P_{3/2}$ laser transitions have been explored. By studying, in the presence of an applied magnetic field, the polarization induced in the spontaneous emission sidelight through these modulations, the lifetime of the $4p^2D_{5/2}$ upper laser level has been estimated. By studying the population changes induced on other 4p and 4d levels as a consequence of the population change on the upper laser level, the relative importance of various proposed excitation mechanisms for the 4p upper laser levels have been assessed.

The population inversions ($1 - g_1N_2/g_2N_1$, where N_1 is the population of the upper laser level and N_2 the population of the lower laser level) on the $4p^2D_{5/2} - 4s^2P_{3/2}$ and $4p^4D_{5/2} - 4s^2P_{3/2}$ transitions of Ar II are destroyed by increasing the argon pressure above 0.2 - 0.3 Torr, and for higher pressures the medium exhibits absorption. Both population inversions increase slowly with discharge current. By using a flow graph technique to analyse the population inversions, this latter is shown to imply that the electron temperature in the discharge increases with current.

The polarization experiments have been analysed by both a simple rate equation treatment, and by a more complete approach based on Lamb theory. This latter treatment demonstrates that the dependence of polarization ratio on magnetic field can be used to determine the lifetime of the upper laser level. Polarization

ratios on the $4p^2D_{5/2} - 4s^2P_{3/2}$ and $4p^4D_{5/2} - 4s^2P_{3/2}$ transitions have been measured as a function of discharge parameters and applied axial magnetic field. From the variation of polarization ratio with magnetic field, the lifetime of the $4p^2D_{5/2}$ level of Ar II under discharge conditions has been estimated.

The perturbations in the populations of other 4p and 4d levels of Ar II resulting from the modulation of the upper laser level have been measured as a function of discharge parameters. Their magnitudes and dependence on discharge current provide direct evidence that an important excitation pathway for the 4p upper laser levels of Ar II is step wise excitation through the quartet 4s levels of Ar II.

DECLARATION

I hereby certify that this thesis has been composed by me, and is a record of work done by me, and has not previously been presented for a higher degree.

This research was carried out in the School of Physical Sciences, in the University of St Andrews, under the supervision of Dr A Maitland.

M H Dunn

CERTIFICATE

I certify that M H Dunn BA has spent nine terms at research work in the Physical Science Laboratory of St Salvator's College, in the University of St Andrews, under my direction, that he has fulfilled the condition of Ordinance No 16 (St Andrews) and that he is qualified to submit the following thesis in application for the Degree of Doctor of Philosophy.

A Maitland

Research Supervisor

CAREER

M H Dunn was born in Eston, Yorkshire on 22 October 1942, and educated at Stockton Grammar School, Stockton on Tees and the Royal Grammar School, Newcastle upon Tyne. He was awarded a State Scholarship and Exhibition to Peterhouse, Cambridge in 1962, and was later William, Baron Kelvin Scholar at Peterhouse. He obtained the degree of BA in Natural Sciences in 1965, and commenced postgraduate studies at St Andrews in October 1965. Since October 1968 he has been a lecturer in the Physics Department, University of St Andrews.

ACKNOWLEDGEMENTS

I would like to thank:

Arthur Maitland, my supervisor, for his advice, interest and encouragement throughout this work;

Also the members of the Laser Group, both past and present;

Fritz Akerboom for his glass-blowing skills;

Norma Trisha and Linda for typing the thesis and Tom McQueen for duplicating it.

ABSTRACT

The technique of perturbation spectroscopy has been applied to study the argon ion laser discharge. In this technique the laser radiation field present within the active medium is switched on and off, and this modulates the population of the upper laser level. By studying the magnitude of these modulations as discharge conditions within the active medium are changed, the population inversions on the $4p^2D_{5/2} - 4s^2P_{3/2}$ and $4p^4D_{5/2} - 4s^2P_{3/2}$ laser transitions have been explored. By studying, in the presence of an applied magnetic field, the polarization induced in the spontaneous emission sidelight through these modulations, the lifetime of the $4p^2D_{5/2}$ upper laser level has been estimated. By studying the population changes induced on other 4p and 4d levels as a consequence of the population change on the upper laser level, the relative importance of various proposed excitation mechanisms for the 4p upper laser levels have been assessed.

The population inversions ($1 - g_1N_2/g_2N_1$, where N_1 is the population of the upper laser level and N_2 the population of the lower laser level) on the $4p^2D_{5/2} - 4s^2P_{3/2}$ and $4p^4D_{5/2} - 4s^2P_{3/2}$ transitions of Ar II are destroyed by increasing the argon pressure above 0.2 - 0.3 Torr, and for higher pressures the medium exhibits absorption. Both population inversions increase slowly with discharge current. By using a flow graph technique to analyse the population inversions, this latter is shown to imply that the electron temperature in the discharge increases with current.

The polarization experiments have been analysed by both a simple rate equation treatment, and by a more complete approach based on Lamb theory. This latter treatment demonstrates that the dependence of polarization ratio on magnetic field can be used to determine the lifetime of the upper laser level. Polarization

ratios on the $4p^2D_{5/2} - 4s^2P_{3/2}$ and $4p^4D_{5/2} - 4s^2P_{3/2}$ transitions have been measured as a function of discharge parameters and applied axial magnetic field. From the variation of polarization ratio with magnetic field, the lifetime of the $4p^2D_{5/2}$ level of Ar II under discharge conditions has been estimated.

The perturbations in the populations of other 4p and 4d levels of Ar II resulting from the modulation of the upper laser level have been measured as a function of discharge parameters. Their magnitudes and dependence on discharge current provide direct evidence that an important excitation pathway for the 4p upper laser levels of Ar II is step wise excitation through the quartet 4s levels of Ar II.

TABLE OF CONTENTS

CHAPTER 1

INTRODUCTION AND PRINCIPLES OF EXPERIMENT

1.1 Introduction

When a laser oscillates the emission of coherent radiation constitutes an additional process of energy loss from the active medium. This loss process is extremely selective in that the coherent output power is supplied only by a net increase in the rate at which radiative transitions take place downwards from the upper to the lower laser level; the process of stimulated emission being responsible for this increase. As a consequence laser oscillation depopulates the upper laser level and can populate the lower laser level, but these are the only direct changes produced in the active medium (fig. 1.1)

If changes are observed in the populations of other levels, then these imply the presence, in the active medium, of coupling mechanisms (either radiative or collisional) linking such levels to the laser levels. Thus by the simple procedure of altering the coherent radiation density in the active medium and studying the perturbations so produced in the energy level populations, for example by emission spectroscopy, microscopic processes within the active medium can be investigated.

Further, a detailed study of the direct population change on the upper laser level and its dependence on coherent radiation density can be used to determine population inversions and laser level lifetimes.

In principle the technique is closely related to conventional optical pumping experiments, where spontaneous emission radiation from a pumping lamp is used to selectively perturb the populations of the energy levels under investigation.

This thesis is about the application of the technique, to be called perturbation spectroscopy[1], to a study of the argon ion laser, but the principles involved have a more general application to other laser systems.

In the argon ion laser the active medium is a high current discharge (100 Acm^{-2}) in low pressure argon (100 mTorr), and, in common with gas discharges in general, the detailed microscopic processes occurring are numerous and complicated. However, in investigating the discharge as the active medium of a laser, interest is centered on those processes responsible for the creation of the population inversions between upper and lower laser levels. The application of perturbation spectroscopy in this context is particularly appropriate since it enables processes directly involving the laser levels to be studied.

The coherent radiation that perturbs the active medium can either be self-generated, i.e. the active medium under study is enclosed within the optical cavity and is itself the source of the radiation (fig. 1.2a), or be generated by a separate laser which illuminates an external sample of active medium (fig. 1.2b). It should be realised, of course, that in general the laser used for the illumination must have a similar active medium to that under investigation, since chance coincidences between different optical transitions within sufficiently close limits for an interaction are rare. (The recent advent of tunable lasers has, however, removed this restriction - see, for example, Demtröder (1973)[33]).

Each arrangement has its advantages. Since the coherent power level within the laser cavity exceeds that outside, larger perturbations can be produced under optimum conditions with the former method. However, this method has the disadvantage that the active medium can only be investigated when a population inversion exists, since it is only then that coherent radiation is generated, whereas by using an external laser the active medium can be investigated over an extended range of discharge parameters. Both experimental arrangements have been used in the studies reported here.

Three aspects of the perturbation spectroscopy of the argon ion

laser have been investigated, namely:

(i) The measurement of population inversions by monitoring the perturbations on transitions originating from the upper laser levels. This method enables the change-over in the active medium from optical gain to absorption to be explored.

(ii) Polarization effects in the perturbation spectrum which occur as a consequence of the linear polarization of the laser radiation. Such effects enable level lifetimes to be investigated.

(iii) Perturbations in the populations of the 4p and 4d levels of ArII due to oscillation on a single 4p - 4s laser transition. Excitation and coupling mechanisms in the discharge are studied by this method.

1.2 Format

Before considering in detail the work on the argon ion laser, the influence of laser oscillation on the spontaneous emission spectrum of a simple three level system is discussed in the next section (ch1.,§3). The aim is to introduce the rate equation approach used in the analysis of perturbation spectra, and to demonstrate more precisely the power of the technique in studying population inversions and coupling mechanisms. This section is then followed by a historical review of perturbation spectroscopy; the purpose being to consider applications to other laser systems and to place the present work on the argon ion laser in context.

A description of the experimental apparatus and a discussion of the design and construction of quartz argon ion lasers are the subjects of ch.2. Detailed considerations of the population inversion, polarization and coupling mechanism studies are then given in chs.3, 4 and 5 respectively. Conclusions regarding these studies are summarized in the appropriate chapter.

A review of experimental and theoretical investigations on the argon ion laser is presented in Appendix A. This provides the necessary

background for the interpretational work included in chs.3, 4, and 5.

For convenience a flow chart is included which summarizes the format of the thesis (fig. 1.3).

1.3 Perturbation spectroscopy of a three level system

The simplified situation to be considered is illustrated in fig. 1.4, in which three energy levels are considered explicitly. Level 1 is the upper laser level (population N_1 vol^{-1}), level 2 is the lower laser level (population N_2 vol^{-1}) and level m is a general level (population N_m vol^{-1}) which is assumed to be coupled to the upper laser level by either radiative or collisional processes.

Two aspects are to be considered:

(i) the influence of laser oscillation on the population of the general level m, and

(ii) the influence of laser oscillation on the population of the upper laser level itself.

The lifetime of the upper laser level to all radiative and collisional decay processes, except stimulated emission and coupling to level m, is τ_1. The upper laser level is assumed to be pumping level m at a rate R_{1m} (vol^{-1}) and to be pumped by that level at a rate R_{m1} (vol^{-1}) where

$$R_{1m} = \rho_{1m} N_1$$
$$R_{m1} = \rho_{m1} N_m \,, \qquad (1.1)$$

and the coefficients ρ_{1m} and ρ_{m1} depend on the details of the coupling processes. The net rate of excitation of the upper laser level by all remaining processes is described by the rate coefficient R_1 (vol^{-1}).

The lower laser level has a corresponding lifetime τ_2 and is not coupled to the level m. It is, however, pumped by spontaneous radiative decay of the upper laser level at a rate $A_{12}N_1$ where A_{12} is the associated transition probability (Einstein A-coefficient). It is

particularly important, as will be seen shortly, that this process is considered explicitly. All other excitation processes for the lower laser level are described by the rate coefficient $R_2(\text{vol}^{-1})$.

The lifetime and rate of excitation of the general level are τ_m and R_m respectively. Both these quantities do not take into account coupling to the upper laser level, this being described separately by equations (1.1) above.

In the absence of laser oscillation the equations describing the steady state populations of the three energy levels are

$$\begin{aligned} R_1 + (R_{m1} - R_{1m}) &= N_1\tau_1^{-1} \\ A_{12}N_1 + R_2 &= N_2\tau_2^{-1} \\ R_m + (R_{1m} - R_{m1}) &= N_m\tau_m^{-1} \ . \end{aligned} \tag{1.2}$$

If the system is now operated as a laser, the net increase in the number of downward transitions from the upper laser level to the lower laser level when coherent power P per unit volume is extracted is

$$L = P(h\nu_{12})^{-1} \ . \tag{1.3}$$

As a consequence of this additional loss process the level populations are perturbed by amounts δN and the modified equations describing the steady state populations in these circumstances become

$$\begin{aligned} R_1 + \rho_{m1}(N_m + \delta N_m) - \rho_{1m}(N_1 + \delta N_1) - L &= (N_1 + \delta N_1)\tau_1^{-1} \\ A_{12}(N_1 + \delta N_1) + R_2 + L &= (N_2 + \delta N_2)\tau_2^{-1} \\ R_m + \rho_{1m}(N_1 + \delta N_1) - \rho_{m1}(N_m + \delta N_m) &= (N_m + \delta N_m)\tau_m^{-1} \ . \end{aligned} \tag{1.4}$$

If the coupling between the upper laser level and the general level is assumed to be weak (i.e. $\rho_{1m} << \tau_1^{-1}$, etc), then the perturbations in the level populations can be obtained by elimination between (1.4) and (1.2) as

$$\begin{aligned} \delta N_1 &= -L\tau_1 \\ \delta N_2 &= +L\tau_2(1 - A_{12}\tau_1) \\ \delta N_m &= \tau_m\rho_{1m}\delta N_1 \ . \end{aligned} \tag{1.5}$$

The perturbations in level populations produce changes in the spontaneous emission sidelight associated with the levels, the relation being

$$\delta I_{pq} = G\, h\nu_{pq}\, A_{pq}\, \delta N_p \quad , \tag{1.6}$$

where A_{pq} is the Einstein A-coefficient for the transition p to q and G is a factor describing the geometry of the light collection system. From (1.2), (1.5) and (1.6) the following may be deduced

$$\sigma = (\delta I_m/I_m)/(\delta I_1/I_1) = R_{1m}\, R_m^{-1} \quad . \tag{1.7}$$

The left hand side is just the ratio of the fractional change in the intensity of the spontaneous emission from the general level m to the fractional change in the intensity of the spontaneous emission from the upper laser level. The right hand side is the fractional pumping of the general level m due to its coupling with the upper laser level.

The left hand side of (1.7) is measured experimentally. Since it involves only ratios of intensities measured at the same wavelength, calibration of the geometry or the spectral response of the apparatus is not necessary. The coupling mechanism between the levels can therefore be readily studied in detail by investigating how the ratio in (1.7) alters as discharge conditions are altered.

It is of course also possible to analyse measurements using (1.5) but in this case the spectral response of the detection apparatus must be known. The approach adopted depends very much on the energy levels under investigation and the information required.

The assumption of weak coupling made in deriving (1.5) and (1.7) is equivalent to the condition $\delta N_m << \delta N_1$, and is a valid approximation for all the measurements made on the argon ion laser reported here.

The type of information about the discharge that can be obtained from perturbation spectroscopy depends very much on the energy level structure of the particular active medium under investigation. It will be demonstrated in ch. 5 that in the case of the argon laser the coupled

energy levels are such that information about excitation pathways for the population inversions may be obtained.

Expression (1.5) shows that when the lifetime of the upper laser level is determined solely by its radiative decay to the lower laser level (i.e. $A_{12}\tau_1 = 1$), there is no change, to first-order, in the population of the lower laser level through the onset of laser oscillation. While not of interest to the present studies on the argon ion laser, since transitions from the lower laser levels were not monitored being in the far UV (200Å), it does indicate that the technique could be used as a particularly sensitive method for detecting the influence of environmental effects (e.g. collisions) on upper laser level lifetimes.

Solution of the rate equations (1.2) and (1.4) can be facilitated by use of a flow graph technique proposed by Maitland and Dunn[2] (Appendix B). The solution for the case of the general level population using this technique is given in fig. 1.5.

Finally in this section the relation between the perturbation of the upper laser level population (N_1) and the population inversion is discussed, i.e. the parameter L in equation (1.3) is determined.

Consider the experimental arrangement shown in fig. 1.2(b) where the active medium under investigation is illuminated by a separate radiation source, and let the intensity of the coherent radiation in the active medium be I. Then the additional process of stimulated emission increases the depopulation rate (vol^{-1}) of the upper laser level by

$$KIN_1/g_1 \quad , \qquad (1.8)$$

where K is a constant depending on the linewidth of the laser radiation, the linewidth of the transition, the Einstein B coefficient, etc. (ch3,§2). and g_1 is the statistical weight of the upper laser level. At the same time there is also absorption occurring which depends on the population of the lower laser level and leads to a pumping rate for the upper level

of

$$KIN_2/g_2 \ . \qquad (1.9)$$

The net rate of depopulation of the upper laser level is therefore

$$KI(N_1/g_1 - N_2/g_2) \ , \qquad (1.10)$$

so that the upper laser level population in the presence of laser radiation is described by the rate equation

$$R_1 = N_1\tau_1^{-1} + KI(N_1/g_1)(1 - g_1N_2/g_2N_1) \ . \qquad (1.11)$$

From this it may be seen that the fractional population change due to illumination of the active medium is

$$(\delta N_1/N_1) \propto - (1 - g_1N_2/g_2N_1) \ . \qquad (1.12)$$

Thus if the population of the upper level decreases when the active medium is illuminated, this implies the existence of a population inversion ($g_2N_1 > g_1N_2$), whereas if the population increases on illumination this implies a condition of absorption ($g_2N_1 < g_1N_2$). By evaluating the constant in (1.10) (see ch3, §2) the magnitude of the population inversion can be calculated. The population change on the upper laser level is most conveniently monitored by observing the spontaneous emission sidelight due to transitions originating from the level.

As a consequence of the linear polarization of the laser radiation, the change in intensity of the spontaneous emission radiation due to the perturbation of the upper laser level population also exhibits polarization; i.e. the populations of the different magnetic sublevels of the upper laser level are influenced to different extents by the polarized laser radiation. This aspect is treated in detail in ch.4.

1.4 Historical review of perturbation spectroscopy

The first report of the influence of laser oscillation on the spontaneous emission from a laser discharge is that of White and Rigden (1963)[3] who investigated effects in the He-Ne laser. Their work was concerned with the influence of laser oscillation at 3.39μ ($3s_2$-$3p_4$ neon)

and 6328Å ($3s_2$-$2p_4$ neon) on the spontaneous emission sidelight from transitions originating on the $3p_4$ neon level. The technique was not at this stage used for any specific diagnostic purpose. Freiberg et al (1965)[4] proposed that the effect might be used as a covenient means of monitoring changes in infra-red power outputs with the use of only visible radiation detection apparatus, since some of the accompanying changes in the spontaneous emission spectrum occur at optical wavelengths.

Parks and Javan (1964,1965)[5,6] were the first to apply perturbation spectroscopy to a serious study of collision processes in the He-Ne laser. They determined the atomic collision cross section for excitation transfer between the closely spaced $2s_2$ and $2s_3$ levels of neon using a laser oscillating at 1.15μ ($2s_2$-$2p_4$).

Waksberg and Carswell (1965)[7] reported intensity changes on a large number of neon transitions due to laser oscillation at 6328Å in the He-Ne laser, and this work was extended by Weaver and Frieberg (1966)[8] to a more detailed study of radiative and collisional processes. Changes in intensity of some eighteen transitions originating on the $3s_2$-$3s_5$, $3p_1$-$3p_{10}$, $2s_2$-$2s_5$ and $2p_1$-$2p_{10}$ levels of neon were studied in the He-Ne discharge oscillating at either 3.39μ, 1.15μ or 6328Å. The observed population changes were compared with those calculated on the basis of radiative cascade coupling between the neon levels, using transition probabilities due to Faust and McFarlane. Deviations between observed and calculated perturbations were assigned to collisional couplings between the levels. On this basis there was evidence of significant collisional mixing between levels within the $3s_2$-$3s_5$, $3p_1$-$3p_{10}$ and $2p_1$-$2p_{10}$ groups. The observation of perturbations on higher energy levels than the laser levels indicated that electron impact excitation from the $3s_2$ level was also taking place. Despite the quantitative nature of the results no attempt was made to estimate collision cross

sections for the proposed processes.

A point of concern regarding the results of Weaver and Frieberg, which is not considered in their paper, is that in certain cases transitions originating on a common upper level indicate different population changes for that level. Whether these inconsistencies are due to an inadequate knowledge of the transition probabilities, to the detection apparatus, or to line absorption effects in the discharge is not made clear.

Garscadden and Adams (1966)[9] by monitoring changes in the discharge current due to lasing have demonstrated that electron impact ionization from the $3s_2$ neon level is also occurring under the discharge conditions in the He-Ne laser.

Khaikin (1967)[10] as well as investigating collisional mixing between the $3s_2$-$3s_5$ neon levels, studied electron impact excitation from the $3s_2$ level to higher neon levels in more detail. The principal levels pumped by this process were found to be the $4s_1'$ - $4s_1'''$ and $5s_1'''$ - $5s_1''''$ levels and excitation rates were calculated for both sets of levels. Khaikin also obtained evidence that electron impact de-excitation is comparable to radiative de-excitation not only for these higher neon levels but also for the $3s_2$ level itself.

The helium-neon system has also been investigated by Hänsch and Töschek (1966)[29] and Csillag et al (1968)[30]. Both groups examined the saturation of the perturbation spectrum with increasing coherent radiation density in the active medium in order to determine relative lifetimes, transition probabilities and pumping rates for the neon laser levels ($2p_4$-$3s_2$, 6328Å) (ch1,§3).

In summary, therefore, radiative and collisional coupling mechanisms and the relative lifetimes and pumping rates of the laser levels have been extensively studied in the He-Ne laser using perturbation spectroscopy.

Abrams and Wolga (1967)[11] have carried out a very elegant perturbation spectroscopy experiment on a helium laser to demonstrate

directly the validity of the Wigner spin rule in helium-helium collisions. They used a helium laser which oscillated continuously on two transitions $4^3P - 3^3D$ (1.95μ) and $4^3F - 3^3D$ (1.86μ), to perturb a separate helium discharge. In particular they were able to selectively perturb either the 4^3P or 4^3F helium populations depending on the laser transition used. The Wigner spin rule states that in the case of interacting atoms or molecules for which Russell-Saunders coupling is valid, total spin is conserved in atom-atom collisions. For conditions in the discharge cell, the predominant species in atom-atom collisions with either the 4^3P or 4^3F state is the ground state (1^1S) helium atom. If the Wigner spin rule is obeyed, therefore, the initial triplet states should be converted only to other triplet (and not singlet) helium states by such atom-atom collisions. Associated perturbations are therefore expected only on transitions originating on triplet states when either the 4^3P or 4^3F populations are perturbed directly by the laser radiation. For the 4^3P state the associated changes in the populations of the 4^3S and 4^3D states implied atom-atom collision cross sections comparable to the gas kinetic, while changes in the populations of the 4^1S, 4^1P and 4^1D levels implied cross-sections two orders of magnitude smaller. The findings are therefore in accord with the Wigner spin rule. In the case of the 4^3F state the Wigner spin rule was found to be violated as previously suggested by Lin and Fowler, who showed that spin-orbit coupling, and hence the spin rule, breaks down for the nF states of helium.

Freiberg and Weaver (1967)[12] have carried out a comprehensive investigation on the dc xenon laser discharge oscillating at 3.51μ ($5d_{33} - 6p_{22}$). They monitored not only the perturbations in level populations but also perturbations in electron density, using a microwave cavity method, and in the discharge current. In the xenon discharge radiative coupling between levels was found to be still important, but electron excitation was found to be more significant as a collisional

coupling process than atom-atom collisions which dominate the situation in He-Ne and He lasers. A significant finding from this investigation is that in the dc xenon laser, electron excitation processes are occurring from the 6s metastable states to the lower laser level ($6p_{22}$), thereby decreasing the population inversion and so degrading the laser power output at 3.51μ.

Perturbation spectroscopy has been applied to the CO_2-N_2-He laser mainly by Crane and Waksberg (1967)[13], but also by Rigden and Moeller (1966)[14] Transitions in the first ($B^3\Pi$ - $A^3\Sigma$) and second ($C^3\Pi$ - $B^3\Pi$) positive systems of the nitrogen molecule and in the Angstrom band ($B^1\Sigma$ - $A^1\Pi$) of the carbon monoxide molecule were monitored as the 10.6μ laser radiation, corresponding to transitions between vibrational-rotational levels of the CO_2 electronic ground state {$(00^0 1)$ - $(10^0 0)$}, was switched on and off. Although the majority of transitions showed decreases in intensity due to laser oscillation, certain were found to increase in intensity. This indicates that the effect is not totally due to the decrease in the effective temperature of the discharge that accompanies the extraction of coherent power. No attempt was made to use the reported perturbations to analyse collisional and radiative processes occurring in the laser. A drawback of the technique when applied to the CO_2-N_2-He laser is that it is not possible to monitor by emission spectroscopy the populations of the N_2 vibrational and rotational states thought to be responsible for pumping the CO_2 molecules, since these are in the N_2 electronic ground state, and do not decay radiatively.

Weaver et al (1967)[15] have investigated changes in the sidelight flourescence from the solid state Nd:Cr:YAG laser due to oscillation at 1.06μ, but not in sufficient detail to provide information on the radiative decay patterns and relaxation processes.

Mention should also be made of an experiment carried out by Beterov

and Chebotaev (1966)[16] on the He-Ne laser where spontaneous emission radiation was used to perturb the discharge as opposed to stimulated emission. A helium discharge pumping lamp was placed in close proximity to the He-Ne laser discharge tube, and radiation from transitions terminating on helium 2^1S and 2^3S metastable states was used to selectively depopulate the same states in the helium-neon laser discharge through optical pumping. The resulting changes in the populations of the excited neon levels enabled the cross sections for the excitation of the neon levels by collisions with helium metastables to be determined. These are, of course, the processes that lead to the establishment of population inversions in neon.

This last experiment demonstrates the close relation between conventional optical pumping experiments, involving spontaneous emission radiation, and perturbation spectroscopy which involves stimulated emission radiation.

In order to complete this section the papers more directly relevant to the present work will be reviewed but detailed discussion will be left to the appropriate later chapters.

The first paper to appear relating to the argon ion laser in this context was that of Rosenberger (1966)[17] who investigated the interaction between two simultaneously oscillating laser transitions. This work was later extended by Merkelo et al (1968)[18]. Both these papers examine the changes in coherent power from one laser transition due to the simultaneous oscillation of another transition. A decrease in coherent power from the former transition was expected, due either to a depletion of the population of its upper level or to an increase in the population of its lower level when the second transition oscillated, but in certain cases the power output was observed to increase (anomalous competition). Ferrario et al (1969)[19] were the first to propose a feasible mechanism to explain this behaviour (ch. 5).

The present work relating to the perturbations in the spontaneous emission from transitions originating on 4p and 4d levels of ArII (ch. 5) was first reported in 1968[20]. Also in 1968, Merkelo et al[21] reported on perturbations in the spontaneous emission from the transitions originating from the 4s levels of ArII. Vacuum UV instrumentation was required since these transitions terminate on the ion ground state and so have wavelengths around 700 Å.

More recently Karatsu and Ogura (1972)[22] have investigated similar effects in the krypton ion laser, but no interpretational work accompanies their results.

Several experiments have been performed investigating the strong interactions that occur between oscillating modes at 5145Å and 4880Å as a consequence of the competition effects discussed above (Forsyth (1967)[23], Statz et al (1969)[24], Grimblatov et al (1972)[25]). The relevance to mode effects of the present measurements of perturbations in the 4p populations is discussed further in ch. 5.

Polarization effects in the perturbation spectrum of the He-Ne laser have been investigated by Krupenikova and Chaika (1966)[26], Kallas and Chaika (1967)[27] and Hänsch and Toschek (1966)[28]. By applying an axial magnetic field to the laser discharge and studying its influence on the polarization of the perturbation spectrum, the lifetime of the $2p_4$ level in neon (lower laser level of 6328Å and 1.15μ laser transitions) was determined, while measurements made under zero field conditions enabled the influence of depolarizing collisions to be assessed. Hänsch and Toschek used a separate discharge cell and were hence able to study depolarizing collisions over a wider range of discharge conditions (including the situation in pure Ne). The independent estimates of the radiative lifetime of the $2p_4$ level agreed only to an order of magnitude (6nS, 14nS) and this applied also to the estimates of depolarization cross-section (10^{-15} - 10^{-14} cm^2). The former

discrepancy may have been due to stray magnetic fields, for example from the discharge current, since precautions were not taken to allow for such effects in the experiments.

The present work on polarization effects in the perturbation spectrum of the argon ion laser was published in 1967[1].

The application of perturbation spectroscopy to the determination of population inversions was first proposed by Johnston (1970)[31] who studied the argon ion laser. In Johnston's method the fractional change in the population of the upper laser level ($4p^2D_{5/2}$- $4s^4P_{3/2}$, 4880Å) is measured as a function of coherent radiation density in the cavity, and the limiting value, corresponding to an infinite radiation density, is estimated by extrapolation. This limiting value can then be related to the initial population inversion (ie before saturation) if certain assumptions are made about the saturation of the population inversion with coherent power. The dependence of the population inversion at 4880Å on discharge current and magnetic field was studied by this technique (ch. 3).

In Johnston's method a high coherent radiation density is required in order to saturate the fractional population change on the upper laser level, and so the method can only be used when the active medium understudy is within the laser cavity. The results reported by Johnston refer to conditions of high population inversion and no attempt was made to investigate the change-over from gain to absorption in the active medium. The present studies on population inversions in the argon ion laser[32], where an external cell was used, both avoid assumptions regarding saturation in the laser and enable the transition region from gain to absorption to be investigated.

Vladimirova et al[34] have determined pumping rates and lifetimes of upper laser levels in the argon ion laser by measuring the fractional intensity changes in the spontaneous emission from the laser transitions

themselves. If the total cavity loss and the coherent power extracted per unit volume of active medium are known, pumping rates and lifetimes can be calculated (see ch.3).

A summary of investigations using perturbation spectroscopy is given in table 1.1. For a brief review of perturbation spectroscopy in relation to other classes of laser based spectroscopy see Demtröder (1973)[33].

Laser	Aspect	Investigator
He-Ne	Radiative/Collisional coupling	Parks and Javan (1964,1965)[5,6]
		Waksberg and Carswell (1965)[7]
		Weaver and Freiberg (1966)[8]
		Garscadden and Adams (1966)[9]
		Khaikin (1967)[10]
	Lifetimes, pumping rates	Hänsch and Toschek (1966)[29]
		Csillag et al (1968)[30]
	Polarization effects	Krupenikova and Chaika (1966)[26]
		Kallas and Chaika (1967)[27]
		Hänsch and Toschek (1966)[28]
	Pumping Mechanism	Beterov and Chebotaev (1966)[16]
He	Wigner spin rule	Abrams and Wolga (1967)[11]
Xenon	Radiative/Collisional coupling	Freiberg and Weaver (1967)[12]
Krypton	Radiative/Collisional coupling	Karatsu and Ogura (1972)[22]
Argon	Mode and Competition effects	Rosenberger (1966)[17]
		Merkelo et al (1968)[18]
		Ferrario et al (1969)[19]
	Collisional/Radiative coupling	Dunn (1968)[20]
		Merkelo et al (1968)[21]
	Polarization	Dunn and Maitland (1967)[1]
	Population inversion	Johnston (1970)[31]
		Dunn and Ross (1973)[32]
Co_2-N_2-He	Radiative/Collisional coupling	Crane and Waksberg (1967)[13]
		Rigden and Moeller (1966)[14]
Nd:Cr:YAG	Radiative/Collisional coupling	Weaver et al (1967)[15]

References (Ch. 1)

1 Dunn M H and A Maitland 1967 Proc Phys Soc 92 1106-14

2 Maitland A and M H Dunn 1973 J Phys D 6 1266

3 White A D and J D Rigden 1963 Appl Phys Lett 2 211-2

4 Freiberg R J, L A Weaver and J T Verdeyen 1965 J Appl Phys 36 3352

5 Parks J H and A Javan 1965 Phys Rev 139 A1351-8

6 Parks J H, A Szöke and A Javan 1964 Bull Am Phys Soc 9 490

7 Waksberg A L and A I Carswell 1965 Appl Phys Lett 6 137-8

8 Weaver L A and R J Freiberg 1966 J Appl Phys 37 1528-35

9 Garscadden A and S L Adams 1966 Proc IEEE 54 427-8

10 Khaikin A S 1967 Sov Phys JETP 24 25-32

11 Abrams R L and G J Wolga 1967 Phys Rev Lett 19 1411-14

12 Freiberg R J and L A Weaver 1967 J Appl Phys 38 250-62

13 Crane R A and A L Waksberg 1967 Appl Phys Lett 10 237-9
(See also RCA Victor Research Report No 3.900.4 Jan 1967)

14 Rigden J D and G Moeller 1966 IEEE J Quant Elec QE-2 365-8

15 Weaver L A, I Liberman and C H Church 1967 J Appl Phys 38 5405-6

16 Beterov I M and V P Chebotaev 1966 Opt and Spectroscopy 20 597-8

17 Rosenberger D 1966 Phys Lett 22 54

18 Merkelo H, R H Wright, E.P. Bialecke and J P Kaplafka 1968 Appl Phys Lett 12 337

19 Ferrario A, A Sironi and A Sona 1969 Appl Phys Lett 14 174

20 Dunn M H 1968 IEEE J Quant Elec QE-4 43

21 Merkelo H, R H Wright, J P Kaplafka and E P Bialecke 1968 Appl Phys Lett 13 401

22 Karatsu O and I Ogura 1972 Japanese J Appl Phys 11 1165

23 Forsyth J M 1967 Appl Phys Lett 11 391

24 Statz H, G A de Mars and C L Tang 1969 Appl Phys Lett 14 125

25 Grimblatov V M, E P Ostapchenko and V V Teselkin 1972 Sov J of Quant Elec 1 378

26 Krupenikova T and M Chaika 1966 Optics and Spectroscopy 20 605

27 Kallas Kh and M Chaika 1967 Optics and Spectroscopy 22 283

28 Hänsch Th and P Toschek 1966 Phys Lett 22 150

29 Hänsch Th and P Toschek 1966 Phys Lett 20 273

30 Csillag L, M Janossy and T Salamon 1968 Phys Lett 26A 436

31 Johnston Jr T F 1970 Appl Phys Lett 17 161

32 Dunn M H and J N Ross 1973 Phys Lett 44A 247

33 Demtröder W 1973 Phys Lett 7c 223

34 Vladimirova N M, I D Konkov, R E Rovinskii and N V Cheburkin, 1970, Sov Phys JETP 30 813

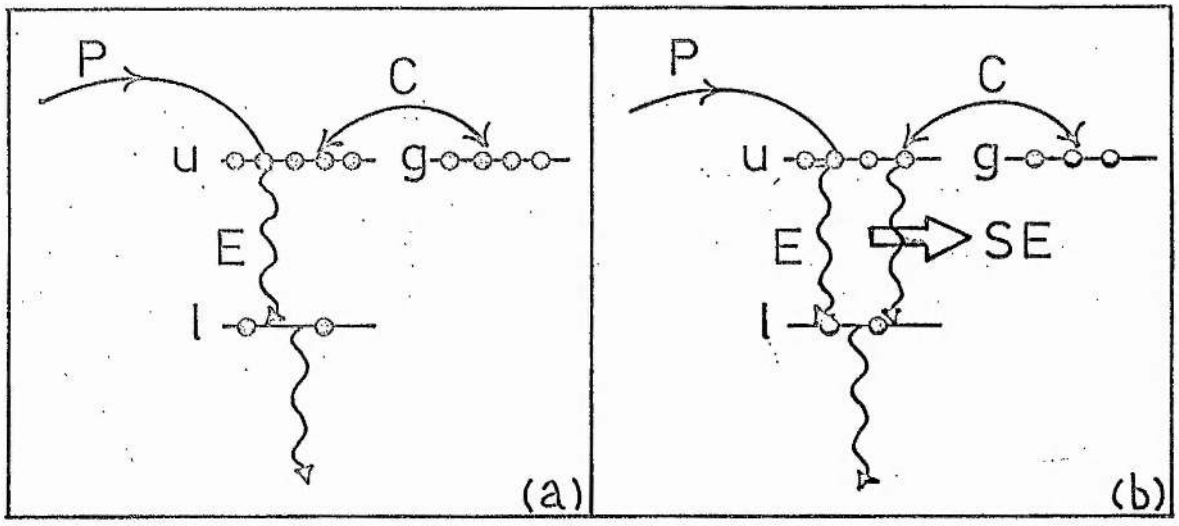

Figure 1.1 The principle of perturbation spectroscopy is illustrated in this diagram. In (a) the situation in the active medium in the absence of laser radiation is shown. The population of the upper laser level (u), represented by the black dots, is determined by a balance between pumping processes (P) and decay by spontaneous emission (E). The population of a general level (g) may depend on the population of the upper laser level through either radiative or collisional coupling processes (C) in the active medium. In (b) coherent radiation is extracted from the active medium, so introducing an additional loss process, that of stimulated emission (SE), which reduces the population of the upper laser level. By monitoring the consequent population change for the level g, the coupling processes C may be studied.

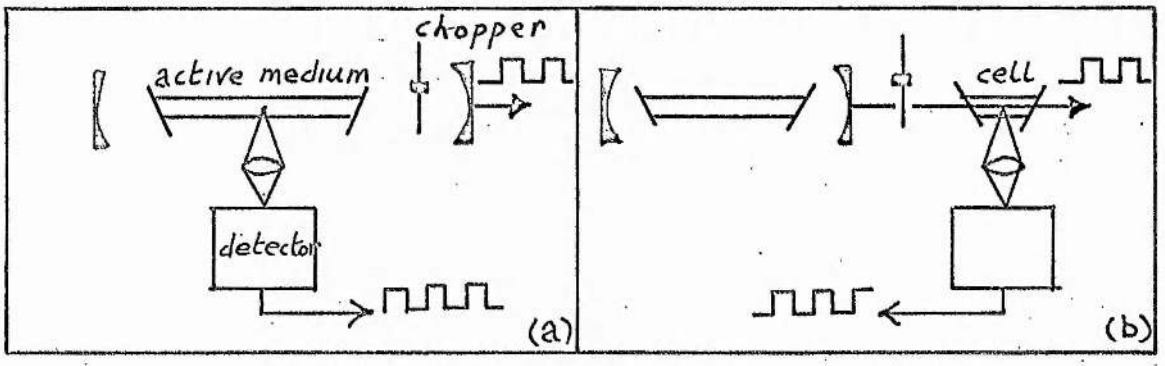

Figure 1.2 Experimental arrangements for perturbation spectroscopy: (a) self-generated radiation, (b) external cell.

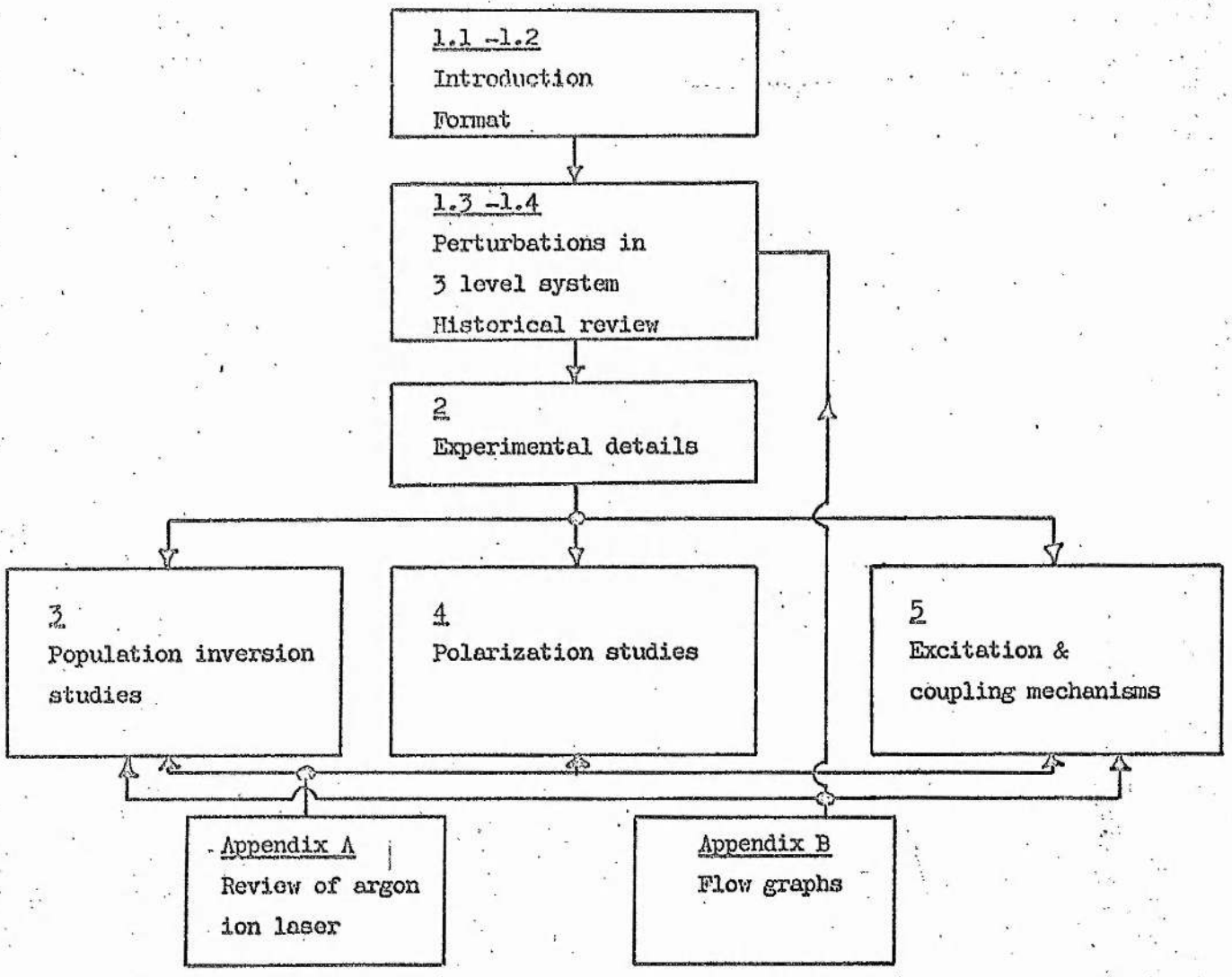

Figure 1.3 Format of thesis.

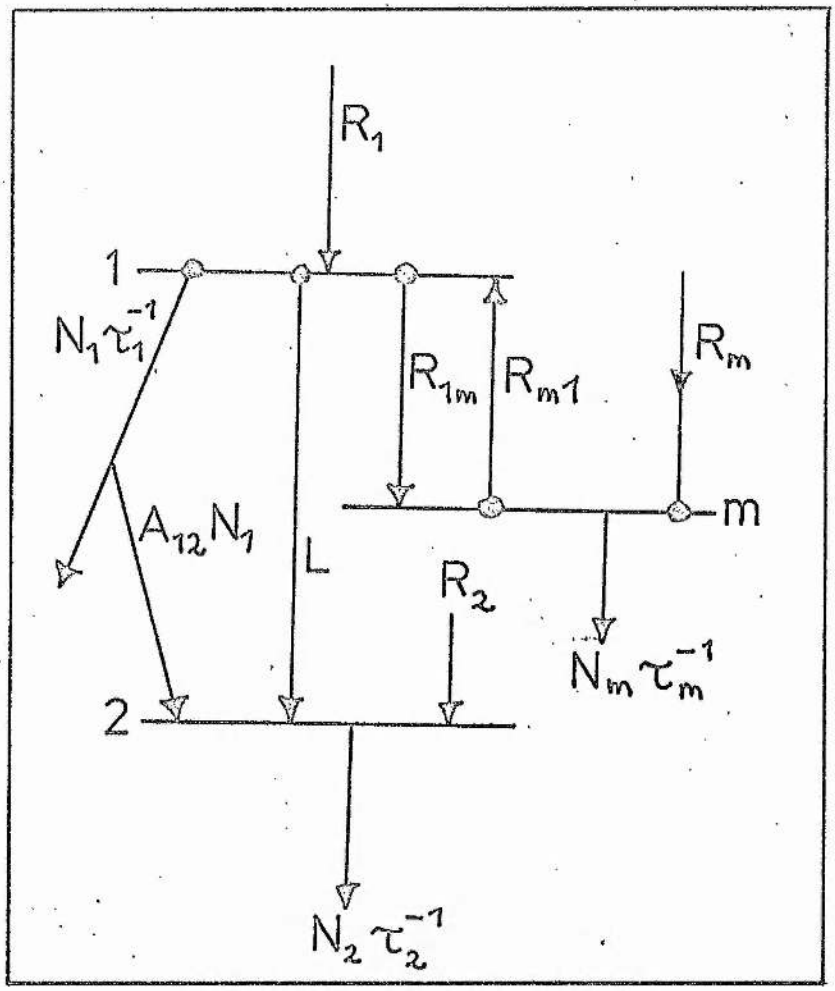

Figure 1.4 Coupling mechanisms for a three level system with laser oscillation.

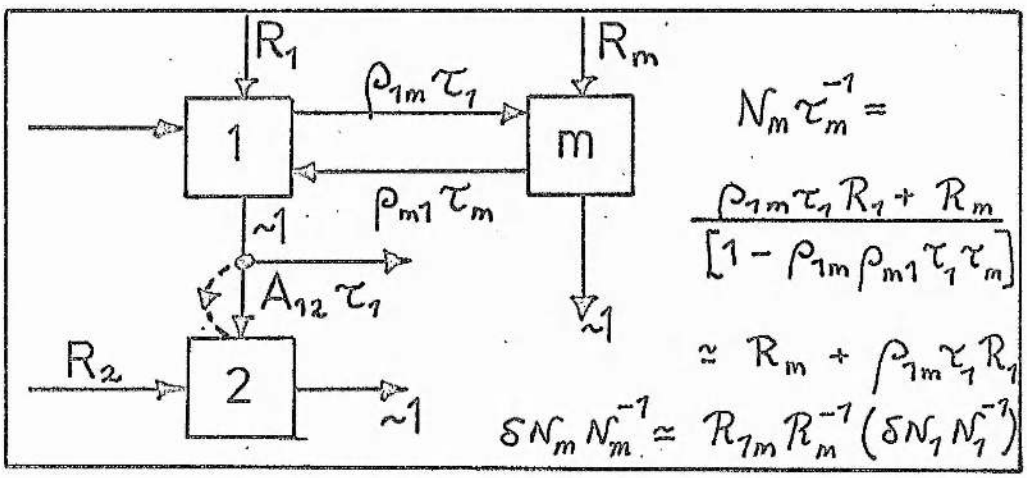

Figure 1.5 Flow graph analysis of fractional perturbation on general level (m). The influence of laser oscillation is shown by the dotted line. See Appendix B.

CHAPTER 2

EXPERIMENTAL DETAILS

We summarize in this chapter the experimental details relevant to the next three chapters. Additional details appropriate only to particular chapters are given in context. The first section of Appendix A provides a general introduction to argon laser design.

2.1 Argon ion laser

A variety of quartz tube argon lasers have been used, but the two basic designs are shown in fig. 2.1. The active medium is contained by a quartz tube (Thermal Syndicate 'Vitreosil') of about 1 mm wall thickness, 2-4 mm bore and 20 - 50 cm long. The capillary is surrounded by a water cooling jacket about 1 cm in diameter and also fabricated in quartz. The water inlet to the jacket is angled so that the cooling water is directed onto the capillary where it opens out towards the cathode end, if this precaution is not taken a dead space, leading to local boiling, occurs in the cooling water. At each end of the capillary the quartz tubing opens out to $\frac{1}{4}$" - $\frac{1}{2}$". On the design where the anode and cathode are in sidearms (fig. 2.1a) the T-pieces and Brewster angle window assemblies are also of quartz; quartz-pyrex graded seals being introduced in the sidearms before the cathode and anode pyrex envelopes. In the co-axial arrangement (fig. 2.1b) the quartz-pyrex graded seals come immediately after the capillary and are protected by internal quartz sleeves to keep the discharge away from the seals.

The cathode is of the hot, oxide coated type (Mullard thyratron cathode type XR1/12A). Before use the cathode is processed while the tube is being pumped, after which it cannot be exposed to the air without serious deterioration of the emitting surface. The manufacturer's processing schedule was found to be satisfactory for the present usage, and processed cathodes were operated without sputtering at dc currents up to 20 A. This particular cathode, where the emitting surface

is on the inside of a cylinder about $1\frac{1}{2}$" in diameter, is well suited to the co-axial arrangement shown in fig. 2.1b; the only modification required being to drill a $\frac{1}{2}$" diameter hole in the end cap of the heat shield. The most successful arrangement for the anode is a length of water cooled copper tubing of about $\frac{1}{4}$" OD turned into a spiral and contained in a pyrex envelope which it enters through glass to metal seals.

Brewster windows are quartz flats ('Spectrosil A', flat to $\lambda/4$, parallel to 1') fixed with adhesive ('Araldite', 'Torr-seal') onto tube ends cut at the Brewster angle. Reflection losses increase by about 1.5% deg^{-1} for angles greater than the Brewster angle (angle of incidence 56^{o}), but only by about 0.2% deg^{-1} for smaller angles - so provided it is towards the latter angular errors of about 5^{o} can be tolerated, and only a simple jig arrangement is required for cutting the tube ends.

A gas return line to equalize pressure gradients caused by gas pumping connects anode and cathode envelopes. Pyrex tubing of $\frac{1}{4}$" OD and 2-3 times the capillary length is satisfactory - the increase in length and bore over that of the capillary results in this pathway having a higher breakdown voltage so there is no tendency for the discharge to go down the gas return path. The laser tube is first evacuated with an oil diffusion pump fitted with a nitrogen cold tap, and then 3N spectroscopically pure argon is introduced. The pressure is monitored by a Pirani gauge calibrated in situ against a McLeod gauge.

Both single phase and three phase power supplies have been used to operate the different tubes, and a typical single phase design is shown in fig. 2.2.[3] The requirement is for a smoothed dc supply delivering up to 20 A at 500 V. Since the voltage across the laser

tube (200 V for a 25 cm capillary) is approximately independent of discharge current, a ballast resistor (20 Ω) is placed in series with the tube to lead to an overall positive voltage-current characteristic. The resistor is most conveniently made from 1 kW electric fire elements. The L-C smoothing circuit incorporated in the full wave bridge rectifier is designed to reduce voltage ripple on the tube to less than 4% at 100 Hz. For trouble free operation with a gas discharge load, varistors, to prevent voltage spikes developing across the silicon diodes in the bridge, and leakage resistors, to equalize voltage across the capacitors, are essential.

Typically, the quartz tubes described above can be operated at currents up to about 15 amps continuously and up to about 20 amps for short periods, with cooling water from the domestic supply. At higher currents localized boiling takes place within the cooling jacket. At 15 amps the typical multiline multimode power output from a 50 cm length of active medium and through a 95% reflectivity mirror is 150 mW.

Single frequency operation is obtained by a 68° quartz prism in the cavity ('Spectrosil B', optical faces flat to $\lambda/8$). The prism angle is chosen to ensure Brewster angle incidence at minimum deviation. For most of the experiments the cavity length is about 1m and multilayer dielectric mirrors of greater than 99% reflectivity are used to maximize coherent power density within the cavity.

In the studies of gain and absorption in the active medium discussed in ch. 3, an argon discharge cell of similar design to the laser discharge tube was optically pumped by a separate laser. In order to obtain sufficiently high radiation field densities in the discharge cell, which was outside the laser cavity, a metal clad argon laser with plasma jet cathode was used as the light source. Details

of this laser have been given in the literature.[1]

2.2 Detection system

The coherent radiation field inside the laser cavity is switched on and off mechanically at a frequency of about 1 kHz by an electrically driven toothed wheel. This switching period is at least three orders of magnitude greater than characteristic times associated with processes in the discharge - radiative or collisional lifetimes of the relevant energy levels being less than 1 μs (see tables A.2 - A.4). Hence the discharge reaches a steady state between switchings and transients may be neglected in the analysis.

The spontaneous emission sidelight from the discharge is sampled through the water jacket either by imaging the discharge onto the inlet slit of the monochromator or by using a fibre optic light guide. The Carl Zeiss SPM2 grating monochromator has a linear dispersion of 40 Å mm^{-1}, and slit widths of the order of 0.02 mm gave sufficient resolution (1Å) to isolate most of the 4p and 4d transitions studied here. The output from the monochromator is collected by a photomultiplier tube (EMI 9558B). In all cases where an imaging lens was used, the axis of the laser tube was at right angles to the slit axis, so that the slit effectively averaged across the tube bore. With this arrangement the exact orientation of slit and tube is not critical, and the averaging is not sensitive to changes of slit width, defocussing, etc. If the slit is arranged parallel to the axis of the discharge tube, then since the laser radiation is not uniform within the active medium, the exact relative location of slit and the image of the discharge tube is important. In those cases where it was important to make the detection apparatus insensitive to the polarization state of the radiation, a fibre optic light guide was used since this depolarizes the radiation passing through it. Since its dimensions are large

compared to the slit width it also is insensitive to exact relative location.

The maximum intensity change in the spontaneous sidelight produced by the laser radiation is on the laser transition itself and is about 7% of the total spontaneous emission intensity from this transition. Intensity changes on other 4p and 4d transitions are down to 2% of this value, thus changes of the order of 0.1% are to be detected. This is done with a lock-in amplifier (Princeton JB4),the output signal from the photomultiplier first passing through a 100 Hz blocking filter and a pre-amplifier (Princeton CR4). The 100 Hz filter is required since the lock-in amplifier is unable to cope with the signal present at the ripple frequency of the power supply. Although the voltage ripple is typically about 4%, because of the non-linear dependence of spontaneous emission on current and the non-linear electrical characteristics of the discharge, the ripple on the spontaneous emission sidelight is around 10%. The reference signal for the lock-in amplifier is provided by a phototransistor (OCP 71) sampling the laser radiation outside the cavity. The detection system is illustrated in fig. 2.3.

The light collection efficiency is limited by two requirements; first, the maximum slit width of the monochromator must be less than 0.02 mm to resolve the 4p and 4d transitions, and second, the photomultiplier must be operated well within the linear region. (The method for checking linearity is discussed later). The latter requirement is met if the anode current is less than 20 μA (0.2 V across a 10 kΩ anode load resistance). In practice the two restrictions are compatible in that anode currents due to the more intense 4p and 4d transitions are less than 100 μA at slit widths around 0.02 mm. This value may be checked against the spontaneous emission data given in table A.2 for the 4p transitions. Typically the number of photons emitted by a 4p transition under the present discharge conditions is about $10^{18} s^{-1} cm^{-3}$.

Since the axis of the discharge tube is normal to the monochromator slit, the effective volume of discharge sampled by imaging on to the slit at unit magnification is of the order of the slit width times the square of the diameter of the discharge tube ($2 \times 10^{-3} \times 0.2^2$ cm^3), and so the photon flux into the monochromator is 10^{11} s^{-1} for an f10 aperture. The quantum efficiency of the S-20 photocathode of the 9558B phototube is 20% at 5000Å, and the overall cathode to anode gain of the tube is 10^6. If transmission losses are neglected, the expected current at the anode of the phototube is therefore 3×10^{-3} A, implying a voltage of 30 V across an anode load resistance of 10 kΩ. In view of the uncertainty in the 4p transition rate and transmission losses through the optical system, this is in reasonable agreement with the observed voltage.

We now examine the sources of noise in the detection system. It will be shown that the principle source is the dc component of the spontaneous emission. Let I_o, I_p and I_D denote currents due to the dc signal, the perturbation signal (rms) and dark current respectively. Then the rms shot noise current within a bandwidth Δf is given approximately by[2]

$$i_s^A = \{2eG(I_o^A + I_D^A)\ \Delta f\}^{\frac{1}{2}},$$

where the superscript A denotes values measured at the anode and G is the gain of the phototube. If Johnson noise introduced by the anode load resistor (R) is included, the total rms noise current at the anode is

$$i^A = \{2eG(I_o^A + I_D^A)\ \Delta f + \frac{4kT}{R}\ \Delta f\}^{\frac{1}{2}},$$

where T is the absolute temperature. The current at the anode due to the perturbation signal is related to the dc current by

$$i_p^A = f\ I_o^A,$$

where f may be as small as 10^{-3}. The noise-to-signal ratio at the output of the photomultiplier in a bandwidth Δf about the chopping frequency is therefore

$$N/S = \frac{1}{f}\frac{1}{I_o^A}\{2eG(I_o^A + I_D^A)\ \Delta f + \frac{4kT}{R}\ \Delta f\}^{\frac{1}{2}}.$$

It may be seen that with an anode dark current[2] of 2nA, an anode load resistor of 10 kΩ and a cathode to anode gain of 10^6, the Johnson noise is negligible, and hence we have

$$N/S = \frac{1}{f}\{\frac{2eG}{I_o^A}(1 + \frac{I_D^A}{I_o^A})\Delta f\}^{\frac{1}{2}}.$$

To minimize the above ratio the dark current needs to be much less than the dc current - a requirement that is met in the present case. The effective bandwidth of the sampling is determined by the time constant of the lock-in amplifier, and is about 0.02 Hz when the latter is 10 s. For typical values of I_o^A, I_D^A, f and G, the noise to signal ratio is about 3%. The equivalent rms noise voltage associated with the above is approximately 1 μV across the anode load resistor, and as such is much greater than the equivalent input noise associated with the pre-amplifier and lock-in amplifier (150 nV Hz^{-1}). This is confirmed by the marked decrease in noise level when the monochromator slits are closed.

In practice, the noise levels associated with the perturbation signals on the 4p and 4d transitions are larger than expected on the basis of shot noise alone, being around 10% (see for example figs. 5.1 - 5.5). Other possible sources of noise are fluctuations in the spontaneous emission due to discharge noise, and fluctuations in the perturbation signals due to noise associated with the laser radiation. There is insufficient information regarding these sources to comment on them quantitatively.

Since small intensity changes in the presence of large intensities are being measured it is important that the photomultiplier is operated well into the linear region. A sensitive method of checking linearity is provided by the technique itself. It involves measuring the ratio of the perturbation signal to the dc signal under constant

laser conditions but varying the light collection efficiency of the monochromator, for example, by varying the slit width or introducing neutral density filters. If the photomultiplier is linear, the ratio of the two remains constant. For anode currents less than about 20 μA the ratio was found to be constant to within the random scatter, and for subsequent measurements the anode current was restricted to below 10 μA.

The discharge must be optically thin for 4p - 4s and 4d - 4p transitions when viewed from the side of the tube. This was confirmed by comparing the fractional perturbations for two transitions with a common upper level, but with lower levels of widely differing lifetimes. For an optically thin discharge, the fractional perturbations are the same for both transitions. Fig. 2.4 shows the ratio of the fractional perturbation for the transition 4p $^2D_{5/2}$ - 4s $^4P_{3/2}$ (4228Å) to that for the transition 4p $^2D_{5/2}$ - 4s $^2P_{3/2}$ (4880Å) as a function of discharge current, the system lasing at 4880Å. The 4s $^4P_{3/2}$ level has a long lifetime (27 nS, see table A.3) compared to that of the 4s $^2P_{3/2}$ level (0.4 nS), and hence, on the assumption that the excitation rates to these lower levels are not widely different (see Appendix A.4.2), the ratio of the fractional perturbations for these two transitions is particularly sensitive to optical thickness effects. Within the limits imposed by the scatter, the results indicate that the discharge is optically thin when viewed from the side. This is also confirmed by other pairs of transitions having common upper levels, but different lower levels (see table 5.1).

References (Ch. 2)

1 Maitland A 1969 J Phys D Appl Phys 2 535

2 Photomultiplier Tubes, EMI Electronics Ltd Hayes Middlesex, brochure ref P001/fP70

3 Mullard Technical Communications 1964 7 no 68

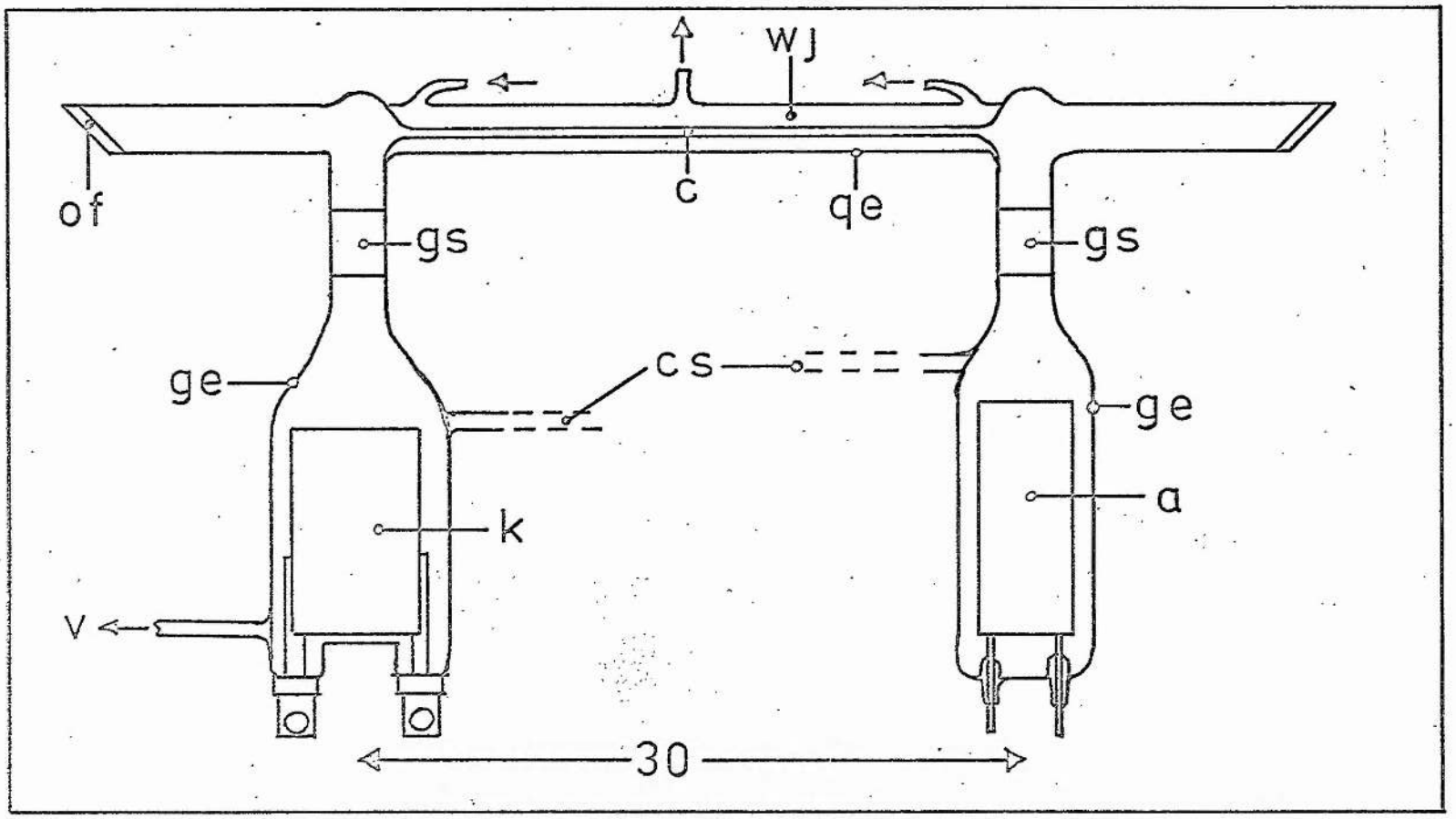

Figure 2.1 (a) DC argon ion laser of conventional design.
of optical flat; ge glass envelope; gs graded seal, quartz to pyrex; k hot oxide-coated cathode; cs cataphoresis spiral, typically 10 turns 3" in diameter; c capillary in quartz; qe quartz envelope; wj water cooling jacket; a anode in nickel; v connection to vacuum and gas filling system.

Dimension in cm.

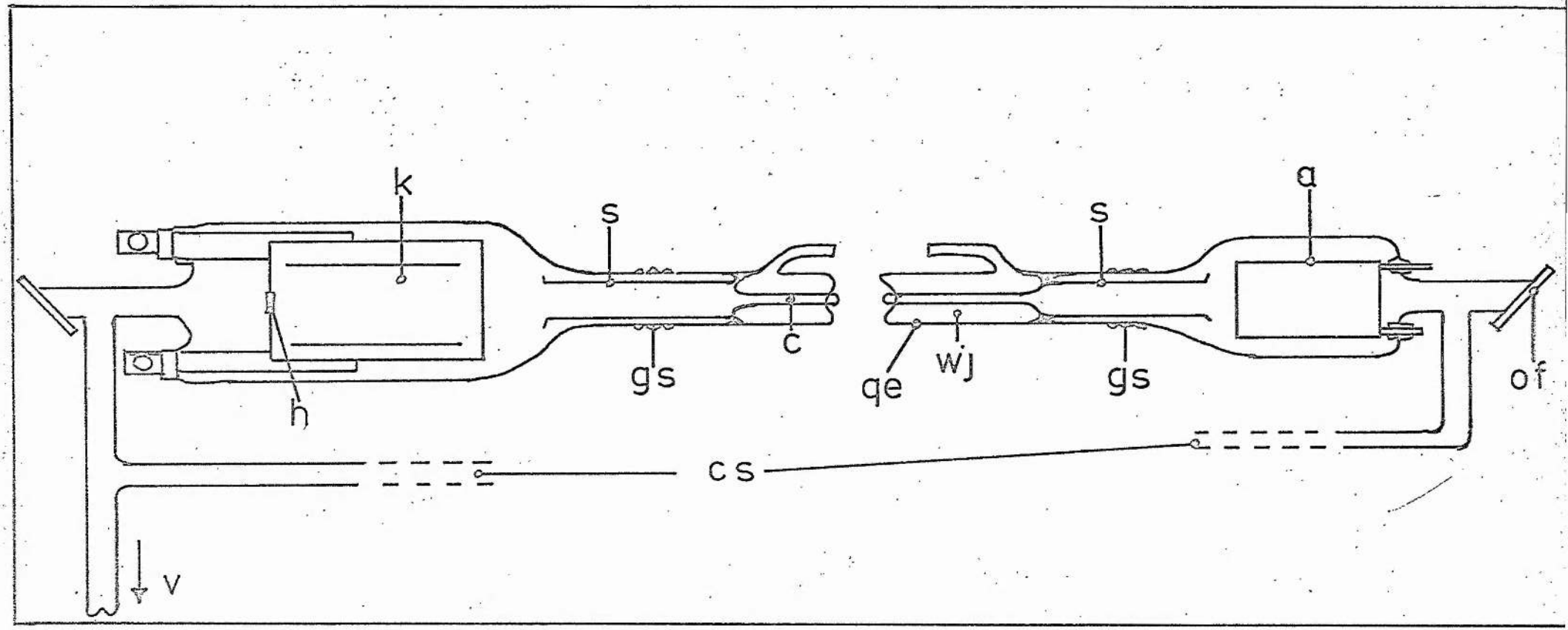

Figure 2.1 (b) DC argon ion laser of straight-through design.
of optical flat; ge glass envelope; gs graded quartz to pyrex seal;
s inner sleeve in quartz to protect graded seal; c quartz capillary
qe quartz envelope; wj water jacket; a anode; cs cataphoresis spiral
h circular hole in cathode .

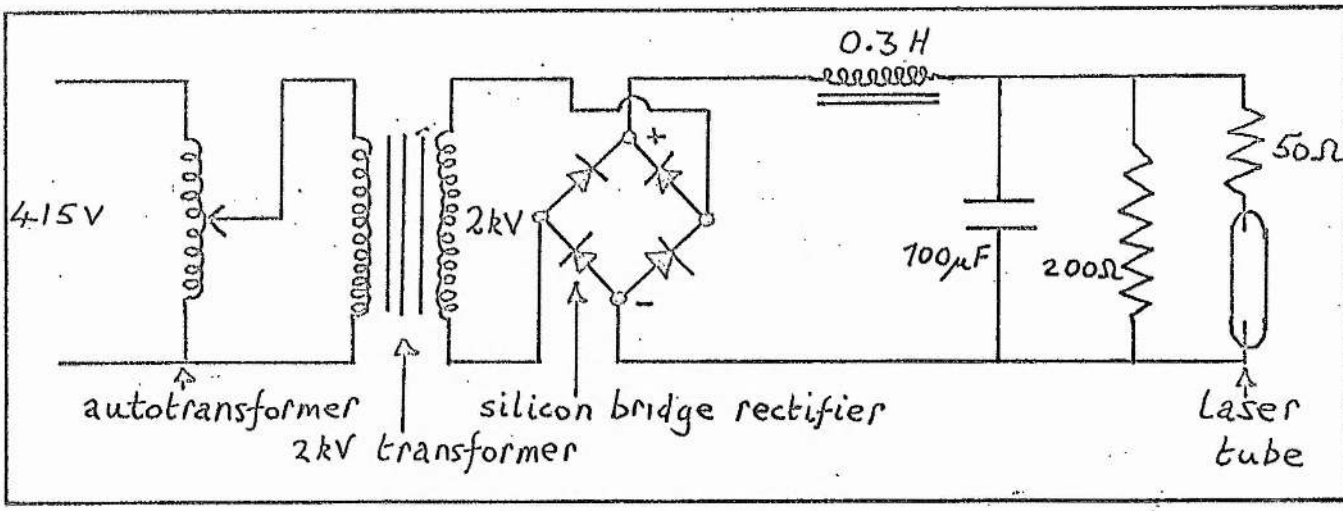

Figure 2.2 D.C. power supply for argon laser.

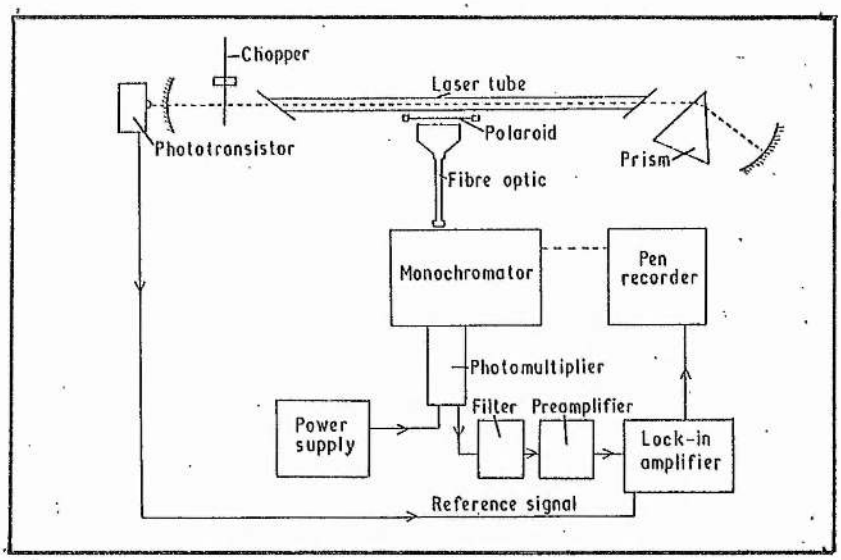

Figure 2.3 Detection system to monitor perturbation spectrum.

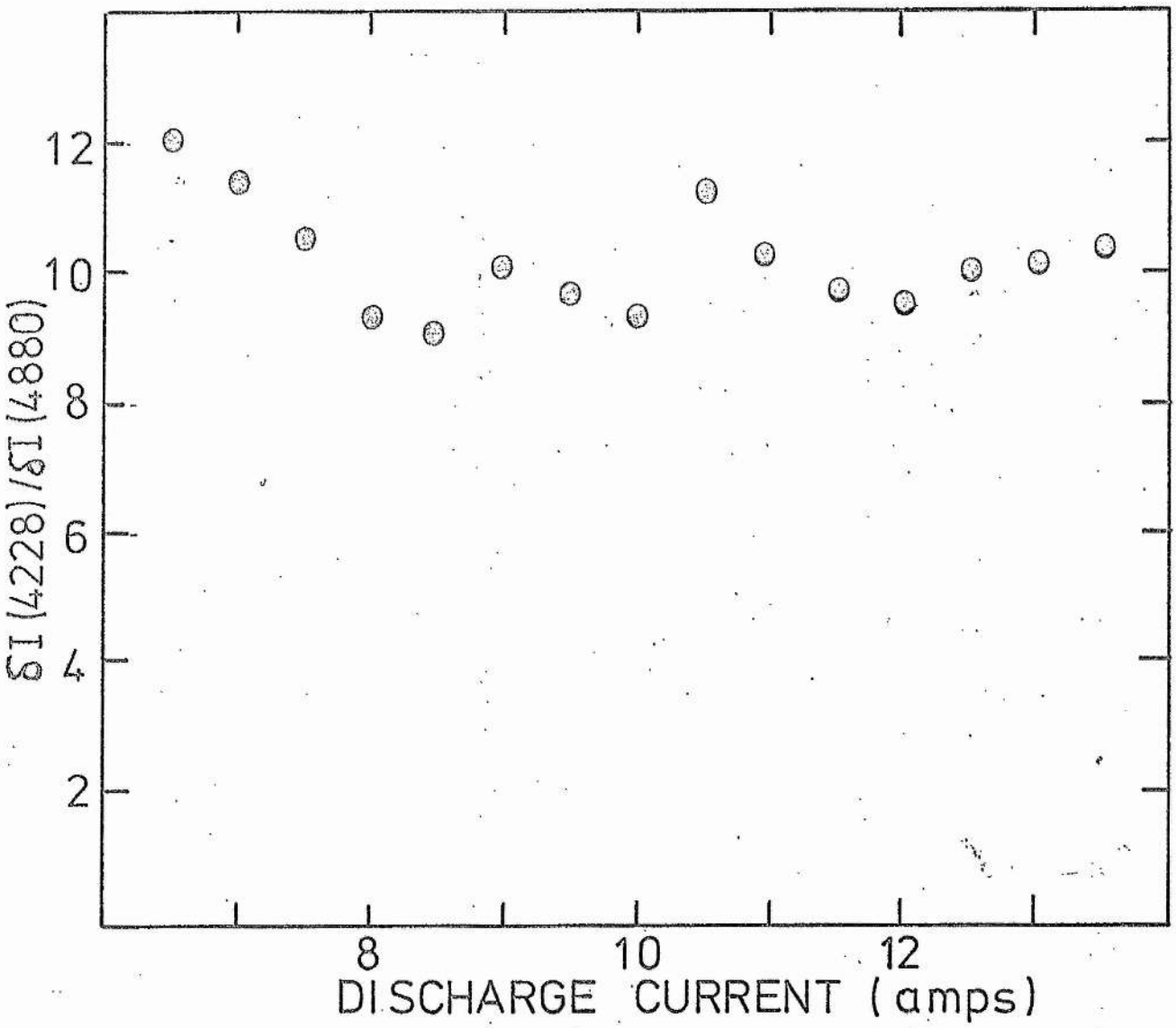

Figure 2.4 Ratio of the fractional perturbation at 4228 Å to that at 4880 Å as a function of discharge current.

CHAPTER 3

MEASUREMENT OF POPULATION INVERSIONS

3.1 Introduction

In this chapter the population changes that occur on the upper laser levels due to stimulated emission or absorption are considered. It has already been demonstrated (ch1,§3) changes can be used to determine population inversions in the active medium. After a more rigorous theoretical treatment (ch3,§2), the results obtained for the 4880Å and 5145Å laser transitions in argon are considered in relation to proposed pumping mechanisms (ch3,§3). Polarization effects that arise as a consequence of the polarized nature of the laser radiation are neglected in this chapter, since the detection apparatus was made insensitive to polarization (ch.2) for these experiments.

3.2 Theory

The arrangement of the experiment is illustrated in fig. 1.2(b). Quasi-monochromatic radiation from the laser is passed axially through the active medium contained in the external cell. The ensuing population change in the upper laser level is investigated by monitoring the intensity change in the spontaneous emission sidelight associated with a transition from this level.

The spectral distribution of the illuminating radiation may be described by

$$\delta I_L(\nu) = I_L \, n(\nu,\nu_p)\delta\nu \, , \qquad (3.1)$$

where $\delta I_L(\nu)$ is the integrated intensity† of the radiation lying in a bandwidth $\delta\nu$ about ν. Since laser radiation is quasi-monochromatic,

---

† By integrated intensity in this context is meant the radiation energy falling on unit area in unit time, without regard to solid angle. In fact this is an incorrect usage of the term, but in practice such a definition is generally adopted in the literature when highly directional beams are considered.

$n(\nu,\nu_p)$ is significantly different from zero only over a narrow frequency interval $\Delta\nu_p$ which is centered on ν_p and is such that

$$\Delta\nu_p/\nu_p << 1 . \tag{3.2}$$

The function $n(\nu,\nu_p)$ is normalized, I_L being the total integrated intensity of the illuminating radiation.

Rate equations describing the populations of the upper and lower laser levels in the absence of coherent radiation have already been given in (ch1,§3), and are

$$R_1 = N_1\tau_1^{-1} \tag{3.3}$$

$$A_{12}N_1 + R_2 = N_2\tau_2^{-1}, \tag{3.4}$$

where the symbols have already been defined. (The term describing explicitly the coupling of the upper laser level to a particular general level has been disregarded.)

The influence of the perturbing radiation on the population of the upper level is now considered. Since this radiation has a centre frequency ν_p close to that associated with the energy gap between the two levels, stimulated emission and absorption take place. The effect of stimulated emission is to increase the number of downward transitions from the upper to the lower level, whereas the effect of absorption is to cause transitions from the lower level to the upper level. Whether the net effect of these two processes is to cause an overall increase or decrease in the population of the upper level depends on the relative populations of the two levels.

Line broadening effects are important when considering the details of the coupling between the coherent radiation and the medium. The general case when inhomogeneous, as well as homogeneous, broadening occurs will be treated. Inhomogeneous broadening refers to the situation in which the atoms, in both the upper and lower levels of the transition, exhibit a distribution of resonance frequencies, and not a single resonance frequency. The source of inhomogeneous broadening in the argon

ion laser is the Doppler effect, and this will be the case considered explicitly here. The approach is to write the rate equations in the presence of laser radiation in differential form.

As a consequence of the distribution of thermal velocities associated with the atoms in a gaseous medium, the atoms exhibit a distribution of resonance frequencies when observed in the laboratory frame of reference. If $\delta N_1(\nu)$ is the number of atoms in the upper level with resonance frequency in the interval $\delta\nu$ about ν for light propagating in a given direction, then,

$$\delta N_1(\nu) = N_1 D(\nu,\nu_o)\delta\nu \,, \qquad (3.5)$$

where $D(\nu,\nu_o)$ is the normalized Doppler function centred on ν_o, the resonance frequency of a stationary atom.

When the atoms exhibit a thermal equilibrium distribution of kinetic energies, the Doppler function is[1]

$$D(\nu,\nu_o) = \frac{2(\ell n 2)^{\frac{1}{2}}}{\pi^{\frac{1}{2}}\,\Delta\nu_D} \exp\left(-\frac{(4\ell n 2)(\nu-\nu_o)^2}{(\Delta\nu_D)^2}\right) , \qquad (3.6)$$

where $\Delta\nu_D$ is the Doppler width (full width at half maximum), which is related to the kinetic temperature T and atomic mass m according to

$$\Delta\nu_D = 2\nu_o \left(\frac{2kT}{mc^2}\ \ell n\ 2\right)^{\frac{1}{2}} . \qquad (3.7)$$

The population of the lower level is described by a similar expression, namely

$$\delta N_2(\nu) = N_2 D(\nu,\nu_o)\delta\nu \,. \qquad (3.8)$$

If it is assumed that the distribution of resonance frequencies for the atoms is a consequence of different excitation rates to the different groups of atoms, then the rate at which a particular group in the upper level is supplied is given by

$$\delta R_1(\nu) = R_1 D(\nu,\nu_o)\delta\nu \,, \qquad (3.9)$$

with a similar expression for the lower level

$$\delta R_2(\nu) = R_2 D(\nu,\nu_o)\delta\nu \,. \qquad (3.10)$$

If all the atoms in the distribution exhibit similar relaxation processes,

then rate equations of the form of (3.3) and (3.4) can be written down for each group of atoms. For the upper level (3.3) becomes

$$\delta\omega R_1 D(\nu,\nu_o) = \delta N_1(\nu).\tau_1^{-1} \quad , \tag{3.11}$$

and for the lower level (3.4) becomes

$$A_{12}\delta N_1(\nu) + R_2 D(\nu,\nu_o)\delta\nu = \delta N_2(\nu).\tau_2^{-1} \quad . \tag{3.12}$$

It is now possible to consider the influence of the perturbing radiation on the populations of the upper and lower levels of the resonance transition. For the group of atoms $\delta N_1(\nu')$ in the upper level with resonance frequencies in the range $\delta\nu'$ about ν', the rate of loss, by stimulated emission, to the lower level due to radiation of intensity $\delta I_L(\nu)$ in the frequency interval $\delta\nu$ about ν is[1]

$$\delta\left\{\left(\frac{d}{dt}\{\delta N_1(\nu')\}\right)_\nu\right\} = -B_{12}\frac{\delta I_L(\nu)}{4\pi} . L(\nu,\nu')\,\delta N_1(\nu') , \tag{3.13}$$

where B_{12} is the Einstein B - coefficient for stimulated emission, which is related to the A - coefficient through

$$B_{12} = \frac{c^2}{2h\,\nu^3} A_{12} \quad , \tag{3.14}$$

and $L(\nu,\nu')$ is the Lorentz function

$$L(\nu,\nu') = \frac{(2\pi)^{-1}\,\Delta\nu_H}{(\nu-\nu')^2 + (\Delta\nu_H/2)^2} \quad , \tag{3.15}$$

where $\Delta\nu_H$ is the homogeneous linewidth (full width at half maximum) for the transition.

If the spectral distribution of the perturbing radiation ($\eta(\nu,\nu_p)$) is very much broader than the natural linewidth (i.e. $\Delta\nu_p \gg \Delta\nu_H$) - this is the case when the laser is oscillating multimode - then after substitution in (3.13) for $\delta I(\nu)$ according to (3.1), the resulting expression can be integrated over $\delta\nu$, since over the region where $L(\nu,\nu')$ changes rapidly, $\eta(\nu,\nu_p)$ is constant and so may be taken outside the integral. This gives

$$\frac{d}{dt}\{\delta N_1(\nu')\} = -\frac{B_{12} I_L}{4\pi}\,\eta(\nu',\nu_p)\,\delta N_1(\nu') = -S(\nu',\nu_p)\,\delta N_1(\nu') . \tag{3.16}$$

In a similar way, the rate at which the population distribution in the upper level is pumped by absorption can be derived and is

$$\frac{d}{dt}\{\delta N_1(\nu')\} = + S(\nu', \nu_p)\frac{g_1}{g_2}\ \delta N_2(\nu') \quad , \tag{3.17}$$

where g_1 and g_2 are the statistical weights of the upper and lower levels respectively.

The rate equation describing the population distribution in the upper level in the presence of coherent radiation is therefore

$$R_1 D(\nu', \nu_o)\delta\nu' + S(\nu', \nu_p)\left(\frac{g_1}{g_2}\delta N_2(\nu') - \delta N_1(\nu')\right) = \tau_1^{-1}\delta N_1(\nu'). \tag{3.18}$$

The rate equation describing the population distribution in the lower level can be derived in a similar fashion to (3.18) and is

$$R_2 D(\nu', \nu_o)\delta\nu' + A_{12}\delta N_1(\nu') - S(\nu', \nu_p)\left(\frac{g_1}{g_2}\delta N_2(\nu') - \delta N_1(\nu')\right) = \tau_2^{-1}\ \delta N_2(\nu') \ . \tag{3.19}$$

Since it is the change in the population distribution due to the coherent radiation that is of interest here, $\delta N_1(\nu')$ and $\delta N_2(\nu')$ are written in the form

$$\begin{aligned} \delta N_1(\nu') &= \delta N_1{}^{o}(\nu') + \delta\{\delta N_1(\nu')\} \\ \delta N_2(\nu') &= \delta N_2{}^{o}(\nu') + \delta\{\delta N_2(\nu')\} \quad , \end{aligned} \tag{3.20}$$

where $\delta N_1{}^{o}(\nu')$ and $\delta N_2{}^{o}(\nu')$ refer to the unperturbed population distributions, and $\delta\{\delta N_1(\nu')\}$ and $\delta\{\delta N_2(\nu')\}$ are the changes produced by the radiation field. By substitution of (3.20) into (3.18) and (3.19) and using (3.11) and (3.12) the following is obtained for $\delta\{\delta N_1(\nu')\}$

$$\delta\{\delta N_1(\nu')\} = \frac{-\tau_1 S(\nu', \nu_p)\left(\delta N_1{}^{o}(\nu') - \frac{g_1}{g_2}\delta N_2{}^{o}(\nu')\right)}{S(\nu', \nu_p)\left(\tau_1 + \frac{g_1}{g_2}\tau_2(1 - \tau_1 A_{12})\right) + 1} \ . \tag{3.21}$$

If the perturbation in the population distribution produced by the radiation field is small

(ie $\delta\{\delta N_1(\nu')\} \ll \delta N_1(\nu')$) then

$$S(\nu', \nu_p)\,\tau_1 \ll 1$$

$$S(\nu', \nu_p)\,\tau_2 \ll 1 \quad ,$$

and (3.21) may be approximated to

$$\delta\{\delta N_1(\nu')\} = -\tau_1 S(\nu', \nu_p)\{\delta N_1^{\circ}(\nu') - \frac{g_1}{g_2}\delta N_2^{\circ}(\nu')\} . \qquad (3.22)$$

The above must now be integrated over the inhomogeneous line profile in order to determine the total change in the population of the upper level. In the case when the spectral distribution of the perturbing radiation is similar to that associated with the resonance transition - for multimode oscillation of the laser this would be approximately the case - ie when

$$\eta(\nu, \nu_p) \equiv D(\nu, \nu_o) \qquad (3.23)$$

and

$$\nu_p \equiv \nu_o ,$$

(3.22) may be integrated to obtain

$$\delta N_1 = -\frac{\tau_1 B_{12} I_L}{4\pi}\left(N_1^{\circ} - \frac{g_1}{g_2}N_2^{\circ}\right)\int_0^{\infty} D^2(\nu', \nu_o)d\nu' . \qquad (3.24)$$

After performing the integration over the Doppler profile using (3.6) and substituting for B_{12} according to (3.14), the following is obtained for the fractional change in the population of the upper level

$$\frac{\delta N_1}{N_1^{\circ}} = -\left(\frac{2\ell n 2}{\pi}\right)^{\frac{1}{2}} \cdot \frac{\lambda_o^2}{8\pi h\nu} \cdot \frac{I_L}{\Delta\nu_D} \cdot \tau_1 A_{12}\left(1 - \frac{g_1 N_2^{\circ}}{g_2 N_1^{\circ}}\right) . \qquad (3.25)$$

For radiation in the visible region of the spectrum, the above may be evaluated to give

$$\frac{\delta N_1}{N_1^{\circ}} = -1.6 \times 10^5 \cdot \frac{I_L}{\Delta\nu_D} \cdot \tau_1 A_{12}\left(1 - \frac{g_1 N_2^{\circ}}{g_2 N_1^{\circ}}\right) , \qquad (3.26)$$

where I_L is in mW cm^{-2} and $\Delta\nu_D$ is in Hz.

The fractional change in the population of the upper level is determined by measuring the fractional change in the spontaneous emission sidelight ($\delta I/I$) associated with transitions from the upper level, since

$$\delta I/I = \delta N_1/N_1^{\circ} . \qquad (3.27)$$

Examination of (3.25) illustrates how the technique may be used to investigate population inversions. When a population inversion exists,

ie when

$$g_1 N_2^{\,o}/g_2 N_1^{\,o} < 1 \ ,$$

the perturbing radiation decreases the spontaneous emission sidelight from transitions originating on the upper level. When there is no population inversion, ie when

$$g_1 N_2^{\,o}/g_2 N_1^{\,o} \geq 1,$$

the perturbing radiation now increases the spontaneous emission sidelight from transitions originating on the upper level. The dependence of population inversions on conditions in the active medium (such as gas pressure, discharge current, etc) can therefore be explored by studying changes in the spontaneous emission sidelight.

In the case when a population inversion is established to such an extent that the population of the upper level is much greater than the population of the lower level, the fractional population change on the upper level tends to a limiting value given by

$$(\delta N_1/N_1^{\,o})_{max} = -\ 1.6 \times 10^5 \frac{I_L}{\Delta\nu_D}\ \tau_1 A_{12}$$

$$= -\ 1.6 \times 10^5 \frac{P_o}{a\ \Delta\nu_D}\ \tau_1 A_{12} \ , \qquad (3.28)$$

where P_o is the total power and a the cross-sectional area of illuminating radiation. In the case when the lifetime of the upper level is determined only by radiative decay to the lower level (ie when $\tau_1 A_{12} = 1$), the fractional change is independent of the transition probability and depends only on the intensity and linewidth of the illuminating radiation.

Since the interest here is the application of the technique to a study of population inversions in the argon ion laser, typical values for the fractional population changes are tabulated in table 3.1 for 4880 Å and 5145 Å perturbing radiation. Experimentally determined values, to be discussed in the next section, are also included. It will be seen that the changes are small. For example, in the case when the medium

is illuminated by 4880 Å radiation of power 100 mW, the fractional change expected is only 3%. Phase sensitive detection techniques are, however, well suited to the observation of the population changes. The illuminating radiation is modulated at a fixed frequency, and the changes produced in the spontaneous emission sidelight at the same frequency are observed by phase sensitive detection.

As a method of determining gain or absorption, observation of upper level population perturbations has advantages over more conventional methods[2]. This is particularly so when small gain (or absorption) coefficients are involved. For example, in the standard method where the change in intensity of the radiation as it propagates through the medium is measured, it is difficult to use phase sensitive detection techniques, since these involve modulating the active medium. In principle the difference between standard gain measuring techniques and the sidelight method discussed above is that in the former the resonance radiation is perturbed by the medium, whereas in the latter the medium is perturbed by the resonance radiation. Since it is much easier to modulate the radiation field than to modulate the active medium, phase sensitive detection techniques can be readily applied in the latter case, but not in the former.

The sidelight method, however, is only sensitive in the region of change-over from gain to absorption (ie where $N_1/g_1 \simeq N_2/g_2$). Once large inversions have been established the fractional change in sidelight radiation becomes independent of level populations.

3.3 Experimental observations

Experimental details have already been discussed in ch. 2. The argon discharge studied was in a water cooled quartz capillary, 4 mm in diameter and about 10 cm long. Illuminating radiation was provided

by an argon ion laser oscillating at either 4880 Å ($4p\ ^2D_{5/2} - 4s\ ^2P_{3/2}$) or 5145 Å ($4p\ ^4D_{5/2} - 4s\ ^2P_{3/2}$). In the former case the population change on the upper level was studied by monitoring the spontaneous emission radiation at 4228 Å ($4p\ ^2D_{5/2} - 4s\ ^4P_{3/2}$) and in the latter case by that at 4426 Å ($4p\ ^4D_{5/2} - 4s\ ^4P_{3/2}$). By using transitions different from the laser transitions, difficulties arising from scattered laser radiation were avoided. Typically the output power of the laser at 4880 Å was 600 - 700 mW and at 5145 Å 300 - 350 mW, in both cases spread over a beam diameter in the capillary discharge of just under 4 mm.

In figures 3.1 and 3.2 the dependences of the fractional modulations (% mW^{-1}) of the sidelight radiation at 4228 Å and 4426 Å respectively on argon filling pressure is shown for a constant discharge current of 10 A (80 A cm^{-2}). At pressures below 120 mTorr, the fractional modulations approach constant values of approximately 8×10^{-3}% mW^{-1} for the $4p\ ^2D_{5/2}$ level and 1.5×10^{-3}% mW^{-1} for the $4p\ ^4D_{5/2}$ level. If allowance is made for uncertainties in beam diameter and for the non-uniform spatial distribution of the laser radiation, both are in reasonable agreement with limiting values of 3×10^{-3}% mW^{-1} and 2×10^{-3}% mW^{-1} respectively derived theoretically in (ch3,§2).

However, before the perturbations can be interpreted in terms of reduced number densities

$$\tilde{N} = \left(1 - \frac{g_1 N_2^{\,o}}{g_2 N_1^{\,o}}\right) ,$$

the various assumptions made in (ch3,§2) must be examined in relation to conditions in the argon discharge.

(i) In equation (3.27) it was assumed that the fractional change in upper level population is equal to the fractional change in spontaneous emission sidelight for transitions originating from that level. This is the case only if the discharge is optically thin on that transition

when viewed at right angles to the tube axis. Experimental evidence that the discharge is optically thin for 4p - 4s transitions has already been considered in ch. 2, where fractional perturbations on two transitions (4880 Å, 4228 Å) originating from the same upper level but terminating on lower levels with widely different lifetimes were found to be equal over an extended range of discharge parameters.

Also, it can be shown that the discharge is optically thin on a particular transition if[5]

$$k_o D \ll 1 \quad , \tag{3.29}$$

where k_o is the absorption coefficient at line centre and D is the tube bore. For a Doppler broadened line

$$k_o = \frac{2}{\Delta\nu_D}\left(\frac{\ell n 2}{\pi}\right)^{\frac{1}{2}} \frac{\lambda_o^{\,2} g_m}{8\pi\, g_n} A_{mn} N_n \quad , \tag{3.30}$$

where upper level effects have been neglected and N_n is the population of the lower level. For the 4p - 4s transitions with large transition probabilities ($A_{12} \sim 8 \times 10^7 s^{-1}$, table A.2) and for a 4 mm bore tube $k_o D$ is $6 \times 10^{-13} N_n$ where N_n is in units of cm^{-3}. Kitaeva et al[6] (Appendix A) have calculated that the total pumping rate to all levels of the 4s configuration does not exceed $2 \times 10^{19} s^{-1} cm^{-3}$ for current densities up to 330 A cm^{-2} and pressures up to 0.62 Torr, and most of this pumping is expected to be to the short lived doublet 4s levels. On the basis of comparable pumping to all 4s levels and using a calculated lifetime for the long lived 4s $^4P_{3/2}$ level of 27×10^{-9} s (table A.3), the maximum population of a quartet 4s level is unlikely to exceed 10^{11} cm^{-3}. The maximum $k_o D$ value is therefore around 0.06, so confirming the experimental observation that the discharge is optically thin on 4p - 4s transitions.

(ii) In equation (3.23) similar line profiles for the perturbing (laser) radiation and for the resonance transition in the discharge were assumed. For this to be a reasonable approximation the laser must oscillate

multimode so that radiation is emitted across most of its gain profile, the gain profile must be similar to the line profile of the resonance transition and any relative shift in centre frequencies due to ion drift must be small. The first requirement was fulfilled by operating the laser well above threshold and by choosing a suitable combination of mirrors to allow oscillation of high order transverse modes. Examination of the power output with a scanning Fabry Perot interferometer confirmed that oscillation was indeed multimode. Since the Doppler linewidth depends on the square root of the absolute ion temperature and this has been shown to be only weakly dependent on discharge current and virtually independent of pressure in the argon discharge[7] (Appendix A), the second requirement is satisfied. Information on axial drift velocities for the ions is inconsistent between different investigators, but maximum values do not exceed about 2×10^4 cm s^{-1} (Appendix A). Since the half-width of the Doppler broadened line corresponds to an ion velocity of about 2×10^5 cm s^{-1}, displacement of the two profiles is unlikely to exceed one tenth of their width at the most, and the third requirement is therefore fulfilled. While differences in linewidth could lead to changes in the magnitude of the fractional perturbations, they could not lead to changes of sign.

(iii) In deriving equation (3.22) fractional perturbations were assumed to be much less than unity. Maximum values observed are less than 5% and so this assumption is valid.

(iv) Finally, the dependence of the upper level lifetime τ_1 on discharge conditions must be considered. If τ_1 varies, then the fractional perturbation will vary correspondingly (equation 3.26), even though $\bar{N}$ remains constant. As discussed in Appendix A (A.3.8) Vladimirova et al report that with both increasing pressure and increasing current, 4p lifetimes decrease.

It may be seen from fig. A.17 that typically the lifetimes of the

$4p\ ^2D^o_{5/2}$ and $4p\ ^4D^o_{5/2}$ levels appear to decrease by some 30% over the pressure range 0 - 1.5 Torr and current range 0 - 11 A (2mm bore). We have repeated the lifetime measurements for the $4p\ ^2D^o_{5/2}$ level, using the technique of Vladimirova et al, over the current range 6 - 12 A and at a pressure of 150 mTorr in a 4mm bore tube.

In this technique the perturbation signal on the upper laser level is measured in the active medium of the laser oscillator itself, not an external cell, together with the coherent power output. From (1.3) and (1.5) it may be seen that

$$\delta N_1 = - P\tau_1(h\nu_{12})^{-1},$$

where P is the total coherent power extracted per unit volume. This is given by

$$P = (1 + \beta)\ P_L\ V_a^{-1},$$

where P_L is the measured output power through the coupling mirror, β allows for parasitic losses and V_a is the mode volume in the active medium. Hence we have

$$(\delta I/P_L) \propto (\delta N_1/P_L) \propto \tau_1(1 + \beta)V_a^{-1}\ .$$

Provided that the mode volume and fractional parasitic losses are constant, $(\delta I/P_L)$ is proportional to τ_1. In fig. 3.6, $\delta I(4p\ ^2D^o_{5/2})$, $P_L(4880\text{Å})$ and $(\delta I/P_L)$ are plotted as a function of discharge current. Apart from the range below 8 A where the errors are large due to small δI, $(\delta I/P_L)$ is current independent. Since the mode volume tends to increase with current and β is approximately independent of current, this implies that τ_1 is independent of discharge current for this pressure condition. For pressures and current densities of interest in the present experiments, therefore, changes in τ_1 are less than those reported by Vladimirova et al as expected.

Although some decrease in $|(\delta I/I)|$ with pressure may be expected, the observed decrease is very much larger than can be accounted for by lifetime changes, and further the change in sign cannot be account for at all in this way. With regard to the current dependence, $|(\delta I/I)|$

is found to increase with increasing current, contrary to the effect expected on the basis of lifetime changes. Thus even if, as suggested, the upper level lifetime does change, it cannot account for the principal features of the curves, but only introduces some uncertainty in the estimates of $\bar{N}$.

At pressures above 180 mTorr $\bar{N}$ decreases with increasing pressure for both transitions, reaching zero around 280 mTorr, and then becomes negative for higher pressures. This indicates that as the argon pressure increases the population inversions on both the 4880 Å ($4p\ ^2D_{5/2}$ - $4s\ ^2P_{3/2}$) and 5145 Å ($4p\ ^4D_{5/2}$ - $4s\ ^2P_{3/2}$) transitions are progressively reduced, with upper and lower level populations comparable around 280 mTorr. Since both transitions share a common lower level, and since the pressure dependence of their upper level populations is similar (fig. A.23) this similarity in $\bar{N}$ is to be expected.

The dependence of $\bar{N}$ on discharge current is shown in figs. 3.3 and 3.4 for the 4880 Å and 5145 Å transitions respectively. Although $\bar{N}$ does change from negative (absorption) to positive (gain) with increasing current, the current dependence is weak. For example, for the 4880 Å transition at a pressure of 230 mTorr the change is only from - 0.16 to + 0.03 for a current change from 5A (50A cm^{-2}) to 15A (150A cm^{-2}). The 5145 Å transition shows a similar behaviour.

In order to interpret the data on population inversions, we first analyse the proposed excitation pathways for the 4p and 4s states using the flow graph technique (Appendix B). On the basis of the discussion of excitation mechanisms given in Appendix A, the flow graph shown in fig. 3.5 has been drawn up. The excitation processes are traced only from the ion ground state (g), since the earlier steps (neutral ground state to neutral metastable state, to ion ground state) are common. From the ion ground state excitation to the 4p states can

proceed either (i) directly (r_{g1}), (ii) via some higher (4d) state followed by radiative cascade ($r_{gc}\ f_{c1}$), or (iii) via an intermediate metastable (3d, quartet 4s) state ($r_{gm}\ r_{m1}$). For the 4s doublet states excitation can proceed either (i) directly from the ion ground state (r_{g2}), or (ii) by radiative decay from the 4p states (f_{12}).

The excitation pathways to upper and lower laser levels and the first and second order loops that occur in fig. 3.5 are summarized in table 3.2. Using the loop rule (B.1) the populations of the 4p and doublet 4s states can be written as

$$N_1 = \tau_1(r_{g1} + r_{gc}\ f_{c1} + r_{gm}\ r_{m1})R_g/S, \qquad (3.31)$$

and

$$N_2 = \tau_2\left[f_{12}(r_{g1} + r_{gc}\ f_{c1} + r_{gm}\ r_{m1}) + r_{g2}(1 - r_{m1}\ f_{1m})\right]R_g/S, \qquad (3.32)$$

respectively where

$$S = 1 - \Sigma\ L(1) + \Sigma\ L(2) - \ .....$$

Expressions (3.31) and (3.32) may be applied to individual 4p and doublet 4s states if the r's and f's are regarded as averages taken over the appropriate intermediate states that are collisionally or radiatively coupled to the 4p or 4s state under consideration. In general computation of the r's and f's is difficult, but from the point of view of the subsequent argument it is the functional form of (3.31) and (3.32) that is important. If we let the statistical weight of the particular 4p state be g_1 and the particular doublet 4s state be g_2, then for the transition between them we have

$$\bar{N} = 1 - \frac{g_1}{g_2}\frac{\tau_2}{\tau_1}\left\{f_{12} + \frac{1 - r_{m1}\ f_{1m}}{(r_{g1}/r_{g2}) + (r_{gc}/r_{g2})f_{c1} + (r_{gm}/r_{g2})r_{m1}}\right\}, \qquad (3.33)$$

which may be written

$$\bar{N} = 1 - \frac{g_1}{g_2}\tau_2\ (A_{12} + C_{12}) - \frac{g_1}{g_2}\frac{\tau_2}{\tau_1}F, \qquad (3.34)$$

where

$$F = (1 - r_{m1}\ f_{1m})/\{(r_{g1}/r_{g2}) + (r_{gc}/r_{g2})f_{c1} + (r_{gm}/r_{g2})r_{m1}\}\ ,$$

and A_{12} is the Einstein coefficient for the transition 1 to 2 and C_{12} is the collisional decay rate from 1 to 2. We must now examine the various terms in (3.33) and (3.34), and in particular their dependence on discharge conditions.

The ratios (r_{g1}/r_{g2}), (r_{gc}/r_{g2}) and (r_{gm}/r_{g2}) are functions only of electron temperature. If the metastable state population is saturated with respect to the ion ground state (ie its principal decay is through electron collisions), then r_{m1} also is dependent only on electron temperature. There is some evidence (discussed in the next paragraph) that the lifetimes of the 4p states may be reduced by electron collisions. If this is the case then f_{1m} is either unaltered if the collisional decay processes branch according to the radiative transition probabilities, or decreases with increasing collisional destruction if this is partly through excitation to higher states. This argument may also be applied to the coefficient f_{c1}. It therefore follows that in the case when the metastable population is saturated with respect to the ion ground state, F is either a function of electron temperature only or a function of both electron temperature and electron density but monotonically increasing as the latter increases. In both cases F decreases with increasing electron temperature since the excitation rates to the 4p states increase more rapidly than those to the 4s states (see talbe A.8 and fig. A.32).

There is evidence that both τ_1 and τ_2 depend on discharge conditions; τ_1 because of collisional destruction of the upper laser states (see A.3.8) and τ_2 because of radiation trapping. This latter effect may be estimated by using (3.29) and (3.30) to calculate k_oD for transitions between doublet 4s levels and the ion ground state. Taking $A_{mm} \sim 2 \times 10^9\ s^{-1}$ (table A.3) and assuming an ion temperature of 3000 - 4000 K (fig. A.4), then for a 4 mm bore tube k_oD is approximately $6 \times 10^{-14} N_e$, where N_e is

the electron density (cm^{-3}) which has been assumed equal to the ion ground state density. At pressures around 200 mTorr and current densities around 100 A cm^{-2}, the discharge conditions appropriate to figs. 3.3 and 3.4, the electron density is in the range 1 - 3 x 10^{13} cm^{-3} (fig. A.8), and so k_oD is in the range 0.6 - 2 implying that radiation trapping effects are significant in increasing the lifetimes of the doublet 4s levels. It should be pointed out that this estimate of radiation trapping is only approximate in that an isotropic ion temperature and an homogeneous plasma have been assumed.

We may conclude therefore that the ratio (τ_2/τ_1) in (3.34) must either be constant or increase with increasing current since τ_1 may decrease with increasing current because of collisional destruction and τ_2 increases with increasing current because of increasing electron density (fig. A.8)

If the electron temperature is independent of discharge current, then all the processes discussed above will tend if anything to reduce $\bar{N}$ with increasing discharge current. The observation that $\bar{N}$ increases with increasing discharge current - see figs. 3.3 and 3.4 - is direct evidence that the electron temperature is increasing with increasing discharge current.

Such a conclusion is consistent with the current dependence shown by the populations of the 4p states at the higher pressures (fig. A.24). On the basis of excitation via the ion ground state or a saturated metastable state, a quadratic current dependence for the 4p states is to be expected if the electron temperature is constant. If however the electron temperature increases with increasing current then the current dependence will be greater than quadratic as is observed.

It should, hwoever, be noted that other explanations for the current dependence of $\bar{N}$ may be advanced if the generally accepted excitation

mechanisms for the 4p and 4s states are disregarded. For example, if the predominant excitation mechanism for the 4s states is from neutral metastable states rather than the ion ground state, then the excitation rate for the 4s states would be a linear function of discharge current since the neutral metastable states are saturated (see A.3.9). In such a circumstance and with a quadratic current dependence for the populations of the 4p states, the population inversion would be expected to increase with increasing discharge current, even with a constant electron temperature. The assumption that the ion metastable densities are saturated has already been pointed out. The evidence for this is discussed in A.3.9. If the metastable densities have not reached saturation then r_{m1} will be increasing with discharge current and this could then explain the increase in $\bar{N}$ with discharge current.

The decrease in $\bar{N}$ with increasing pressure for both the 4880 Å and 5145 Å transitions (fig. 3.1 and 3.2) may be explained by increasing radiation trapping for transitions from the 4s doublet states together with a decrease in the relative excitation rate to 4p states compared to 4s states (see A.4) due to decreasing electron temperature (see A.3.6). In fig. 3.1 the experimentally determined $\bar{N}$ values for the 4880 Å transition are compared with average values of $\bar{N}$ for doublet 4p - 4s transitions determined from the estimates of 4p and 4s populations made by Kitaeva et al (see table A.8). These latter refer to a higher discharge current density (160 A cm^{-2}) and a smaller bore diameter (2mm) than the experimental values (100 A cm^{-2}, 4mm), but are the only calculated values available for comparison. The condition $\bar{N} = 0$ occurs at higher pressures in this case, and this is to be expected in view of the higher discharge current density and smaller bore diameter involved.

References (Ch. 3)

1 Maitland A and M H Dunn 1969 Laser Physics North Holland Publishing Co Amsterdam

2 Heard H G 1968 Laser Parameter Measurements Handbook Wiley New York

3 Rudko R I and C L Tang 1967 J Appl Phys 38 4731

4 Bloom A L, R L Byer and W E Bell 1966 Physics of Quantum Electronics McGraw-Hill New York p 688

5 Mitchell A C G and M W Zemansky 1961 Resonance Radiation and Excited Atoms Cambridge University Press p100

6 Kitaeva V F, A N Odintsov and N N Sobolev 1970 Sov Phys - Uspekhi 99 699

7 Koster G F, H Statz, F A Horrigan and C L Tang 1968 J Appl Phys 39 4045

λ Å	Designation	τ_1 (3) (nS)	A_{12} (3) (s^{-1})	$\Delta\nu_D$ (4) (GHz)	a (cm^2)	$(\delta N_1/N_1^o)$ (mW^{-1}) theor.	exp.
4880	$4p^2D_{5/2}$–$4s^2P_{3/2}$	8.7	8.4×10^7	4	0.1	3×10^{-2}%	8×10^{-3}%
5145	$4p^4D_{5/2}$–$4s^2P_{3/2}$	6.2	9.2×10^6	4	0.1	2×10^{-3}%	1.5×10^{-3}%

Table 3.1 Limiting values of fractional perturbations on upper laser levels

Loops		Paths	
First Order	Second Order	To Upper Level (1)	Loops not Touched
m1m	m1mg2g	$R_g r_{gc} f_{c1}$	none
g2g	m1mgcg	$R_g r_{gm} r_{m1}$	none
gm1g		$R_g r_{g1}$	none
gm12g			
gc1g		To Lower Level (2)	
gcg			
mgm		$R_g r_{g2}$	m1m
gc1mg		$R_g r_{gc} f_{c1} f_{12}$	none
g1mg		$R_g r_{gm} r_{m1} f_{12}$	none
g1g		$R_g r_{g1} f_{12}$	none
g12g			

Table 3.2 Loops and paths associated with flow graph of fig. 3.5.

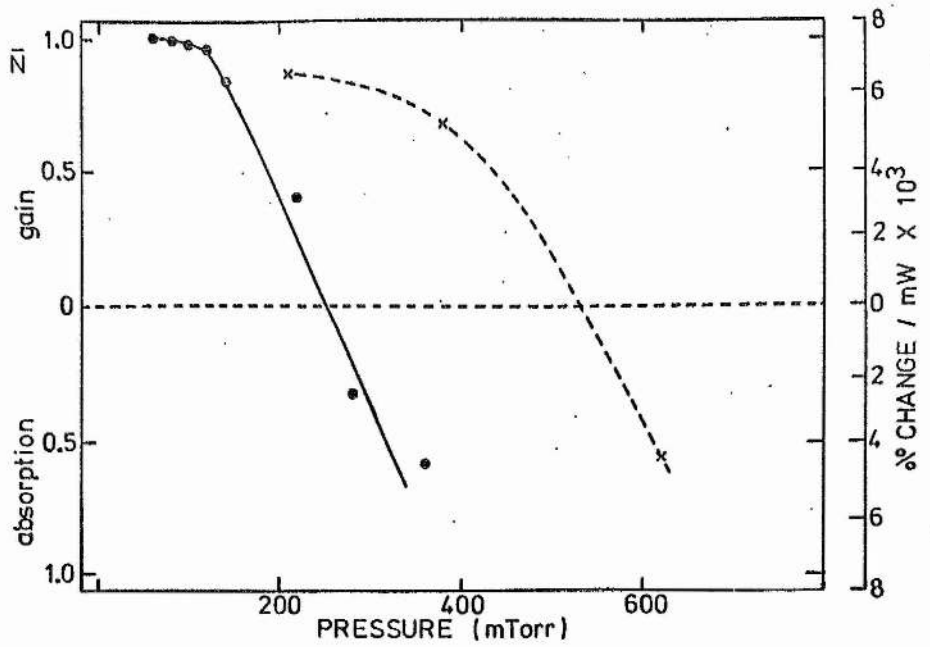

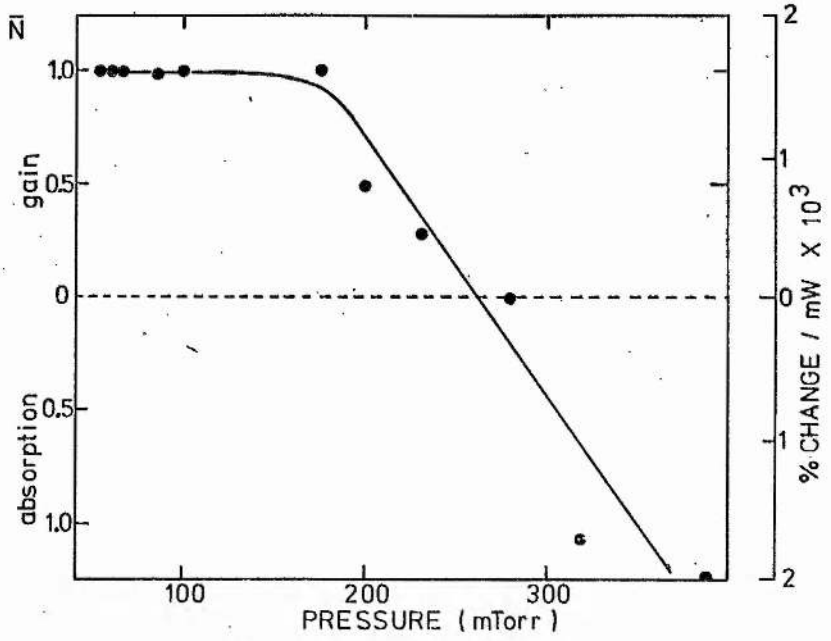

Figure 3.1 Fractional modulation at 4228A when illuminated with 4880A radiation as a function of filling pressure (mTorr). The fractional modulation is expressed as % change per mW of illuminating radiation, and N deduced from the change is also shown. Discharge current density 100 A cm^{-2}, 4mm bore tube. The dashed line shows the values of N calculated by Kitaeva at 160 A cm^{-2} in a 2mm bore tube (see Table A.8).
Figure 3.2 Fractional modulation at 4426 A when illuminated with 5145 A radiation as a function of filling pressure (mTorr). Discharge current density 100 A cm^{-2}, 4mm bore tube.

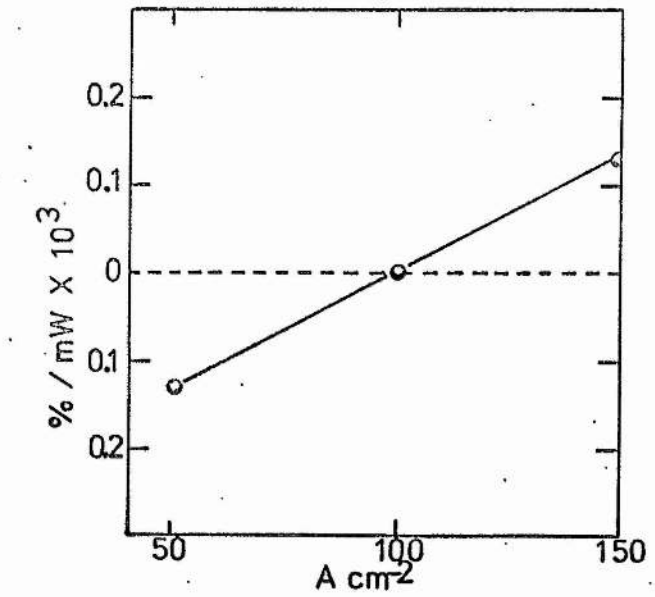

Figure 3.4

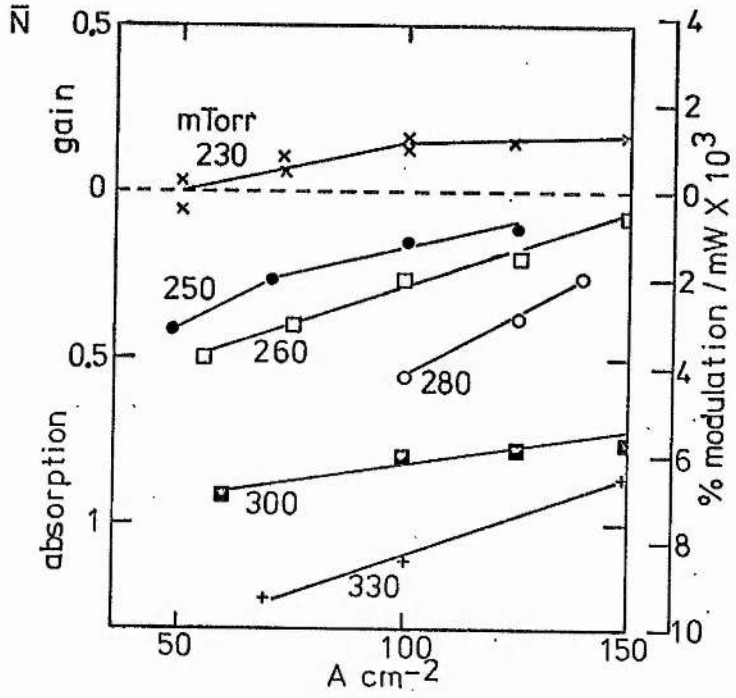

Figure 3.3

Figure 3.3 Fractional modulation at 4228 A when illuminated with 4880 A radiation as a function of discharge current (A cm^{-2}) with filling pressure as parameter (mTorr). 4 mm bore tube.

Figure 3.4 Fractional modulation at 4426 A when illuminated with 5145 A radiation as a function of discharge current (A cm^{-2}). 280 mTorr, 4 mm bore.

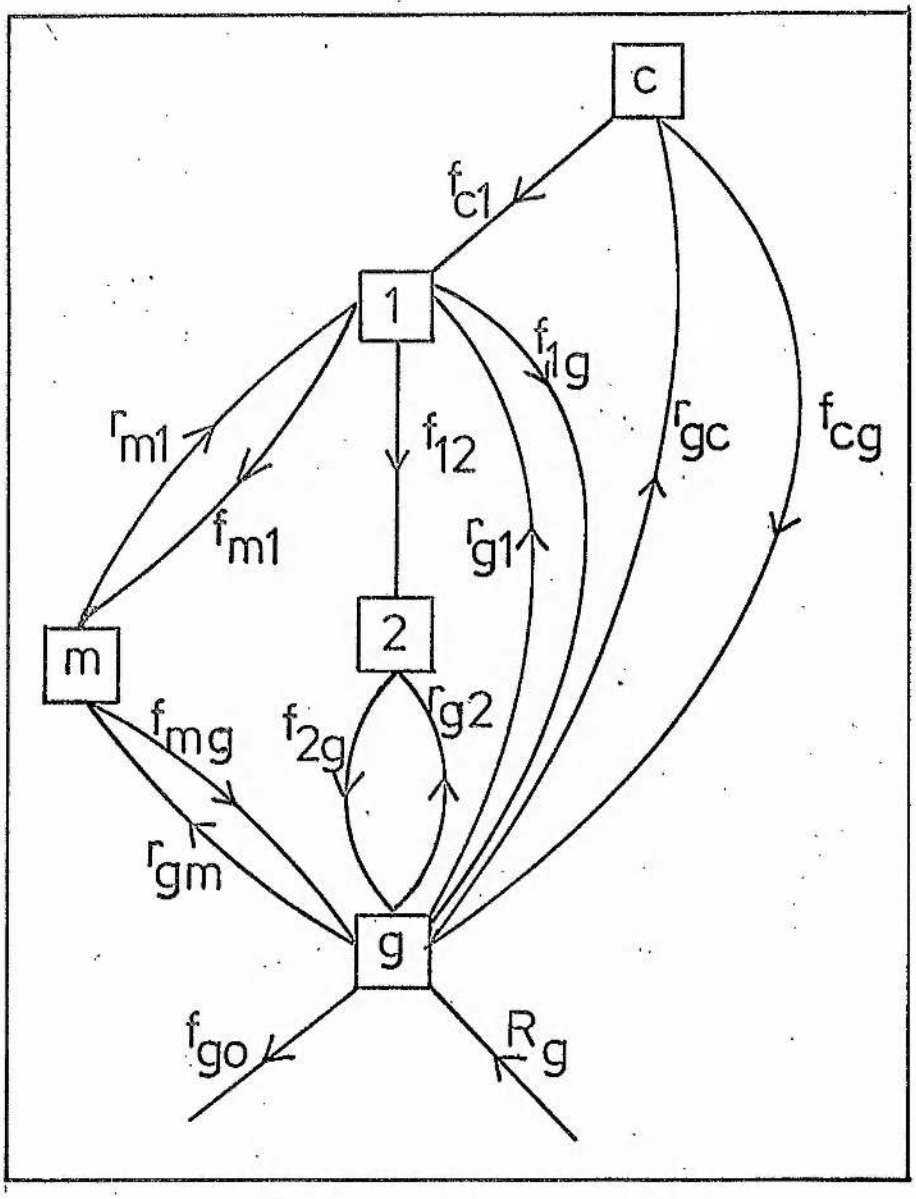

Figure 3.5 Flow graph describing excitation processes for the 4p (1) and 4s (2) ion levels. m represents a general metastable state (3d, quartet 4s), c states from which radiative cascade can occur (4d), and g the ion ground state.

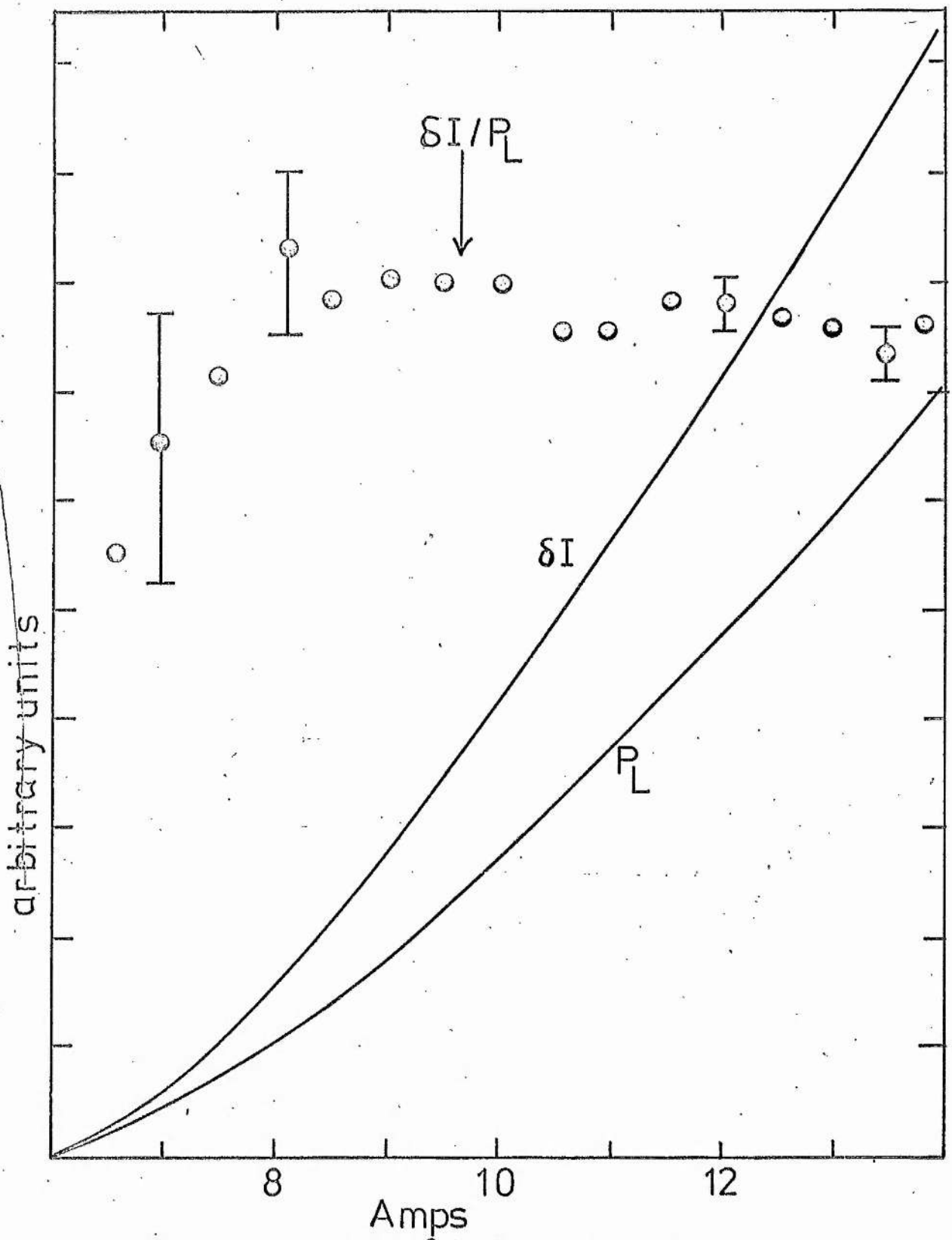

Figure 3.6 Power output at 4880 Å (P_L), perturbation in spontaneous emission from 4p $^2D_{5/2}$ level (δI) and ($\delta I/P_L$) as a function of discharge current. Filling pressure 150 mTorr, bore diameter 4 mm, oscillation at 4880 Å only. Error bars are placed on some of the ($\delta I/ P_L$) points.

CHAPTER 4

POLARIZATION IN PERTURBATION SPECTRUM

4.1 Introduction

In this chapter we consider polarization effects that arise in the perturbation spectrum as a consequence of the linear polarization of the coherent radiation within the laser cavity. In particular we are concerned with polarization effects on transitions (4880Å, 4228Å) originating on the 4p $^2D^o_{5/2}$ level, both when an axial magnetic field is applied as well as when only the self-generated magnetic field due to the discharge current is present.

First of all we discuss a simple theoretical treatment of the experiment based on a rate equation approach, then present a full semi-classical analysis to demonstrate how the polarization ratio is related to the lifetimes of excited states, and finally consider the experimental results.

4.2 Theoretical analysis by rate equations

Polarization ratios are calculated for the 4p $^2D^o_{5/2}$ - 4s $^2P_{3/2}$ (4880Å) and 4p $^2D^o_{5/2}$ - 4s $^4P_{3/2}$ (4228Å) transitions following the method formulated by Van Vleck[1]. This is done for the cases of (i) a cylindrically symmetrical magnetic field, (ii) zero magnetic field and (iii) an axial magnetic field.

The case where there is a B_ϕ field at right angles to the propagation direction of the laser radiation is first considered. Such a field arises in the discharge due to the dc discharge current, and is of magnitude

$$B_\phi = I_D \, r/5 \, R^2 \text{ gauss}, \qquad (4.1)$$

where I_D is the discharge current (A), r is the radial distance from the tube centre (cm) and R is the radius of the discharge tube ($r \leq R$). In (4.1) is has been assumed that the current density is uniform over the cross-section of the discharge tube. The geometry for this case is illustrated in figs. 4.1(a) and (b). The magnetic field direction

$\underset{\sim}{B}$, viewing direction $\underset{\sim}{V}$ and polarization direction of the laser radiation $\underset{\sim}{X}$ (direction of electric field vector) are all in the same plane and perpendicular to the propagation direction of the laser radiation ($\underset{\sim}{k}$). The angle ψ between $\underset{\sim}{V}$ and $\underset{\sim}{X}$ is zero for direction V_2 and $\pi/2$ for direction V_1. An integration must eventually be performed over ϕ to take into consideration the varying direction of the B_ϕ field in the discharge.

The Zeeman sublevels, specified by M_J of the 4s $^2P_{3/2}$ and 4p $^2D^o_{5/2}$ levels are illustrated in fig. 4.2, which also describes the polarization state of the radiation associated with transitions involving different pairs of sublevels. The steady state population of one of the upper laser sublevels in the absence of laser radiation may be written by analogy with (1.2) and (1.4) as

$$R_1(M_1) = N_1(M_1)\,\tau_1^{-1} \tag{4.2}$$

while in the presence of laser radiation this becomes

$$R_1(M_1) = \{N_1(M_1) - \delta N_1(M_1)\}\,\tau_1^{-1} + B_{12}(\underset{\sim}{a},M_1)\,I_L\{N_1(M_1) - \delta N_1(M_1)\}\,\tau_1^{-1} \tag{4.3}$$

where $\delta N_1(M_1)$ is the decrease in the population of the sublevel due to laser radiation, $B_{12}(\underset{\sim}{a},M_1)$ is a coefficient describing the stimulated emission process for the sublevel and depends on the polarization state of the laser radiation designated by $\underset{\sim}{a}$, $R_1(M_1)$ is the excitation rate to the sublevel, I_L is the intensity of the laser radiation and τ_1 is the lifetime of the sublevel against radiative decay by spontaneous emission. The lifetime τ_1 is the same for all sublevels.

The two equations (4.2) and (4.3) may be solved for $\delta N_1(M_1)$, and if it is assumed that the fractional population change is small, then we have

$$\begin{aligned}\delta N_1(M_1) &\simeq B_{12}(\underset{\sim}{a},M_1)\,I_L\,N_1(M_1)\,\tau_1 \\ &\simeq B_{12}(\underset{\sim}{a},M_1)\,I_L\,R_1(M_1).\end{aligned} \tag{4.4}$$

If $R_1(M_1)$ is the same for all magnetic sublevels then we can write

$$\delta N_1(M_1) = \text{constant } B_{12}(\underset{\sim}{a},M_1). \tag{4.5}$$

We now determine the coefficient $B_{12}(\underset{\sim}{a},M_1)$ for the different sublevels. It may be shown (see for example Powell and Crasemann[2] or Maitland and Dunn[3]) that the probability of induced emission in the dipole approximation is proportional to

$$|\langle f|\ \underset{\sim}{a}.\underset{\sim}{D}\ |i\rangle|^2\ , \tag{4.6}$$

where f represents the final state, i the initial state and $\underset{\sim}{a}$ is unit vector in the direction of the electric field of the radiation.

For the geometry shown in fig. 4.3 the unit vector $\underset{\sim}{a}$ may be expanded in terms of a right handed set of orthogonal unit vectors, $\underset{\sim}{i}_1$, $\underset{\sim}{i}_2$, $\underset{\sim}{i}_3$, as

$$\underset{\sim}{a} = a_1\underset{\sim}{i}_1 + a_2\underset{\sim}{i}_2 + a_3\underset{\sim}{i}_3\ , \tag{4.7}$$

where $\underset{\sim}{i}_3$ is in the direction of the magnetic field $\underset{\sim}{B}$, and $\underset{\sim}{i}_1$ is in the plane of $\underset{\sim}{B}$ and $\underset{\sim}{k}$. For the particular geometry shown in fig. 4.1(b) it then follows that

$$a_1 = 0,\quad a_2 = \sin\phi \quad \text{and } a_3 = \cos\phi. \tag{4.8}$$

It may be shown from the properties of the matrix elements (4.6) describing transitions between different pairs of sublevels (Powell and Crasemann[2]) that

$$\begin{aligned}
&\langle\alpha',J',\ M+1|\ \underset{\sim}{a}.\underset{\sim}{D}|\alpha,J,M\rangle = \tfrac{1}{2}(a_1 - ia_2)\langle\alpha',J',M+1|D_+|\alpha,J,M\rangle\\
&\langle\alpha',J',M-1|\underset{\sim}{a}.\underset{\sim}{D}|\alpha,J,M\rangle = \tfrac{1}{2}(a_1 + ia_2)\langle\alpha',J',M-1|D_-|\alpha,J,M\rangle\\
&\langle\alpha',J',M|\underset{\sim}{a}.\underset{\sim}{D}|\alpha,J,M\rangle = a_3\ \langle\alpha',J',M|D_3|\alpha,J,M\rangle,
\end{aligned} \tag{4.9}$$

where the primed terms refer to the final state and the unprimed terms to the initial state. For the geometry of fig. 4.1(b), where $\chi = \pi/2$, and using (4.8), (4.9) reduces to

$$\begin{aligned}
|\langle\alpha',J',M+1|\underset{\sim}{a}.\underset{\sim}{D}|\alpha,J,M\rangle|^2 &= \frac{1}{4}\sin^2\phi|\langle\alpha',J',M+1|D_+|\alpha,J,M\rangle|^2\\
|\langle\alpha',J',M-1|\underset{\sim}{a}.\underset{\sim}{D}|\alpha,J,M\rangle|^2 &= \frac{1}{4}\sin^2\phi|\langle\alpha',J',M-1|D_-|\alpha,J,M\rangle|^2\\
|\langle\alpha',J',M|\underset{\sim}{a}.\underset{\sim}{D}|\alpha,J,M\rangle|^2 &= \cos^2\phi|\langle\alpha',J',M|D_3|\alpha,J,M\rangle|^2\ .
\end{aligned} \tag{4.10}$$

For both the transitions with which we are concerned here where

$(J - J') = +1$, it may be shown (Condon and Shortley[4], Powell and Crasemann[2]) that

$$|\langle M+1|D_+|M\rangle|^2 \propto (J - M - 1)(J - M)$$
$$|\langle M-1|D_-|M\rangle|^2 \propto (J + M - 1)(J + M)$$
$$|\langle M|D_3|M\rangle|^2 \propto (J^2 - M^2) , \qquad (4.11)$$

so that finally we obtain

$$B_{12}(\underset{\sim}{a},M_1) = \text{constant } \{(J_1^2 - M_1^2) \cos^2\phi + \tfrac{1}{4}(J_1 - M_1 - 1)(J_1 - M_1) \sin^2\phi + \tfrac{1}{4}(J_1 + M_1 - 1)(J_1 + M_1) \sin^2\phi\}. \qquad (4.12)$$

Relative values of the matrix elements given by (4.11) for $J = 5/2$ have been tabulated in table (4.1), and these give the following for the population changes on the different magnetic sublevels

$$\delta N_1(\pm 5/2) = C_1\ 5 \sin^2\phi$$
$$\delta N_1(\pm 3/2) = C_1\ (4 \cos^2\phi + 3 \sin^2\phi)$$
$$\delta N_1(\pm 1/2) = C_1\ (6 \cos^2\phi + 2 \sin^2\phi). \qquad (4.13)$$

Having derived expressions for the population changes of the magnetic sublevels of the upper laser level, we must now determine the effect of these on the polarization of the modulated component of the spontaneous emission sidelight (the perturbation spectrum) when observed in a general viewing direction $\underset{\sim}{V}$. For spontaneous emission from one of the upper laser sublevels (α_1, J_1, M_1) to a sublevel (α_3, J_3, M_3) of a lower level, not necessarily the lower laser level, the intensity change is given by

$$\delta I(\alpha_1, J_1, M_1, \alpha_3, J_3, M_3, \underset{\sim}{V}, \underset{\sim}{b}) = \text{const. } \delta N_1(M_1)|\langle \alpha_3,J_3,M_3|\underset{\sim}{b}.\underset{\sim}{D}|\alpha_1,J_1,M_1\rangle|^2, \qquad (4.14)$$

where $\underset{\sim}{b}$ specifies the orientation of the analyser used in the observation of the emitted radiation. The total intensity of the modulated radiation is given by summing (4.14) over the allowed transitions from the set of sublevels of the upper level to the set of sublevels of the lower level, so that we have

$$\delta I(\alpha_1, J_1, \alpha_3, J_3, \underset{\sim}{V}, \underset{\sim}{b}) = \sum_{\substack{M_1 \; M_3 \\ \text{allowed}}} \delta N_1(M_1) |\langle \alpha_3, J_3, M_3 | \underset{\sim}{b}.\underset{\sim}{D} | \alpha_1, J_1, M_1 \rangle|^2 . \tag{4.15}$$

In order to determine the matrix elements we write as before

$$\underset{\sim}{b} = b_1 \underset{\sim}{i}_1' + b_2 \underset{\sim}{i}_2' + b_3 \underset{\sim}{i}_3' , \tag{4.16}$$

where the unit vectors are defined in fig. 4.4.

In the case when the analyser is orientated to accept linearly polarized radiation with its electric vector parallel to the axis of the discharge tube ($\underset{\sim}{b}'$) then

$$b_1' = 0, \; b_2' = 1, \; b_3' = 0, \tag{4.17}$$

so that the matrix elements according to (4.9) become

$$|\langle \alpha_3, J_3, M_1 + 1 | \underset{\sim}{b}'.\underset{\sim}{D} | \alpha_1, J_1, M_1 \rangle|^2 = \tfrac{1}{4} |\langle \alpha_3, J_3, M_1 + 1 | D_+ | \alpha_1, J_1, M_1 \rangle|^2$$

$$|\langle \alpha_3, J_3, M_1 - 1 | \underset{\sim}{b}'.\underset{\sim}{D} | \alpha_1, J_1, M_1 \rangle|^2 = \tfrac{1}{4} |\langle \alpha_3, J_3, M_1 - 1 | D_- | \alpha_1, J_1, M_1 \rangle|^2$$

$$|\langle \alpha_3, J_3, M_1 | \underset{\sim}{b}'.\underset{\sim}{D} | \alpha_1, J_1, M_1 \rangle|^2 = 0 . \tag{4.18}$$

When the analyser is rotated through $\pi/2$ relative to the first position, we have

$$b_1'' = \cos\theta, \; b_2'' = 0, \; b_3'' = \sin\theta , \tag{4.19}$$

so that the matrix elements are now

$$|\langle \alpha_3, J_3, M_1 + 1 | \underset{\sim}{b}''.\underset{\sim}{D} | \alpha_1, J_1, M_1 \rangle|^2 = \tfrac{1}{4}\cos^2\theta |\langle \alpha_3, J_3, M_1 + 1 | D_+ | \alpha_1, J_1, M_1 \rangle|^2$$

$$|\langle \alpha_3, J_3, M_1 - 1 | \underset{\sim}{b}''.\underset{\sim}{D} | \alpha_1, J_1, M_1 \rangle|^2 = \tfrac{1}{4}\cos^2\theta |\langle \alpha_3, J_3, M_1 - 1 | D_- | \alpha_1, J_1, M_1 \rangle|^2$$

$$|\langle \alpha_3, J_3, M_1 | \underset{\sim}{b}''.\underset{\sim}{D} | \alpha_1, J_1, M_1 \rangle|^2 = \sin^2\theta |\langle \alpha_3, J_3, M_1 | D_3 | \alpha_1, J_1, M_1 \rangle|^2 . \tag{4.20}$$

To calculate the intensity changes observed for the two polarisation states ($\underset{\sim}{b}'$, $\underset{\sim}{b}''$) and in a general viewing direction, the values for $\delta N_1(M_1)$ given by (4.13) are substituted into (4.14) together with the matrix elements given by (4.18) and (4.20), so that we obtain

$$\delta I(\underset{\sim}{V}, \underset{\sim}{b}') = C_2(38\sin^2\phi + 24\cos^2\phi)$$

$$\delta I(\underset{\sim}{V}, \underset{\sim}{b}'') = C_2(38\sin^2\phi + 24\cos^2\phi - 14\sin^2\phi\sin^2\theta + 28\cos^2\phi\sin^2\theta) \tag{4.21}$$

If we define a polarization ratio for a specific viewing direction

$$P = \frac{|\delta I_{max}| - |\delta I_{min}|}{|\delta I_{max}| + |\delta I_{min}|} , \tag{4.22}$$

where δI_{max} is the maximum intensity of the modulated component and δI_{min} is the minimum intensity (ie when the analyser is rotated through $\pi/2$), then substituting from (4.21) gives in this case

$$P = \frac{(28\cos^2\phi - 14\sin^2\phi)\sin^2\theta}{(48\cos^2\phi + 76\sin^2\phi) + (28\cos^2\phi - 14\sin^2\phi)\sin^2\theta} \quad . \qquad (4.23)$$

For the case of zero magnetic field the principle of spectroscopic stability (Heisenberg 1926[5]) may be applied. This states that the ratio in the zero field case is the same as that in the presence of a magnetic field applied parallel to the direction of the electric vector of the perturbing radiation ($\phi = 0$). For the zero field case (4.23) therefore reduces to

$$P = \frac{28\sin^2\theta}{48 + 28\sin^2\theta} \quad . \qquad (4.24)$$

In table (4.2), polarization ratios associated with different viewing directions and for different magnetic field configurations are summarized. For the case of a uniform B_ϕ field, averages of the δI's in (4.21) were first taken before substitution in (4.22). For the case of an axial magnetic field (B parallel to k), the polarization ratio was recalculated for the new geometry using equations (4.5), (4.9), (4.11) and (4.15).

In the above we have assumed that it is possible to associate discrete magnetic sublevels with both the upper and lower levels of the transition, and on this basis have used rate equations to determine the influence of linearly polarized radiation on the populations of the different magnetic sublevels of the upper level (4.5). The assumption of discrete sublevels is valid only if the applied magnetic field splits the levels beyond the natural width due to their finite lifetimes. If the field strength is less than this, a description solely in terms of sublevel populations is no longer adequate since coherence effects between the sublevels lead to off-diagonal terms in the density matrix for the system.

For the transitions of interest here ($4p\ ^2D^o_{5/2}$ - $4s\ ^2P_{3/2}$, $4p\ ^2D^o_{5/2}$ - $4s\ ^4P_{3/2}$) the lifetimes of the levels involved differ widely (tables A.2 and A.3 : $^2D^o_{5/2}$ 9nS, $^2P_{3/2}$ 0.4nS, $^4P_{3/2}$ 27nS). As a magnetic field is applied, therefore, the upper level of the 4880Å transition splits into discrete sublevels before the lower level of this transition, while the converse is the case for the 4228Å transition. It is shown in the next section that in the present experiments it is the splitting of the upper level only that influences the polarization ratio.

For magnetic fields producing splittings small compared to the natural width of the upper level the polarization ratio is that corresponding to the zero field case, while for fields producing splittings large compared to the natural width of the upper level the polarization ratio is that given by the rate equation approach discussed above. The behaviour of the polarization ratio in the intermediate field case is discussed in the next section.

An investigation of the change of polarization ratio with magnetic field strength enables the upper level lifetime to be determined even in the presence of a short lower level lifetime which is then the determining factor for the homogeneous linewidth.

4.3 Semiclassical treatment of polarization ratios

We now present a semi-classical treatment for the interaction of monochromatic unidirectional optical radiation with a collection of atomic systems in a magnetic field. We assume initially that the atomic systems are stationary (no inhomogeneous broadening). The significance of a finite bandwidth for the optical radiation and a distribution of velocities amongst the system will be discussed later.

An atomic system in the absence of the magnetic field is considered to have two energy levels, both of which are degenerate. The energy

levels are such that their energy separation is close to the frequency of the optical radiation, and that dipole transitions can occur between them. The magnetic field is considered to split the degenerate energy levels into states designated m for the upper level and μ for the lower level. Other energy levels associated with the atomic system to which the two energy levels considered explicitly can decay are taken into account phenomenologically by the introduction of damping constant (γ_1 for the upper level, γ_2 for the lower level) after the method of Wigner and Weisskopf[6].

The Hamiltonian for a particular atomic system in the presence of the optical radiation and the magnetic field can be written

$$H = (H_o + H_M + H_D + H_{opt}) \ , \tag{4.25}$$

where H_o describes the isolated atom, H_M ($= \sigma_\alpha \underline{J}.\underline{B}$) describes the effect of the magnetic field (weak), H_D describes the phenomenological damping, and H_{opt} describes the influence of the optical radiation. In the presence of the magnetic field the eigenfunctions describing the states associated with the upper level ($\alpha = 1$) are designated $|m\rangle$ and those associated with the lower level ($\alpha = 2$) are designated $|\mu\rangle$. The wavefunction of the atomic system in the presence of the radiation and damping is then expanded in terms of these eigenfunction as

$$\psi(t) = \sum_\mu a_\mu(t).|\mu\rangle + \sum_m a_m(t).|m\rangle \ , \tag{4.26}$$

where the coefficients a_μ and a_m are functions of time. This wavefunction satisfies the time-dependent Schrödinger equation

$$i\hbar \frac{d}{dt} \psi(t) = \hat{H} \psi(t) \ . \tag{4.27}$$

If we substitute (4.26) into (4.27) and make use of the relations[3]

$$(\hat{H}_o + \hat{H}_M)|m\rangle = \hbar(\Omega_1 + m\omega_1)|m\rangle$$
$$(\hat{H}_o + \hat{H}_M)|\mu\rangle = \hbar(\Omega_2 + \mu\omega_2)|\mu\rangle$$
$$\hat{H}_D |m\rangle = -(i\hbar\gamma_1/2)|m\rangle$$
$$\hat{H}_D |\mu\rangle = -(i\hbar\gamma_2/2)|\mu\rangle$$

$$\langle \mu'/\mu \rangle = \delta_{\mu\mu'}$$

$$\langle m'/m \rangle = \delta_{mm'}$$

$$\langle \mu/m \rangle = 0 \quad ,$$

then after some re-arrangement we obtain the following sets of equations (for all m' and all μ')

$$i\hbar \dot{a}_{m'} = \hbar(\Omega_1 + m'\omega_1 - \tfrac{1}{2}i\gamma_1)a_{m'} + \sum_{\mu} a_{\mu}\langle m'|\hat{H}_{opt}|\mu\rangle \qquad (4.28)$$

$$i\hbar \dot{a}_{\mu'} = \hbar(\Omega_2 + \mu'\omega_2 - \tfrac{1}{2}i\gamma_2)a_{\mu'} + \sum_{m} a_{m}\langle \mu'|\hat{H}_{opt}|m\rangle .$$

In order to describe the time evolution of the system we construct a density matrix with the following elements

$$\rho_{m'm''} = a^*_{m''}\, a_{m'} \text{ for all } m', m''$$

$$\rho_{\mu'\mu''} = a^*_{\mu''}\, a_{\mu'} \text{ for all } \mu', \mu''$$

$$\rho_{m'\mu'} = a^*_{\mu'}\, a_{m'} \text{ for all } \mu', m'.$$

From the two sets of equations (4.28) we then obtain

$$i\hbar\dot{\rho}_{m'm''} = \hbar\{(m'-m'')\omega_1 - i\gamma_1\}\rho_{m'm''} + \sum_{\mu}\{\rho_{\mu m''}\langle m'|\hat{H}_{opt}|\mu\rangle - \rho_{m'\mu}\langle m''|\hat{H}_{opt}|\mu\rangle^*\}$$

$$i\hbar\dot{\rho}_{\mu'\mu''} = \hbar\{(\mu'-\mu'')\omega_2 - i\gamma_2\}\rho_{\mu'\mu''} + \sum_{m}\{\rho_{m\mu''}\langle \mu'|\hat{H}_{opt}|m\rangle - \rho_{\mu' m}\langle \mu''|\hat{H}_{opt}|m\rangle^*\}$$

$$i\hbar\dot{\rho}_{m'\mu'} = \hbar\{\Omega_{12} + (m'\omega_1 - \mu'\omega_2) - i(\gamma_1+\gamma_2)/2\}\rho_{m'\mu'} + \sum_{\mu}\{\rho_{\mu\mu'}\langle m'|\hat{H}_{opt}|\mu\rangle\}$$

$$- \sum_{m}\{\rho_{m'm}\langle \mu'|\hat{H}_{opt}|m\rangle^*\} \quad ,$$

where $$\Omega_{12} = (\Omega_1 - \Omega_2) \qquad (4.29)$$

The approximations that we use in obtaining solutions for the elements $\rho_{m'm''}$, $\rho_{\mu'\mu''}$ follow closely those adopted by Lamb[7] in his treatment of the optical maser. The first approximation is to assume that the optical radiation only slightly perturbs the populations of the upper states so that to zero order the probability of finding an atom in a particular upper state (m'), created at a time, t_o, at a later time, t, is given by

$$\rho^{(o)}_{m'm'} = \exp\{-\gamma_1(t - t_o)\} . \qquad (4.30)$$

Further, the excitation process is assumed to be incoherent so that

$$\rho^{(o)}_{m'm''} = 0. \qquad (4.31)$$

Substitution of (4.30) into (4.29) leads to the following expression for $\rho_{m'\mu'}$ to first order

$$i\hbar\dot{\rho}^{(1)}_{m'\mu'} = \hbar\{\Omega_{12} + (m'\omega_1 - \mu'\omega_2) - i\gamma_{12}\}\rho^{(1)}_{m'\mu'} - \hbar V_{m'\mu'}(t).\exp\{-\gamma_1(t-t_o)\}, \tag{4.32}$$

where $\gamma_{12} = \frac{1}{2}(\gamma_1 + \gamma_2)$,

and $\hbar V_{m'\mu'}(t) = \langle m'|\hat{H}_{opt}|\mu'\rangle$,

and we have neglected the contribution due to the lower states since we assume that

$$\rho^{(o)}_{\mu'\mu'} << \rho^{(o)}_{m'm'} .$$

At time t_o we further assume that $\rho^{(1)}_{m'\mu'} = 0$, that is to say the excitation process does not bring about coherence between the states associated with the upper and lower levels. The coherence between states is brought about only through interaction with the radiation. At a time $t(>t_o)$, we then have

$$\rho^{(1)}_{m'\mu'}(t,t_o) = i\int_{t_o}^{t} dt'\ V_{m'\mu'}(t')\exp\{-\gamma_1(t'-t_o)\}\ \exp\{(i\Omega_{m'\mu'}+\gamma_{12})(t'-t)\}. \tag{4.33}$$

In order to integrate (4.33), the time behaviour of $V_{m'\mu'}$ is required. We treat the atomic systems as stationary, so that they all see monochromatic radiation at one frequency (ω_o). We take the radiation field to be of the form

$$\underset{\sim}{E} = \underset{\sim o}{E}\cos\omega_o t = \underset{\sim o}{E}(e^{i\omega_o t} + e^{-i\omega_o t})/2 \quad , \tag{4.34}$$

in which case we have for a dipolar interaction

$$V_{m'\mu'}(t) = \hbar^{-1}\langle m'|H_{opt}|\mu'\rangle = \hbar^{-1}\langle m'|\underset{\sim}{D}.\underset{\sim\lambda}{e}|\mu'\rangle.|\underset{\sim o}{E}|.(e^{i\omega_o t} + e^{-i\omega_o t})/2 \ , \tag{4.35}$$

where $\underset{\sim\lambda}{e}$ is unit vector in the direction of $\underset{\sim}{E}$. On substitution of (4.35) into (4.33) and neglecting the antiresonance term we then obtain

$$\rho^{(1)}_{m'\mu'}(t,t_o) = i(2\hbar)^{-1}.|\underset{\sim o}{E}|.\langle m'|\underset{\sim}{D}.\underset{\sim\lambda}{e}|\mu'\rangle.\int_{t_o}^{t} dt'.\exp\{-\gamma_1(t'-t_o)\}.\exp\{(i\Omega_{m'\mu'} + \gamma_{12})(t'-t)\}.\exp(-i\omega_o t') \quad , \tag{4.36}$$

which on integration leads to the following

$$\rho^{(1)}_{m'\mu'}(t,t_o) = \frac{i|\underset{\sim}{E}_o|.\langle m'|\underset{\sim}{D}.\underset{\sim}{e}_\lambda|\mu'\rangle.e^{-i\omega_o t}}{2\hbar\{\gamma_{12}-\gamma_1+i(\Omega_{m'\mu'}-\omega_o)\}}.\left[\exp\{-\gamma_1(t-t_o)\}-\right.$$

$$\left.\exp\{(i\omega_o - i\Omega_{m'\mu'}-\gamma_{12})(t-t_o)\}\right] . \qquad (4.37)$$

In order to find the value of $\rho^{(1)}_{m'\mu'}$, when averaged over all the atomic systems, we assume that the rate of excitation to a state m' is independent of time, and is the same for all the upper states. Designating this excitation rate as Λ_1, then

$$\overline{\rho^{(1)}_{m'\mu'}(t)} = \int_{-\infty}^{t} dt_o.\Lambda_1.\rho_{m'\mu'}(t,t_o) \quad , \qquad (4.38)$$

which on substitution from (4.37) gives

$$\overline{\rho^{(1)}_{m'\mu'}(t)} = \frac{i\Lambda_1|\underset{\sim}{E}_o|\langle m'|\underset{\sim}{D}.\underset{\sim}{e}_\lambda|\mu'\rangle}{2\hbar\gamma_1\{\gamma_{12}^2+(\omega_o-\Omega_{m'\mu'})^2\}^{\frac{1}{2}}}.\exp(-i\omega_o t + i\theta_{m'\mu'}) \quad , \qquad (4.39)$$

where

$$\theta_{m'\mu'} = \tan^{-1}\left\{\frac{\omega_o - \Omega_{m'\mu'}}{\gamma_{12}}\right\} .$$

We now return to a consideration of a single atomic system and use the first order solution for $\rho_{m'\mu'}$ derived above to find $\rho_{m'm''}$ to second order. In this way the influence of the optical radiation both on the populations of the upper states ($\rho_{m'm'}$) and in imparting coherence between these states ($\rho_{m'm''}$) will be determined to first order. From (4.29) we have the following equation for $\rho_{m'm''}$

$$i\hbar\dot{\rho}^{(2)}_{m'm''} = \hbar\{(m'-m'')\omega_1 - i\gamma_1\}\rho^{(2)}_{m'm''} + \sum_\mu\{\rho^{(1)}_{\mu m''}\langle m'|\hat{H}_{opt}|\mu\rangle - \rho^{(1)}_{m'\mu}\langle m''|\hat{H}_{opt}|\mu\rangle^*\} ,$$

so that for an atom initially created in the state m' at t_o, we obtain on integration

$$\rho^{(2)}_{m'm''}\{t,t_o(m')\} = i\sum_\mu\left[\int_{t_o}^{t} dt' V^*_{m''\mu}(t')\rho^{(1)}_{m'\mu}\{t',t_o(m')\}.\exp\{(i\Omega_{m'm''}+\gamma_1)(t'-t)\}\right]$$

$$+ \delta_{m'm''}\exp\{-\gamma_1(t-t_o)\} . \qquad (4.40)$$

The last term in (4.40) is due to the finite value of $\rho_{m'm''}$ at t_o in the case when m' = m''.

Substitution from (4.37) into (4.40) leads to the following equation

$$\rho^{(2)}_{m'm''}\{t,t_o(m')\} = -\sum_{\mu}\frac{|\underset{\sim}{E}_o|^2\langle m'|\underset{\sim}{D}.\underset{\sim}{e}_\lambda|\mu\rangle\langle\mu|\underset{\sim}{D}.\underset{\sim}{e}_\lambda|m''\rangle}{4\hbar^2\{\gamma_{12}-\gamma_1+i(\Omega_{m'\mu}-\omega_o)\}} \cdot$$

$$\int_{t_o}^{t} dt'(e^{i\omega_o t'}+e^{-i\omega_o t'})e^{-i\omega_o t'} \cdot \exp\{(i\Omega_{m'm''}+\gamma_1)(t'-t)\} \cdot$$

$$\left[\exp\{-\gamma_1(t'-t_o)\}-\exp\{(i\omega_o-i\Omega_{m'\mu}-\gamma_{12})(t'-t_o)\}\right] +$$

$$\delta_{m'm''}\exp\{-\gamma_1(t-t_o)\} \quad . \qquad (4.41)$$

We neglect the high frequency term, since this averages out to zero within the lifetime of the atom. Integration of the above equation between the limits specified then leads to

$$\rho^{(2)}_{m'm''}\{t,t_o(m')\} = -\sum_{\mu}\frac{|\underset{\sim}{E}_o|^2\langle m'|\underset{\sim}{D}.\underset{\sim}{e}_\lambda|\mu\rangle\langle\mu|\underset{\sim}{D}.\underset{\sim}{e}_\lambda|m''\rangle}{4\hbar^2\{\gamma_{12}-\gamma_1+i(\Omega_{m'\mu}-\omega_o)\}} \cdot$$

$$\left[\frac{e^{-\gamma_1(t-t_o)}-e^{\{(i\Omega_{m'm''}+\gamma_1)(t_o-t)\}}}{i\Omega_{m'm''}}\right.$$

$$\left. + \frac{e^{\{(i\Omega_{m'm''}+\gamma_1)(t_o-t)\}}-e^{\{(i\omega_o-i\Omega_{m'\mu}-\gamma_{12})(t-t_o)\}}}{\{i(\omega_o-\Omega_{m''\mu})+\gamma_1-\gamma_{12}\}}\right]$$

$$+ \delta_{m'm''}\exp\{-\gamma_1(t-t_o)\} \quad . \qquad (4.42)$$

For an atom initially in the state m'' at time t_o, we can derive the following analogous expression

$$\rho^{(2)}_{m'm''}\{t,t_o(m'')\} = -\sum_{\mu}\frac{|\underset{\sim}{E}_o|^2\langle m'|\underset{\sim}{D}.\underset{\sim}{e}_\lambda|\mu\rangle\langle\mu|\underset{\sim}{D}.\underset{\sim}{e}_\lambda|m''\rangle}{4\hbar^2\{\gamma_{12}-\gamma_1-i(\Omega_{m''\mu}-\omega_o)\}}$$

$$\left[\frac{e^{-\gamma_1(t-t_o)}-e^{\{(i\Omega_{m'm''}+\gamma_1)(t_o-t)\}}}{i\Omega_{m'm''}}\right.$$

$$\left. + \frac{e^{\{(i\Omega_{m'm''}+\gamma_1)(t_o-t)\}}-e^{\{(i\Omega_{m''\mu}-i\omega_o-\gamma_{12})(t-t_o)\}}}{\{i(\Omega_{m'\mu}-\omega_o)+\gamma_1-\gamma_{12}\}}\right]$$

$$+ \delta_{m'm''}\exp\{-\gamma_1(t-t_o)\} \quad . \qquad (4.43)$$

In order to find the value of $\rho^{(2)}_{m'm''}$ when averaged over the collection of atoms, (4.42) and (4.43) are summed over the atoms created at the different times t_o using

$$\overline{\rho^{(2)}_{m'm''}(t)} = \Lambda_1 \int_{-\infty}^{t} \rho^{(2)}_{m'm''}\{t,t_o(m')\}dt_o + \Lambda_1 \int_{-\infty}^{t} \rho^{(2)}_{m'm''}\{t,t_o(m'')\}dt_o \ , \quad (4.44)$$

to obtain after some re-arrangement

$$\overline{\rho^{(2)}_{m'm''}(t)} = \sum_{\mu} \frac{\Lambda_1 |\underset{\sim}{E}_o|^2 \langle m'|\underset{\sim}{D}.\underset{\sim}{e}_\lambda|\mu\rangle\langle\mu|\underset{\sim}{D}.\underset{\sim}{e}_\lambda|m''\rangle}{4\hbar^2\gamma_1(i\Omega_{m'm''} + \gamma_1)}$$

$$\cdot\left[\{i(\Omega_{m''\mu} - \omega_o) - \gamma_{12}\}^{-1} + \{-i(\Omega_{m'\mu} - \omega_o) - \gamma_{12}\}^{-1}\right]$$

$$+ \Lambda_1\gamma_1^{-1}\delta_{m'm''} \ .$$

If we combine the two summations, then we have

$$\rho^{(2)}_{m'm''}(t) = - \frac{\Lambda_1 |\underset{\sim}{E}_o|^2}{4\hbar^2\gamma_1(i\Omega_{m'm''} + \gamma_1)}$$

$$\cdot \sum_{\mu} \frac{\langle m'|\underset{\sim}{D}.\underset{\sim}{e}_\lambda|\mu\rangle\langle\mu|\underset{\sim}{D}.\underset{\sim}{e}_\lambda|m''\rangle.(i\Omega_{m'm''} + 2\gamma_{12})}{\{\gamma_{12}^2 + (\Omega_{m''\mu} - \omega_o)(\Omega_{m'\mu} - \omega_o) + i\gamma_{12}\Omega_{m'm''}\}}$$

$$+ \Lambda_1\gamma_1^{-1}.\delta_{m'm''} \ . \quad (4.45)$$

For the case when $m' = m''$ we have $\Omega_{m'm''} = 0$, and the above reduces to

$$\rho^{(2)}_{m'm'}(t) = \frac{\Lambda_1}{\gamma_1} - \frac{\Lambda_1 |\underset{\sim}{E}_o|^2}{4\hbar^2\gamma_1^2} \cdot \sum_{\mu} \frac{2\gamma_{12}\langle m'|\underset{\sim}{D}.\underset{\sim}{e}_\lambda|\mu\rangle\langle m'|\underset{\sim}{D}.\underset{\sim}{e}_\lambda|\mu\rangle^*}{\{\gamma_{12}^2 + (\Omega_{m'\mu} - \omega_o)^2\}} \ . \quad (4.46)$$

This should be compared with equation (4.4) which is the analogous expression derived by a simple treatment based on rate equations.

Suppose the following conditions apply

$$\gamma_{12} >> \Omega_{m'm''} \quad ; \quad \gamma_{12} >> (\Omega_{m''\mu} - \omega_o);$$

then (4.45) reduces to

$$\overline{\rho^{(2)}_{m'm''}(t)} = \frac{\Lambda_1}{\gamma_1}\delta_{m'm''} - \frac{2\Lambda_1 |\underset{\sim}{E}_o|^2}{4\hbar^2\gamma_1(i\Omega_{m'm''} + \gamma_1)} \cdot \sum_{\mu} \frac{\langle m'|\underset{\sim}{D}.\underset{\sim}{e}_\lambda|\mu\rangle\langle\mu|\underset{\sim}{D}.\underset{\sim}{e}_\lambda|m''\rangle}{\gamma_{12}} \ . \quad (4.47)$$

The changes produced by the radiation field are therefore

$$\overline{\delta\{\rho^{(2)}_{m'm'}\}} = - \frac{2\Lambda_1 |\underset{\sim}{E}_o|^2}{4\hbar^2\gamma_1^2\gamma_{12}} \sum_{\mu} \langle m'|\underset{\sim}{D}.\underset{\sim}{e}_\lambda|\mu\rangle\langle m'|\underset{\sim}{D}.\underset{\sim}{e}_\lambda|\mu\rangle^*$$

$$\overline{\delta\{\rho^{(2)}_{m'm''}\}} = - \left[\frac{\gamma_1}{(\gamma_1 + i\Omega_{m'm''})}\right] \frac{2\Lambda_1 |\underset{\sim}{E}_o|^2}{4\hbar^2\gamma_1^2\gamma_{12}} \sum_{\mu} \langle m'|\underset{\sim}{D}.\underset{\sim}{e}_\lambda|\mu\rangle\langle\mu|\underset{\sim}{D}.\underset{\sim}{e}_\lambda|m''\rangle \ . \quad (4.48)$$

From the above it may be seen that the 'coherence' (non-diagonal) terms are comparable to the 'population' (diagonal) terms when the separations of the upper sublevels are comparable to their natural widths. The change over from the zero field case ($\Omega_{m'm''} << \gamma_1$) to that where a description in terms of populations ($\Omega_{m'm''} >> \gamma_1$) is adequate is thus determined solely by the lifetime of the upper laser level. The behaviour of the polarization ratio with increasing magnetic field provides a method of directly determining the upper level lifetime. It should be noted, however, that in the above derivation we have neglected the populations of the sublevels of the lower level compared to those of the upper level (4.8). This is valid only when the active medium is well into the gain condition; the state of affairs in the present experiment. In the more general case the polarization ratio depends also on the lifetime of the lower level and its behaviour with magnetic field is then more complex.

The intensity of the spontaneous emission radiation from a particular atom is given by

$$I_a(\underset{\sim}{e}_o) = \sum_{m',m'',\mu'} \langle\mu'|\underset{\sim}{e}_o.\underset{\sim}{D}|m'\rangle\rho_{m'm''}\langle m''|\underset{\sim}{e}_o.\underset{\sim}{D}|\mu'\rangle^* \quad , \qquad (4.49)$$

where $\underset{\sim}{e}_o$ designates the polarization component that is being observed in the sidelight radiation. Since the atoms are randomly spaced at distances greater than a wavelength, the total spontaneous intensity is given by summing over the intensity components due to the individual atoms, so that

$$I(\underset{\sim}{e}_o) = \sum_{m',m'',\mu'} \langle\mu'|\underset{\sim}{e}_o.\underset{\sim}{D}|m'\rangle\overline{\rho_{m'm''}}\langle m''|\underset{\sim}{e}_o.\underset{\sim}{D}|\mu'\rangle^* \, . \qquad (4.50)$$

Finally, we obtain for the intensity change produced by the laser radiation

$$\delta I(\underset{\sim}{e}_o) = \sum_{m',m'',\mu'} \langle\mu'|\underset{\sim}{e}_o.\underset{\sim}{D}|m'\rangle\delta\{\overline{\rho^{(2)}_{m'm''}}\}\langle m''|\underset{\sim}{e}_o.\underset{\sim}{D}|\mu'\rangle^* \qquad (4.51)$$

where $\delta\{\overline{\rho^{(2)}_{m'm''}}\}$ is given by (4.48).

So far we have restricted our treatment to stationary atoms in a monochromatic radiation field with no time fluctuations. We now consider qualitatively the effects of removing these restrictions.

To see the consequences of multimode radiation it is sufficient to consider the two mode case when the field is of the form

$$\underset{\sim}{E} = \underset{\sim}{E}_o \cos(\omega_o t + \theta_o) + \underset{\sim}{E}_o' \cos(\omega_o' t + \theta_o'). \qquad (4.52)$$

If the analysis is now carried out as before then we find in the final expression for $\overline{\rho^{(2)}_{m'm''}(t)}$ two time-independent terms of the form (4.45), one involving $|\underset{\sim}{E}_o|^2$ and ω_o and the other involving $|\underset{\sim}{E}_o'|^2$ and ω_o', together with a time-dependent term of the form $\exp\{i(\omega_o'-\omega_o)t\}$ - ie a term describing oscillations in the populations. This term averages to zero for time intervals long compared to $2\pi/(\omega_o'-\omega_o)$, under which circumstance the functional form of (4.45) remains.

For the case of laser radiation the predominant time fluctuations associated with a mode are those of phase, since gain saturation in the active medium acts to reduce amplitude fluctuations. We can investigate the effect of phase fluctuations by considering a radiation field of the form

$$\underset{\sim}{E} = \underset{\sim}{E}_o \exp\{-i\omega_o t + i\phi(t)\}, \qquad (4.53)$$

where $\phi(t)$ is a random function of time and is such that

$$\langle|\delta\phi(t'-t'')|\rangle = \langle|\phi(t') - \phi(t'')|\rangle << 2\pi \ ,$$

for

$$|(t'-t'')| << \tau_c, \qquad (4.54)$$

where τ_c is the coherence time of the radiation. In order to investigate the influence of these fluctuations on the elements $\rho_{m'm''}$, we substitute (4.53) into (4.36) and then before integration substitute (4.36) into (4.40) to obtain

$$\rho^{(2)}_{m'm''}(t,t_o) = -K\, e^{-(i\Omega_{m'm''}+\gamma_1)t} \int_{t_o}^{t} dt'' \int_{t_o}^{t''} dt'\, e^{-\gamma_1(t'-t_o)}$$
$$e^{-(i\Omega_{m'\mu'}+\gamma_{12}-i\omega_o)(t''-t')}\, e^{(i\Omega_{m'm''}+\gamma_1)t''}\, e^{i\delta\phi(t'-t'')} \qquad (4.55)$$

where K is a constant. The area in the t't'' plane over which the above integrations extend is shaded in fig. 4.5. If we define two new variables

$$\tau = (t'' - t')$$

$$\chi = (t' + t'') - (t + t_o), \qquad (4.56)$$

then we can re-write (4.55) in terms of these variables as

$$\rho^{(2)}_{m'm''}(t,t_o) = -K\, e^{-\gamma_1(t-t_o)/2}\, e^{-(i\Omega_{m'm''}+\gamma_1)(t-t_o)/2} \int_{t_o-t}^{-t_o+t} d\chi \int_{o}^{(t-t_o)-|\chi|} d\tau\, e^{(i\omega_o - i\Omega_{m'\mu'} - \gamma_{12}+\gamma_1+i\Omega_{m'm''}/2)\tau}\, e^{i\delta\phi(\tau)}\, e^{(i\Omega_{m'm''}/2)\chi}, \qquad (4.57)$$

where the limits of integration have been deduced using fig. 4.5. We now examine the integral over τ in (4.57). The time interval that makes an effective contribution to this integral is determined by the damping constant, in this case $(\gamma_{12}-\gamma_1)$, and is hence approximately $(\gamma_{12}-\gamma_1)^{-1}$. If the phase fluctuates by more than 2π over this interval, then the phase of $\rho_{m'm''}$ is randomized and hence when an average is carried out over all atoms (ie over all t_o values), $\overline{\rho_{m'm''}}$ is zero - ie the coherence between the states is destroyed. In the particular case $m' = m''$, the effect is to average out the field perturbation of the state to zero. For coherence between states to be preserved on averaging, we therefore have that

$$\tau_c > 2/(\gamma_2 - \gamma_1). \qquad (4.58)$$

In the case of the 4880Å transition in argon, $\gamma_1 \simeq 10^8\ s^{-1}$, $\gamma_2 \simeq 3 \times 10^9\ s^{-1}$ (see Appendix A), so that we require $\tau_c > 1nS$. Since the transit time of radiation in the cavity is 3nS, this condition is readily fulfilled.

Both the 4880Å and 4228Å transitions are inhomogeneously broadened through the Doppler effect. For typical operating conditions of the argon laser the inhomogeneous broadening is about 4 GHz[8]. This has

two consequences to the present case. First, the oscillating modes of the laser radiation have frequencies distributed over about 4 GHz. Second, because of their distribution of velocities the atoms in the active medium have a spread of resonance frequencies (Ω_{m_μ}). With regard to the first we have already seen that multimode oscillation does not alter the polarization ratio deduced from time averaged values of the modulated spontaneous emission. However beats up to 4 GHz will be present in the sidelight. With regard to the second, this also has no influence on the polarization ratio since all groups of atoms under the inhomogeneous profile have the same relative values of $\overline{\delta\rho_{m'm''}}$'s and so the same polarization ratio.

There is one further assumption made in the derivation of (4.48) that we must examine, namely

$$\gamma_{12} >> \Omega_{m'm''} ,$$

ie the Zeeman splitting must be much less than the homogeneous linewidth. If this condition is not fulfilled then the different $\rho_{m'm''}$ values are influenced to different extents by a mode of the radiation field (the linewidth factor in (4.45)). For the 4880Å transition $\gamma_{12} \simeq 3 \times 10^9\ s^{-1}$ (Appendix A) whereas maximum values of $\Omega_{m'm''}$ are $3 \times 10^8\ s^{-1}$. In fact in the presence of multimode oscillation across the inhomogeneous profile the above requirement is relaxed. Once the Zeeman splitting ($\Omega_{m'm''}$) has exceeded the natural width of the upper level (γ_1) coherence terms no longer appear in the polarization ratio. It is then sufficient that the total linewidth of the laser radiation exceeds the Zeeman splitting. If the magnetic field is increased to lead to splittings greater than γ_{12}, then in the present case no further change in polarization ratio is to be expected.

4.4 Experimental results

We first of all consider the measurements made in the absence of an applied magnetic field. The detection system is shown in fig. 4.6. The spontaneous emission sidelight is sampled by a fibre optic with a slit input set parallel to the axis of the laser tube and about 1 cm from the active medium in the tube, being separated from it by the quartz walls and water in the cooling jacket. The acceptance angle of such an arrangement for light coming directly from the active medium is about $\pm 5^{\circ}$ around the axis of the tube, but in the plane of the tube axis is larger being determined by the acceptance angle of the fibre optic, in this case about $\pm 10^{\circ}$. As well as this there is the possibility of light being reflected from the quartz-air interface of the outer wall of the cooling jacket into the fibre optic. Light from the fibre optic then passes into the monochromator and the remainder of the detection system is as described in ch. 2. The polarization of the radiation is investigated by inserting a polaroid sheet, which is rotated in a plane perpendicular to the fibre optic, between the quartz water jacket of the laser and the slit of the fibre optic. By observing the dc spontaneous emission from the discharge as the polaroid sheet was rotated it was confirmed that the fibre optic effectively depolarizes the radiation propagating through it - this is important since the transmission of the grating monochromator is sensitive to the polarization state of the incident radiation. An intracavity prism was used to obtain single frequency oscillation at 4880Å under all operating conditions. The orientation of the Brewster angle windows and the faces of the prism (parallel to the windows) determine the polarization of the laser radiation (see fig. 4.1).

The polarization ratio (4.22) of the modulated component of the spontaneous emission was measured for viewing directions V_1 and V_2

(fig. 4.1) on both the 4880Å ($4p\ ^2D_{5/2} - 4s\ ^2P_{3/2}$) and 4228Å ($4p\ ^2D_{5/2} - 4s\ ^4P_{3/2}$) transitions.

Under all operating conditions, the polarization ratios for direction V_2 were found to be zero as expected, and for direction V_1 to be a maximum, the electric vector of the δI_{max} component in this direction being parallel to the electric vector of the laser radiation.

No changes in the polarization ratios were observed as the fibre optic was moved to different positions along the active length of the discharge tube. The ratios also remained unaltered as the laser mirrors were misaligned to alter the mode structure and amplitude of the laser field under constant discharge conditions. All these observations are to be expected from the analysis given in the previous section.

The polarization ratio for the 4880Å transition and for viewing direction V_1 is shown in fig. 4.7 as a function of discharge current, the pressure being constant at 0.35 Torr. The errors indicated cover the non-linearity of the detection system and the setting error for rotation of the polaroid analyser. The corresponding polarization ratios for the 4228Å transition show no detectable deviation from those at 4880Å. The lower current limit is the threshold for lasing, the upper limit being determined by the power capability of the laser tube.

The maximum field intensity inside the laser cavity during the above measurements was about 5 watts cm^{-2} (at 0.3 Torr, 9 A) falling to below 1 watt cm^{-1} as the discharge conditions were altered during the experiments.

The polarization ratios for other transitions (4371Å, $4p\ ^4P_{3/2} - 3d\ ^4D_{5/2}$; 4806A, $4p\ ^4P_{5/2} - 4s\ ^4P_{5/2}$; 4610A, (^1D) $4p\ ^2F_{7/2}$- (^1D) $4s\ ^2D_{5/2}$) that appear prominently in the perturbation spectrum, but which do not

have the same upper level as the laser transition, were also investigated as a function of discharge current and pressure. Within the sensitivity of the apparatus (minimum polarization ratio about 0.01) they exhibited no polarization effects.

An axial magnetic field was applied to the active medium by winding a pair of coils on the water jacket as shown in fig. 4.9. The coils were spaced by their diameter (1 cm) to give a Helmholtz configuration, and produce a field of 34 gauss A^{-1} at the midpoint. Since it was now no longer possible to use the fibre optic to sample the spontaneous emission a 2.5 cm diameter imaging lens at a distance of 25 cm from the discharge tube was used to image that part of the active medium mid-way between the coils, on to the inlet slit of the monochromator. Such an arrangement has an acceptance angle of about $\pm 3^{o}$. The polaroid analyser was placed immediately in front of the coils as shown in fig. 4.9. Since the imaging lens does not depolarize the radiation before it enters the monochromator, unpolarized radiation exhibits an 'apparent' polarization as the polaroid analyser is rotated, due to the dependence of the monochromator transmission on polarization. This effect was allowed for by using the dc spontaneous emission (unpolarized) to calibrate the transmission of the detection system for two orientations of the polaroid analyser used in determining the polarization ratio of the modulated component. The relative transmittance of the system for these two polarization states was found to be independent of intensity, and was constant throughout the experiments. The variation of polarization ratio in viewing direction V_1 for both the 4880Å and 4228Å transitions as an axial magnetic field is applied to the active medium is shown in fig. 4.10 for a discharge current of 9 A and a filling pressure of 0.25 Torr. The polarization ratio changes significantly from the zero applied field case for fields around 30 gauss. In fig. 4.11

the variations with applied field of the individual π and $\sigma_{\pm}$ components that make up the polarization ratio are shown. Although both components increase with applied field, the π component increases more rapidly, hence producing the change in polarization ratio. It is interesting to note that as the axial field is applied the dc spontaneous emission remains unaltered although both components of the modulated spontaneous emission increase - this can only be accounted for by an increase in the efficiency of coupling between the active medium and laser radiation with increasing field.

4.5 Interpretation and conclusions

We first of all consider the dependence of polarization ratio on discharge current (fig. 4.7). Over the current range 6 to 9 A the maximum value of the B_{ϕ} magnetic field (ie at the capillary wall) changes from 12 gauss to 18 gauss. The g-factor for the 4p $^2D_{5/2}$ level is 1.24[9] and hence the splitting factor, in terms of angular frequency, for this level is 10.8×10^6 B s^{-1}. The maximum splitting of the 4p $^2D_{5/2}$ level hence varies between 1.3×10^8 s^{-1} and 1.9×10^8 s^{-1}. Since the polarization ratios for both the 4880Å and 4228Å transitions are independent of current, this suggests that γ_1 for the 4p $^2D_{5/2}$ level is greater than 1.9×10^8 s^{-1}.

It is not plausible to argue that γ_1 is less than 1.3×10^8 s^{-1} and that total splitting has already occurred by 6 A. Since the self magnetic field in the active medium varies from zero on the capillary axis to its maximum value at the tube wall, there must always be some region towards the axis of the discharge where the splitting is less than total, and so the polarization ratio must change with increasing current as this region decreases in volume. The value of 0.23 for the polarization ratio as opposed to the theoretical value of 0.37 for the zero field case can be accounted for by the large acceptance angle of

the fibre optic in the plane of the tube axis and by stray reflections from the glass-air and water-glass interfaces associated with the water cooling jacket. If γ_1 is greater than 1.9×10^8 s^{-1} as proposed then the polarization ratio would be independent of pressure as observed (fig. 4.8).

We now consider the dependence of polarization ratio on applied magnetic field (figs. 4.10 and 4.11). At axial fields above about 30 gauss, as calculated for the centre of the Helmholtz pair, the polarization ratio begins to change significantly from its zero field value (0.25), reaching a final constant value of 0.14 at high fields. This constant value must correspond to total splitting by the axial field. The value expected theoretically in this case is 0.23, and the fact that the experimental value is less may be accounted for, as before, by lack of angular resolution or by scattered light. The change in polarization ratio when the axial field is in the range 30-60 gauss indicates a γ_1 value in the range $3\text{-}6 \times 10^8$ s^{-1}, and hence a lifetime for the 4p $^2D_{5/2}$ level in the range 1.5 - 3 ns. The radiative lifetime of the 4p $^2D_{5/2}$ level as calculated and experimentally determined (see table A.2) is 9 ns. (There is some evidence - see fig. A.17 - that the lifetime of the 4p $^2D_{5/2}$ level may decrease to about half its radiative lifetime at a discharge current of 10 A in a 2 mm bore tube.) In view of the inhomogeneous nature of the applied magnetic field - the radii of the field coils are comparable to the radius of the plasma column being investigated - and the lack of a direct experimental calibration of the field strength on tube axis, this discrepancy is not unexpected. For precision lifetime measurements well-defined light collection and field coil geometries are required. Even then the inhomogeneous self-field of the discharge presents an unavoidable difficulty since

in the present case its value is sufficient to produce splittings approaching the level widths.

References (Ch. 4)

1 Van Vleck J H 1925 Proc Nat Acad Sci Wash 11 612

2 Powell J L and B Crasemann 1961 Quantum Mechanics Addison-Wesley London

3 Maitland A and M H Dunn 1969 Laser Physics North Holland Publishing Co Amsterdam

4 Condon E V and G H Shortley 1953 The Theory of Atomic Spectra Cambridge University Press London

5 Heisenberg W 1926 Z Phys 31 617

6 Weisskopf V and E Wigner 1930 Z f Phys 63 54

7 Lamb W E 1964 Phys Rev 134 A1429

8 Bloom A L, R L Byer and W E Bell 1966 The Physics of Quantum Electronics McGraw-Hill New York

9 Moore C E 1952 Natl Bur Std US circular 467 vol II

M value for $4s\ {}^2P_{3/2}$ level	M value for $4p\ {}^2D_{5/2}$ level	$+\frac{5}{2}$	$+\frac{3}{2}$	$+\frac{1}{2}$	$-\frac{1}{2}$	$-\frac{3}{2}$	$-\frac{5}{2}$
$+\frac{3}{2}$		20	4	2			
$+\frac{1}{2}$			12	6	6		
$-\frac{1}{2}$				6	6	12	
$-\frac{3}{2}$					2	4	20

Table 4.1 Values of the matrix elements defined by (4.11) for different pairs of sublevels of the transition $4s\ {}^2P_{3/2} - 4p\ {}^2D_{5/2}$

Field	Viewing direction		
	General direction in plane normal to $\underset{\sim}{k}$ at angle ψ to $\underset{\sim}{X}$	V_1	V_2
(or $\underset{\sim}{B} \overset{\text{zero}}{\|\|^e} \underset{\sim}{X}$)	$28 \sin^2\psi/(48 + 28 \sin^2\psi)$	0.37	0
$\underset{\sim}{B} \perp \underset{\sim}{X}$	$14 \cos^2\psi/(76 - 14 \cos^2\psi)$	0	0.23
Average over uniform B_ϕ field	$\dfrac{\lvert(3.5 - 5.25 \cos 2\psi)\rvert}{(65.5 - 5.25 \cos 2\psi)}$	0.12	0.03
axial ($\underset{\sim}{B} \|\|^e \underset{\sim}{k}$)	0.23	0.23	0.23

Table 4.2 Polarization ratios for 4880Å and 4228Å transitions for different viewing directions and different magnetic field conditions

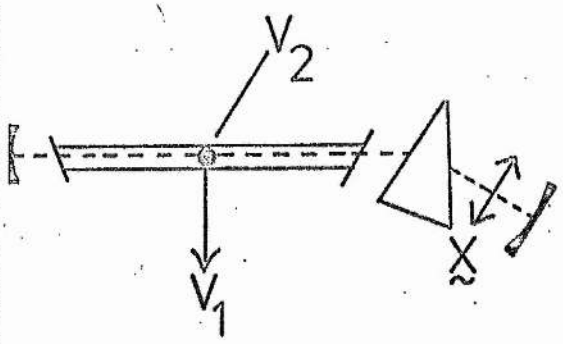

Figure 4.1(a)

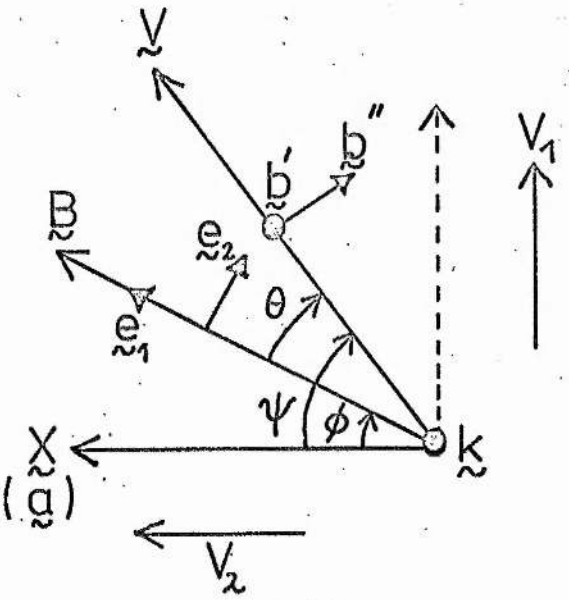

Figure 4.1 (b)

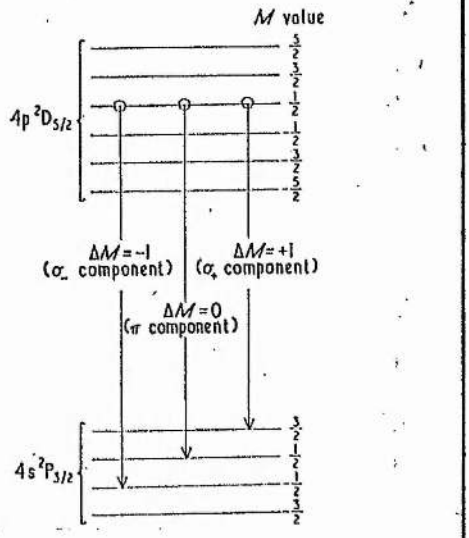

Figure 4.2 Zeeman sublevels for $4s\ ^2P_{3/2}$ and $4p\ ^2D_{5/2}$.

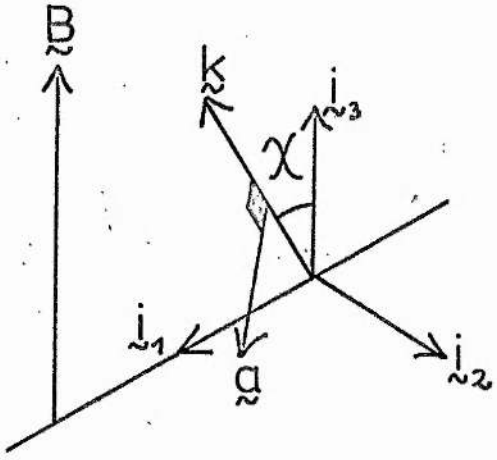

Fig. 4.3 Unit vectors - laser radiation.

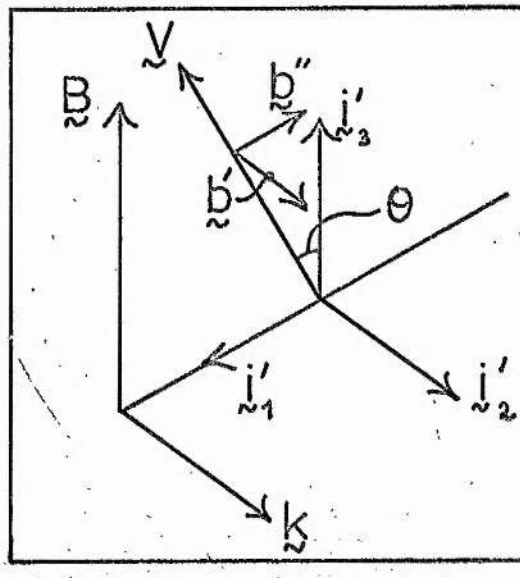

Fig. 4.4 Unit vectors - viewing direction.

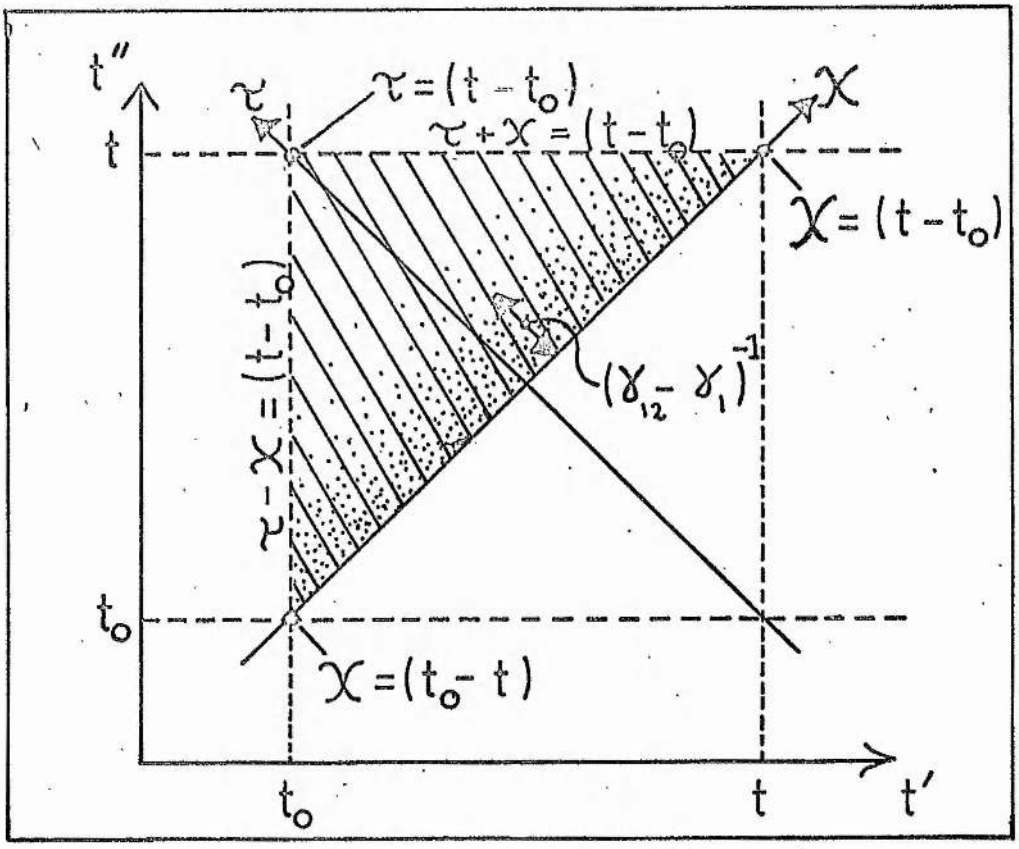

Figure 4.5 Area over which (4.55) is integrated is shown shaded. The transformed axes are τ and χ. The density of dots indicates the value of the integrand in (4.55).

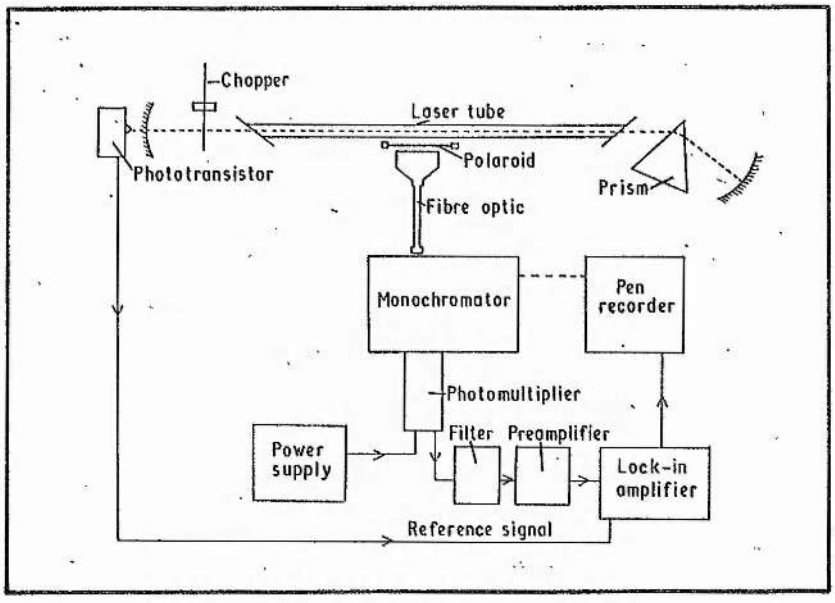

Figure 4.6 Detection system to determine the polarization ratio of the modulated component of the sidelight.

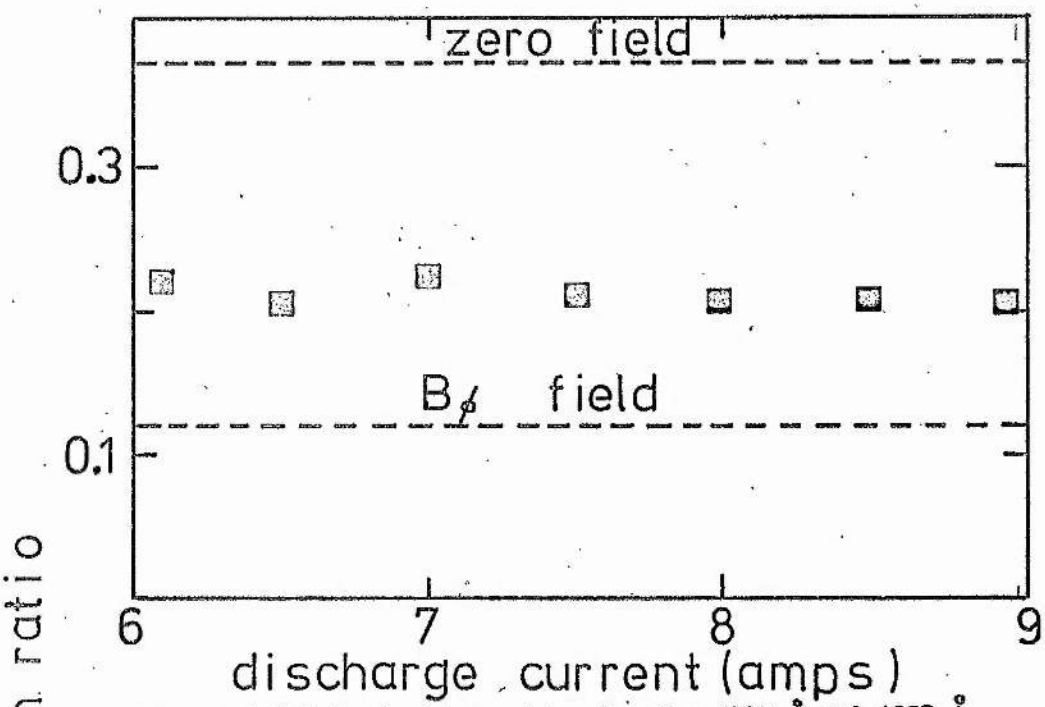

Figure 4.7 Polarization ratios for the 4880 Å and 4228 Å transitions as a function of discharge current (pressure 0.35 Torr).

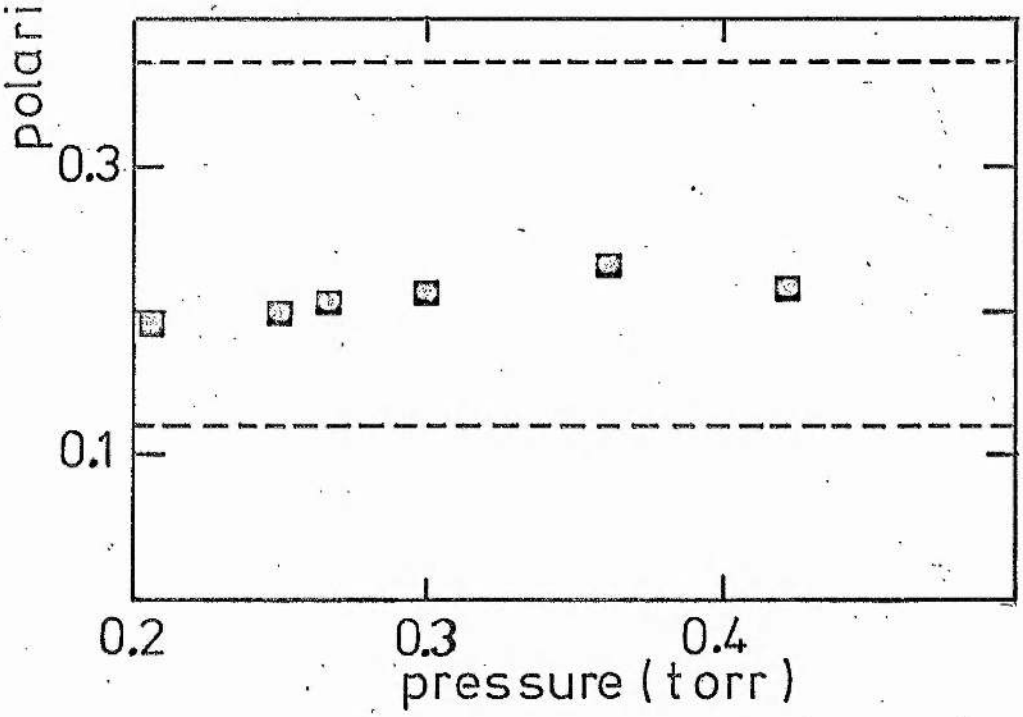

Figure 4.8 Polarization ratios for the 4880 Å and 4228 Å transitions as a function of discharge pressure (current 7 A).

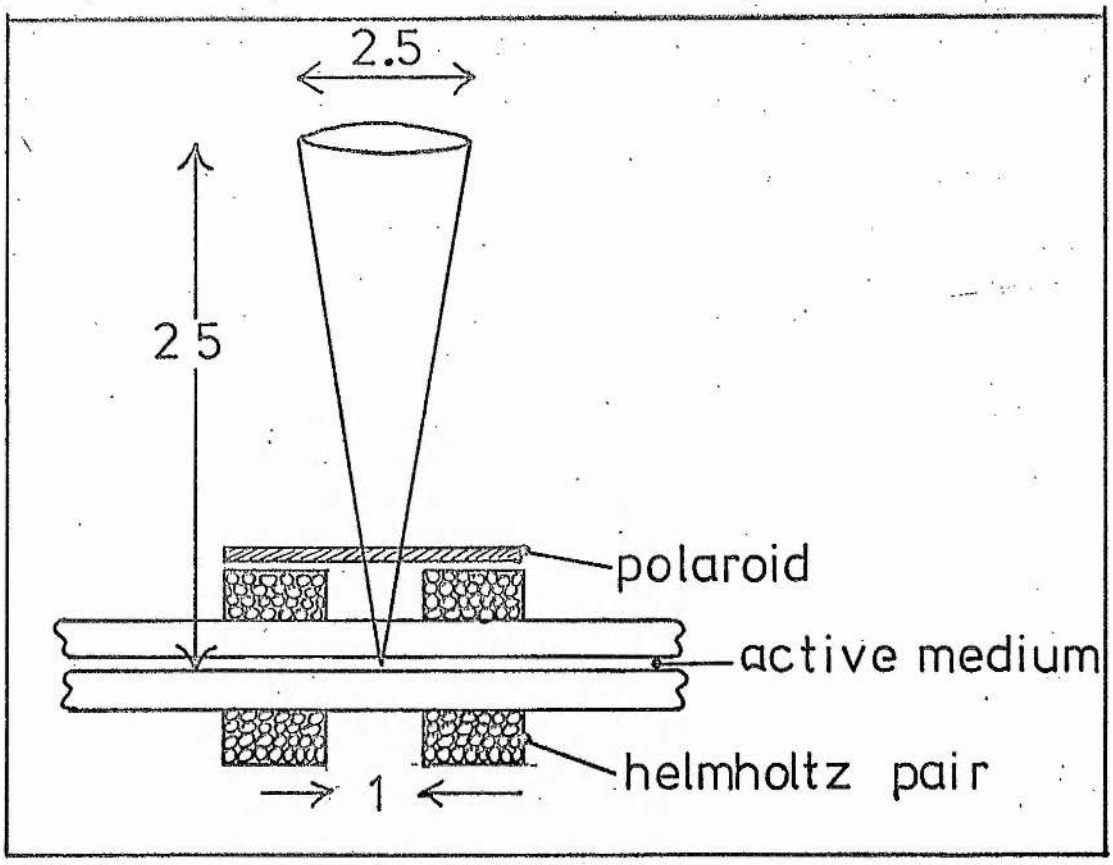

Figure 4.9 Viewing geometry for experiments involving the application of an axial magnetic field. Dimensions are in cm.

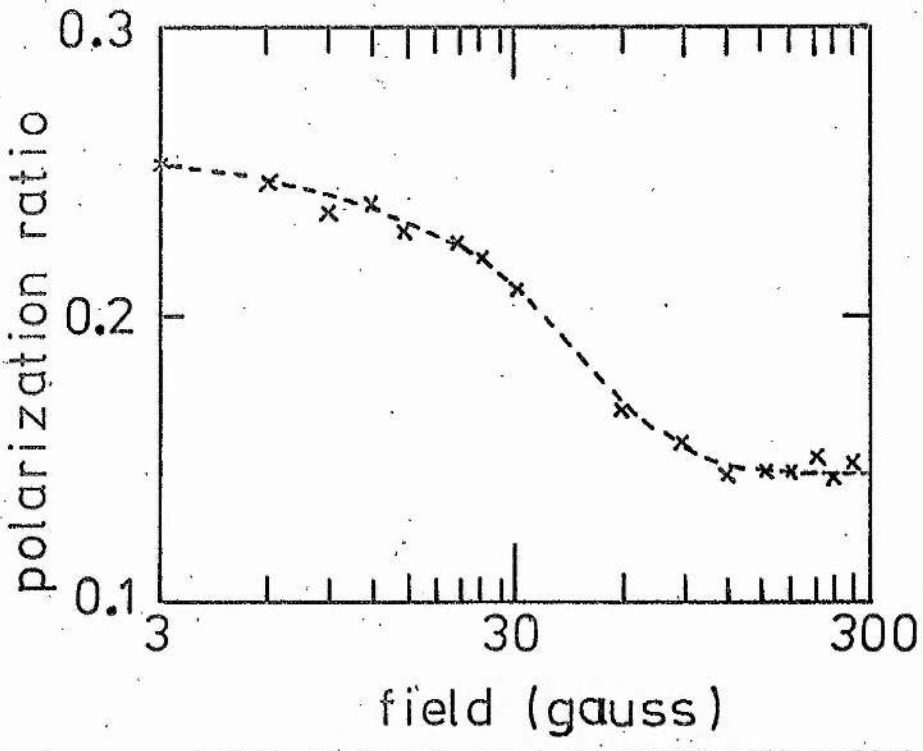

Figure 4.10 Variation of polarization ratio with applied axial field for 4880 Å and 4228 Å transitions (9 A, 0.25 Torr).

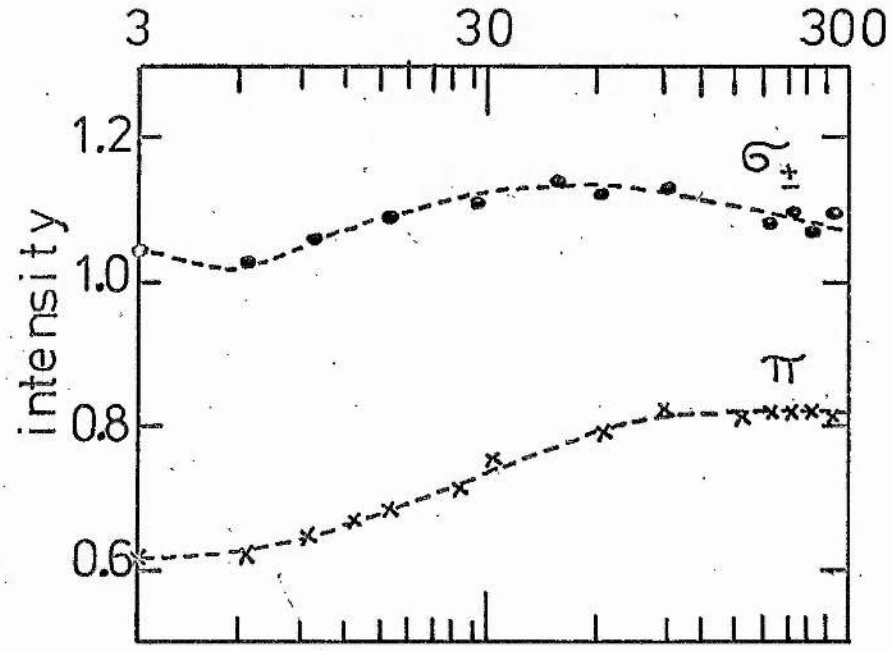

Figure 4.11 Intensity of π and $\sigma_{\pm}$ components as a function of applied axial field.

CHAPTER 5

PERTURBATIONS ON 4p and 4d TRANSITIONS

5.1 Introduction

In this chapter we consider the intensity changes that occur, due to laser oscillation, on transitions originating throughout the 4p and 4d configurations of Ar II. Since the active medium when viewed from the side is optically thin for the 4p and 4d transitions (ch.2.2) the intensity perturbations indicate population changes amongst the 4p and 4d levels, these changes being a consequence of the depletion of the populations of the upper laser levels ($4p\ ^2D_{5/2}$, $4p\ ^4D_{5/2}$) by the laser radiation.

By studying the current dependence of the 4p and 4d perturbations it is possible to assess the role of metastable ion levels in the pumping mechanism for the upper laser levels.

5.2 Experimental results

The normalized fractional perturbation for a transition has been defined in (1.7) and is

$$\sigma = (\delta I_m/I_m)/(\delta I_1/I_1), \qquad (5.1)$$

where the subscript m refers to the upper level of the transition and the subscript 1 refers to the upper laser level. Since the discharge is optically thin when viewed from the side for the transitions concerned, we can write

$$\sigma = (\delta N_m/N_m)/(\delta N_1/N_1). \qquad (5.2)$$

We first of all consider the measurements made on a 2mm bore argon laser where perturbations are produced by the self generated radiation field. In table 5.1 we show σ values for a range of 4p - 4s transitions, column A is for single frequency oscillation at 4880 Å and column B for single frequency oscillation at 5145 Å. The discharge current for these measurements was 10A and the filling pressure was 0.3 Torr. For laser oscillation at 4880 Å the σ values are in the range 2 - 4%, while for oscillation at 5145 Å, σ values for the doublet 4p levels are 3 - 5% and for the quartet 4p levels

are 8 - 11%. On table 5.2 we show σ values for 4d - 4p transitions under similar discharge conditions to those above. For the 4d levels, σ values are around 2.5 - 5% for laser oscillation at 4880 Å and 8 - 12% for laser oscillation at 5145 Å. The σ values in both tables are good to only about ± 10%, as may be seen by comparing values for two transitions originating from the same upper level, which should be the same. Although individual values are somewhat uncertain, the general trends discussed above are clear. In all cases the σ values are positive in the sense that the populations of all 4p and 4d levels decrease when the population of the upper laser level decreases. Typically, the radiation power density in the cavity during the above measurements was 70 watts cm^{-2}, and the maximum absolute population changes on the upper laser levels themselves were of the order of 7%.

There were no detectable changes in the σ values as the radiation power density in the active medium was altered under constant discharge conditions. Also, there were no significant changes with different cavity configurations. In particular, there were no differences between cavities with and without a prism, provided only one transition (4880 Å) was above threshold. These observations are important in relation to the possible effects of spontaneous emission on the perturbations. The spontaneous emission radiation from a particular transition into the cavity modes is also modulated by the chopper, and therefore could account for the small perturbation observed on that transition. We can estimate the significance of spontaneous emission as follows. The fraction of the total spontaneous emission from a transition that can radiate into the cavity modes is proportional to the solid angle of the cavity. The maximum value of this solid angle is given by

$$\frac{4\pi \ (\text{tube bore})^2}{16 \ (\text{tube length})^2} .$$

In the present case the fraction of the spontaneous emission that radiates into the cavity modes is therefore about 4×10^{-4}%. When the laser is oscillating the rate at which coherent radiation is emitted into the modes is about 7% of the total spontaneous emission from the transition, and therefore the spontaneous emission radiation density in the cavity due to a single transition is about 1 part in 10^{4} of the stimulated emission radiation density. The minimum normalized fractional perturbations (2%) are two orders of magnitude greater than this, and thus cannot be accounted for in terms of direct perturbations due to spontaneous emission radiation in the cavity. This is confirmed by the insensitivity of the perturbations to cavity configuration.

The dependence of σ on discharge current for the 5145 Å and 4380 Å transitions is shown in figs 5.1 and 5.2 respectively, the laser oscillating single frequency at 4880 Å. In order to increase the current range over which measurements could be made, the external discharge cell arrangement discussed in chs. 2 and 3 was used. This cell has a capillary bore of 4mm. Population changes on the upper laser levels were monitored using the 4228 Å and 4426 Å transitions to avoid scattered laser radiation. In figs 5.3 and 5.4 the current dependences of σ for the 3559 Å and 5145 Å transitions respectively are shown, the cell being illuminated with 4880 Å laser radiation. Figure 5.5 shows the current dependence of σ for the 3577 Å transition, when the cell is illuminated with 5145 Å radiation. For transitions originating from both 4p and 4d levels σ is independent of current, and hence we deduce that the normalized population changes on these levels are current independent.

It was not possible to investigate in detail the dependence of σ on discharge pressure since the pressure range is limited towards higher pressures by the changeover of the medium from gain to absorption (see ch. 3) and towards lower pressures by the rapidly decreasing 4p and 4d populations (see fig A.23). However, over the

limited pressure range explored (50 - 100 mTorr) it was not possible to detect significant changes in the σ values.

All the σ values given above are for the gain condition, so that the presence of laser radiation always depleted the upper laser level population with a consequent depletion of all 4p and 4d populations.

5.3 Coupling mechanisms for 4p and 4d perturbations

We now consider the coupling mechanisms that may explain the decreases in the 4p and 4d populations that accompany the direct depletion of the upper laser level populations ($4p\ ^2D_{5/2}$, $4p\ ^4D_{5/2}$) by laser oscillation.

First of all we consider coupling mechanisms involving the lower laser level ($4s\ ^2P_{3/2}$). Since $A_{12}\ \tau_1 < 1$ for both the 4880 Å and 5145 Å transitions, an increase in the $4s\ ^2P_{3/2}$ population accompanies laser oscillation (see equation (1.5)). Therefore there is an increase in any collisional pumping processes from this 4s level back to the 4p or 4d levels. Hence on this basis an increase in 4p and 4d populations is expected to accompany laser oscillation, whereas in all cases they are observed to decrease. Since the $4s\ ^2P_{3/2}$ level decays radiatively directly to the ion ground state, there is also an increase in ion ground state population accompanying laser oscillation. The same argument against this accounting for the 4p and 4d population changes applies.

We must therefore consider the population depletion on the upper laser level as the principal source of the 4p and 4d population perturbations. The following coupling mechanisms between the upper laser level and the 4p and 4d levels are now examined:

(i) Gas kinetic collisions (including charge transfer) between excited ions in the upper laser level and neutral argon atoms resulting in the transfer of the excited ions to other 4p and 4d levels. (fig. 5.6 a)

(ii) Electron-ion collisions resulting in the direct transfer of excited ions in the upper laser level to other 4p and 4d levels. (fig. 5.6 b)

(iii) Radiative decay or electron de-excitation from the upper laser level to metastable 3d levels, followed by electron impact excitation from the metastable 3d levels to the 4p and 4d levels. (fig. 5.6 c)

(iv) As in (iii) but involving quartet 4s levels as opposed to metastable 3d levels.

Mechanism (i)

The cross sections required if this mechanism is to explain the observed perturbations are now calculated from the σ values. Using equation (1.7) the rate coefficient for collisional coupling between some general 4p or 4d level m (population N_m) and the upper laser level (population N_1) is

$$\rho_{1m} = (\sigma_{1m}/\tau_m)(N_m/N_1), \qquad (5.3)$$

where σ_{1m} is the measured normalized fractional perturbation on the mth level.

We have calculated ρ_{1m} values from the σ_{1m} values using the lifetime and population data for the 4p and 4d levels summarized in tables A.2 and A.4. Values of ρ_{1m} are given in columns 5 and 6 of tables 5.1 and 5.2.

From these rate coefficients the cross-sections may be calculated using

$$\rho_{1m} \simeq V_o\, N_o\, Q_{1m}^{(n)}\ , \qquad (5.4)$$

where V_o is the neutral atom velocity, N_o the neutral atom density and $Q_{1m}^{(n)}$ the neutral atom collision cross-section for the process. Atom and ion velocities are around 10^5 cm s^{-1} in the argon discharge, as deduced from atom and ion temperature measurements (see A.3.3 and A.3.4). The neutral atom density may be deduced from the filling

pressure (0.3 Torr) using equation (A.1), and is about 2×10^{15} cm^{-3}. These values have been used to determine the cross-sections $Q_{1m}^{(n)}$ shown in columns 7 and 8 of tables 5.1 and 5.2.

Total neutral-ion collision cross-sections of the order of 2×10^{-13} cm^2 for the 4p $^2D_{5/2}$ level and 6×10^{-13} cm^2 for the 4p $^4D_{5/2}$ level are required in order to account for the observed perturbations on the 4p levels. Typically, gas kinetic cross-sections are of the order of 5×10^{-16} cm^2. However, in the present case, it is necessary to take into account the possibility of charge transfer between the excited ion and the neutral.

Dalgarno[1] has derived cross-sections for resonance charge transfer between ground state argon ions and neutral argon using the argon ion mobility measurements of Biondi and Chanin[2]. At ion velocities of 10^5 cm s^{-1} this cross-section is determined as 75×10^{-16} cm^2. Calculations based on Firsov's theory predict cross-sections of the order of 65×10^{-16} cm^2 for this energy range[3].

The collision processes under discussion involve excited argon ions, as opposed to ground state ions, and further are non-resonance in that the ion is required to be in a different 4p state after the collision. On the first of these counts there is no reason to expect a larger cross-section since the wave functions calculated by Statz et al (see A.2.2) indicate that the excited argon ion is comparable in size to the ground state ion. For non-resonance charge transfer a smaller maximum cross-section is in general expected, and this now occurs at a non-zero neutral velocity, as opposed to the resonance case where the cross-section increases monotonically on approaching zero velocity. The cross-section falls off exponentially on the low velocity side of this maximum value (the adiabatic region). The neutral velocity (V_o) corresponding to the maximum cross-section may be estimated from the energy defect, $|\Delta E|$, between initial and final states using Massey's near-adiabatic hypothesis[4]

$$a\,|\Delta E|\,/\,h\nu_o \sim 1\,, \qquad (5.6)$$

where a is a length corresponding to the range of the interaction (a value of 7×10^{-8} cm is assumed here). For transfer between adjacent 4p levels (separation approx. 0.1 eV), the near adiabatic hypothesis predicts a value of 2×10^{6} cm s^{-1} for the velocity at which the maximum cross-section occurs, so that for the neutral velocities under consideration, the non-resonance charge transfer cross-section is much below its peak value. Further, transfer to a more highly excited state is only possible at all if the energy gap involved is less than the kinetic energy of the colliding particles in their centre of mass frame (~ 0.2 eV), and so the observation of large cross-sections throughout the 4p levels is not consistent with this mechanism.

On the basis of both the calculated and measured cross-sections, neutral-ion collisions are unable to account for the magnitude of the perturbations observed throughout the 4p configuration. Also, the neutral-ion collision mechanism is unable to explain the appearance of comparable population changes on the 4d levels which are separated by optical energies (3 eV) from the levels directly perturbed by the laser radiation.

In this context, however, the report by Miller et al (A.3.9) that the population distribution throughout the 4p configuration in a high current density argon discharge has an approximately thermal form with an effective temperature corresponding to the neutral temperature, should be mentioned. It implies that neutral-ion collisions are significant in determining the populations of the 4p levels. Subsequent measurements by Rudko and Tang (A.3.9) have confirmed this finding for the 4p levels, but have further shown that other configurations (4p′, 5s, 4d, etc) also exhibit approximately thermal distributions. In general, however, the effective configurational temperature decrease rapidly in going to higher

configurations, and so the correspondence between the 4p temperature and the neutral temperature cannot, therefore, in itself be taken as implying that neutrals are the agency responsible for the population distribution amongst the 4p levels.

Mechanism (ii)

Using the ρ_{1m} values calculated according to equation (5.3), electron-ion collision cross-sections may be determined from

$$\rho_{1m} \simeq V_e \, N_e \, Q_{1m}^{(e)} \quad , \tag{5.5}$$

where N_e is the electron density, V_e the electron velocity and $Q_{1m}^{(e)}$ the inelastic electron-ion collision cross-section for electron induced transfer from the upper laser level to the general 4p or 4d level m.

Electron density and electron temperature measurements for the argon discharge (see A.3.5 and A.3.6) indicate that for the present conditions these parameters have values of 5×10^{13} cm^{-3} and 50,000 K (4.5 eV) respectively; the latter implying an electron velocity of 10^8 $cm\ s^{-1}$. On the basis of this data implied electron-ion collision cross-sections have been calculated and are tabulated in columns 9 and 10 of tables 5.1 and 5.2.

Partial cross-sections required to explain the observed population changes in terms of inelastic electron-ion collisions, range in value between 2×10^{-16} and 10^{-15} cm^2 for coupling from the 4p $^2D_{5/2}$ level, and between 2×10^{-16} and 4×10^{-15} cm^2 for coupling from the 4p $^4D_{5/2}$ level. The total cross-section for transfer from the 4p $^2D_{5/2}$ level to all other 4p levels is 6×10^{-15} cm^2, and from the 4p $^4D_{5/2}$ level is 2×10^{-14} cm^2.

The current dependence of the σ values (figs 5.1 - 5.5) is at variance with electron collisions being responsible for the 4p and 4d perturbations. All measurements of electron density in the argon discharge (and a variety of diagnostic techniques have been used) indicate that electron density increases approximately linearly with

discharge current (see A.3.5 and in particular figs A.5 - A.8). Also, electron temperature increases with discharge current (see A.3.6 and ch. 3). We have shown that the ratio (N_m/N_1) and τ_m in (5.3) are independent of current, see figs A.24 and 3.6 respectively, and therefore it follows that the normalized fractional perturbations (σ) should increase at least linearly with current if electrons are responsible for the perturbations. All experimental evidence indicates that the σ values are independent of discharge current for both the 4p and 4d configurations.

As well as the above, the magnitudes of the perturbations on the 4d levels brought about by laser oscillation at 5145 Å ($\sigma \sim 10\%$) indicate that a considerable fraction of the pumping of the 4d levels must be due to electron excitation from the 4p configuration if electron excitation is responsible for the coupling. This in turn implies that the current dependence of the 4d populations should be one power up on that for the 4p populations. Experimental measurements show that the populations of both the 4p and 4d configurations behave similarly in their current dependence over a large pressure range (fig A.24).

Electron collisions may therefore be eliminated as a possible mechanism for the 4p and 4d population changes.

Mechanisms (iii) and (iv)

Both these mechanisms are based on radiative decay from the upper laser level to a metastable ion level (quartet 4s levels or metastable 3d levels) followed by electron impact excitation from the metastable level to the 4p or 4d level. The proposed coupling scheme is illustrated in fig 5.6 (c). The metastable level, population N_i, is supposed pumped at a rate R_i through all other processes apart from that involving the upper laser level. The pumping of the metastable level by radiative decay from the upper laser level is $N_1 A_{1i}$. If τ_i is the total lifetime of the metastable level to both collisional (including collisions with the walls) and

radiative decay, then

$$N_i/\tau_i = R_i + N_1 A_{1i} . \tag{5.6}$$

The population change on the metastable level is therefore related to the population change on the upper laser level by

$$\delta N_i = A_{1i} . \tau_i . \delta N_1 . \tag{5.7}$$

If the general level (4p or 4d) is being pumped from this metastable level at a rate $N_i \rho_{im}$, then we have

$$N_m/\tau_m = R_m + \rho_{im} N_i . \tag{5.8}$$

As before we have that

$$\delta N_m = \rho_{im} \tau_m \delta N_i , \tag{5.9}$$

and so from (5.7) and (5.9) we obtain

$$\sigma = \left(\frac{N_i \rho_{im} \tau_m}{N_m}\right)\left(\frac{N_1 A_{1i} \tau_i}{N_i}\right) . \tag{5.10}$$

The first term in brackets on the right hand side of (5.10) is the fractional pumping of the general 4p or 4d level by excitation from the metastable level, while the second term is the fractional pumping of the metastable level due to spontaneous decay from the upper laser level.

All levels pumped solely by the metastable level under consideration should, therefore, exhibit the same fractional perturbation, and the fractional perturbations should be independent of current provided the excitation pathway does not change. Further, for any particular level the ratio of the fractional perturbations for lasing at 4880 Å and 5145 Å should be in the ratio of the transition probabilities from the 4p $^2D^0_{5/2}$ and 4p $^4D^0_{5/2}$ levels respectively, to the metastable level. In so far as the 4p $^2D^0_{5/2}$ and 4p $^4D^0_{5/2}$ levels are coupled radiatively to both 3d and 4s levels, the metastable levels in both these configurations must be considered as being

possible intermediates in the pumping of the 4p and 4d levels.

The ratio of the σ value for laser radiation at 5145 Å to that for laser radiation at 4880 Å, is approximately constant for all quartet 4p levels and all 4d levels, being in the range 4 - 5 (see column 11 of tables 5.1 and 5.2), while for the doublet 4p levels it is in the range 1 - 2. The ratio of the transition probability ($4p\ ^4D_{5/2}$ - quartet 4s's) to the transition probability ($4p\ ^2D_{5/2}$ - quartet 4s's) is 7 while the corresponding ratio for all the 3d states is 4 (see table A.2). On the basis of the above ratios, therefore, either the quartet 4s levels or metastable 3d levels are intermediate levels in the pumping of the quartet 4p states and the 4d states.

The relative importance of these two pathways may be assessed by examining the magnitudes of the pumping rates involved. Rudko and Tang have shown that for the present discharge conditions, the total pumping rate to all levels in the 4p, 4d and 5s configurations is about 8.5×10^{18} cm^{-3} s^{-1} (see final column of table A.2). Further, their results indicate that the pumping rate from the $4p\ ^4D_{5/2}$ level to the $4s\ ^4P_{3/2,\ 5/2}$ levels through radiative decay is 6.0×10^{17} cc^{-1} s^{-1}, so that if these levels are solely responsible for the pumping of the 4p, 4d and 5s configurations, then (5.10) shows that perturbations of the order of 7% are to be expected on all levels of these configurations due to lasing at 5145 Å. (In fact this is a conservative estimate since other 4p levels, also radiatively coupled to the $4p\ ^4P_{3/2,\ 5/2}$ levels are, of course, undergoing population changes). In a similar manner it can be shown that for lasing at 4880 Å, perturbations of the order of 1% are to be expected as a consequence of the radiative coupling (7.7×10^{16} cm^{-1} s^{-1}) of the $4p\ ^2D_{5/2}$ level to the $4p\ ^4P_{5/2,\ 3/2,\ 1/2}$ levels, and for the same reason as before this is a conservative estimate. The observation of somewhat larger perturbations, of the order of 10% for 5145 Å radiation and 2 - 3% for 4880 Å radiation, could be accounted for by collisional, as well as radiative, decay for which we have already discussed the evidence (see chs. 3 and 4 and also fig A.17).

With regard to coupling from the 4p $^2D_{5/2}$ and 4p $^4D_{5/2}$ levels to 3d levels, both the radiative coupling rates and collisional de-excitation rates are too small, by a factor of 4 (see table A.2), to explain the observed perturbations.

If the 4s $^4P_{5/2, 3/2, 1/2}$ levels are solely responsible for the pumping of the 4p levels, the cross-section estimates of Beigman et al (see fig A.32) for 4s - 4p electron excitation, imply a combined population for these quartet 4s levels of the order of 2×10^{11} cm^{-3} and a lifetime towards collisional excitation to 4p levels of 2×10^{-8} s, which is of the same order as their radiative lifetimes.

The total radiative decay from all 4p levels to the quartet 4s levels is about 4×10^{18} cm^{-1} s^{-1} (table A.2), which is about 50% of the total pumping rate to the 4p levels. This implies that if these 4s levels are responsible for the pumping of the 4p levels, a considerable fraction of the 4p population is due to re-cycling from closely lying energy levels (as opposed to the ion ground state).

5.4 Conclusions regarding the excitation mechanisms for the 4p and 4d configurations

On the basis of the available cross-section data, the observed 4p and 4d perturbations cannot be explained by inelastic neutral-ion collisions. Since the normalized fractional perturbations (σ values) are independent of discharge current, they cannot be explained by inelastic electron-ion collisions.

The σ values for the 4d and the quartet 4p levels are between 2 and 4% due to a direct population change on the 4p $^2D_{5/2}$ level and 8 - 11% due to a direct population change on the 4p $^4D_{5/2}$ level. The ratio of the σ values is approximately the same for all levels. These observations are direct evidence that an important excitation pathway for the 4d and the quartet 4p levels is through the quartet 4s levels. The magnitudes of the perturbations are consistent with reported pumping rates for the 4p configuration. The ratio of the σ values for a particular level (4 - 5 for the 4d's and quartet 4p's

and 1 - 2 for the doublet 4p's) is less than expected from the ratio of radiative decay rates to the quartet 4p states (7). This indicates that pumping is not solely through the quartet 4s states but involves other pathways, and that the relative contributions of the pathways differ between doublet and quartet 4p's.

5.5 Mode interactions

We now consider the relevance of the present study of 4p population perturbations to reported mode interactions between the 4880 Å and 5145 Å laser transitions (Forsyth[5], Statz et al[6]).

When the 4880 Å transition oscillates multimode its associated population inversion is modulated at the difference frequencies of the modes[7], and in particular the lower level population ($4s\ ^2P_{3/2}$) is modulated in this way. The lower level is common to the 5145 Å transition and therefore the population inversion at 5145 Å is also modulated at frequencies corresponding to the mode spacings at 4880 Å. If the 5145 Å transition oscillates simultaneously on a single longitudinal mode, the polarization induced by this mode in the active medium has sidebands at frequencies corresponding to the mode spacings at 4880 Å. When the longitudinal mode spacings at 4880 Å and 5145 Å are the same (equal cavity lengths) the polarization sidebands inject power into other longitudinal modes at 5145 Å, so lowering their threshold. When the longitudinal mode spacings are different (unequal cavity lengths) the frequency of the polarization sidebands does not correspond to the available modes at 5145 Å and so single mode oscillation persists. The additional modes in the output lead to an overall increase in the total power available from the transition.

We have seen in the previous sections that in the argon discharge there is coupling between the populations of upper laser levels. This coupling is important in considering mode competition effects, since the modulation of the population inversion at 4880 Å is transmitted to the population inversion at 5145 Å not only through

the common lower level, but also through the coupling between the upper laser levels ($4p\ ^2D_{5/2}$, $4p\ ^4D_{5/2}$) of these two transitions.

We now calculate the amplitude of the polarization sidebands at 5145 Å due to the observed coupling between the $4p\ ^2D_{5/2}$ and $4p\ ^4D_{5/2}$ upper laser levels.

The amplitude of the polarization sidebands at 5145 Å, under the approximations made by Statz et al[6], is given by

$$\frac{1}{2h\gamma_2} \; |D_{12}|^2 \; |\delta(N_1 - N_2)| \; |E_0| \; , \tag{5.11}$$

where $\delta(N_1 - N_2)$ is the amplitude of the modulation of the population inversion at 5145 Å due to two mode oscillation at 4880 Å, $|E_0|$ is the amplitude of the single mode (initially) at 5145 Å, $|D_{12}|$ is the x-component of the dipole matrix element for the 5145 Å transition and γ_2 is the relaxation rate of the common lower level.

If the output power of the laser at 4880 Å is P and the discharge volume coupled to the radiation field is V, then the modulation of the population inversion at 5145 Å due to the common lower level is given approximately by (see 1.5)

$$\delta N_2 = P(h\nu V\gamma_2)^{-1}(1 - A_{32}\tau_3) \; , \tag{5.12}$$

where the subscript 3 designates the $4p\ ^2D_{5/2}$ level. In order to determine the modulation of the population inversion at 5145 Å due to the coupling between the upper 4p levels, we must consider the time-dependent form of equations (5.6) and (5.8) which are

$$\begin{aligned} \dot{\delta N_i} &= A_{1i}\, \delta N_3 \cos \omega_0 t - \delta N_i\, \tau_i^{-1} \\ \dot{\delta N_1} &= \rho_{i1}\, \delta N_i - \delta N_1\, \tau_1^{-1} \; . \end{aligned} \tag{5.13}$$

From these we obtain for the amplitude of the coupling at frequency ω_0

$$(\delta N_1/\delta N_3)_{\omega_0} = (\delta N_1/\delta N_3)_{DC} (1+\omega_0^2\tau_m^2)^{-\frac{1}{2}}(1+\omega_0^2\tau_1^2)^{-\frac{1}{2}}$$

$$\simeq \sigma (1+\omega_0^2\tau_m^2)^{-\frac{1}{2}}(1+\omega_0^2\tau_1^2)^{-\frac{1}{2}} . \qquad (5.14)$$

Now we have that

$$\delta N_3 = P/(h\nu V\gamma_3) ,$$

so that the modulation of the population inversion at 5145 Å due to upper level effects is

$$\delta N_1 = \sigma P(h\nu\ V\gamma_3)^{-1} (1+\omega_0^2\tau_m^2)^{-\frac{1}{2}}(1+\omega_0^2\tau_1^2)^{-\frac{1}{2}} , \qquad (5.15)$$

and the ratio of upper to lower level modulation effects is therefore

$$\sigma(\gamma_2/\gamma_3)\ (1-A_{32}\tau_3)^{-1}(1+\omega_0^2\tau_m^2)^{-\frac{1}{2}}(1+\omega_0^2\tau_1^2)^{-\frac{1}{2}} . \qquad (5.16)$$

Assuming that $\tau_1 = 9 \times 10^{-9}$ s, $\gamma_2\gamma_3^{-1} = 25$, $\omega_0 = 2\pi \times 100$ MHz, $\tau_m = 3 \times 10^{-7}$ s, $\sigma = 0.03$ and $(1-A_{32}\tau_3) = 0.25$ (see tables A.2 - A.4), the above ratio is 0.2. Thus at heat frequencies around 100 MHz, lower level coupling is the more significant. For P = 2 watts and V = 1.5 cm^3, values of the equivalent electric field and for spontaneous emission noise were calculated by Statz et al[6] from (5.11) as 3.5×10^{-9} esu and 3.6×10^{-12} esu respectively. It therefore follows that for laser transitions that do not share a common lower laser level, upper level couplings will be significant since associated equivalent electric fields exceed spontaneous emission noise. Also, in going to heat frequencies around $\omega_0 = 2\pi \times 10$ MHz, upper level couplings dominate over lower level couplings.

References (ch. 5)

[1]Dalgarno A 1958 Phil Trans A250 426

[2]Biondi M A and Chanin L M 1954 Phys Rev 94 910

[3]Atomic and Molecular Process 1962 Ed D R Bates Academic Press p708
Firsov O B 1951 J exp theor phys 21 1001

[4]Massey H S W 1949 Rep Progr Phys 12 248

[5]Forsyth J M 1967 Appl Phys Lett 11 391

[6]Statz H, Mars G E de and Tang C L 1969 Appl Phys Lett 15 428

[7]Lamb W E Jr 1964 Phys Rev 134 A1429

Table 5.1

Level Designation Upper	Level Designation Lower	Wavelength (Å)	A (%)	B (%)	$\rho_{1m} \times 10^{-6} s^{-1}$ $(4p^2D_{5/2})$	$\rho_{1m} \times 10^{-6} s^{-1}$ $(4p^4D_{5/2})$	$Q_{1m}^{(n)} \times 10^{+14}$ $cm^2(4p^2D_{5/2})$	$Q_{1m}^{(n)} \times 10^{14}$ $cm^2(4p^4D_{5/2})$	$Q_{1m}^{(e)} \times 10^{+16}$ $cm^2(4p^2D_{5/2})$	$Q_{1m}^{(e)} \times 10^{+16}$ $cm^2(4p^4D_{5/2})$	B/A
$4p^2P^o_{3/2}$	$4s^2P_{1/2}$	4765	1.8	3.6	1.2	2.3	0.6	1.2	2.4	4.6	2
$4p^2P^o_{3/2}$	$4s^2P_{3/2}$	4545	1.8	3.7							2
$4p^2P^o_{1/2}$	$4s^2P_{3/2}$	4658	2.2	3.5	0.8	1.1	0.4	0.6	1.6	2.2	1.6
$4p^2P^o_{1/2}$	$4s^2P_{1/2}$	4889	2.6	3.5							1.4
$4p^2D^o_{3/2}$	$4s^2P_{3/2}$	4727	3.8	5.4	1.5	1.9	0.8	0.9	3.0	3.8	1.4
$4p^2D^o_{3/2}$	$4s^2P_{1/2}$	4965	3.7	4.4							1.2
$4p^2D^o_{5/2}$	$4s^2P_{3/2}$	4880	100	9.6	-	10.7	-	5.4	-	21.4	-
$4p^2D^o_{5/2}$	$4s^4P_{3/2}$	4228	100	9.8							-
$4p^4D^o_{1/2}$	$4s^4P_{1/2}$	4380	1.5	6.3	0.9	3.5	0.4	1.8	1.8	7.0	4.2

$4p^4D^o_{3/2} - 4s^4P_{3/2}$	4331	2.6	11.0	2.7	11.2	1.4	5.6	5.4	22.4	4.2
$4p^4D^o_{3/2} - 4s^4P_{1/2}$	4430	2.2	9.8							4.5
$4p^4D^o_{5/2} - 4s^2P_{3/2}$	5145	3.0	100	5.0	-	3.0	-	10.0	-	-
$4p^4D^o_{7/2} - 4s^4P_{5/2}$	4348	2.1	8.3	5.1	19.3	2.6	9.6	10.2	38.6	4.0
$4p^4P^o_{1/2} - 4s^4P_{3/2}$	4848	2.3	9.1	1.7	6.4	0.9	3.2	3.4	12.8	4.0
$4p^4P^o_{3/2} - 4s^4P_{5/2}$	4736	2.0	8.5	3.9	15.0	1.9	7.5	7.8	30.0	4.3
$4p^4P^o_{3/2} - 4s^4P_{1/2}$	5062	1.9	7.5							3.9
$4p^4P^o_{5/2} - 4s^4P_{5/2}$	4806	2.1	10.8	6.0	31	3.0	15.5	12.0	62.0	5.1
$4p^4P^o_{5/2} - 4s^4P_{3/2}$	5009	2.0	11.0							5.5

Table 5.1 Normalized fractional perturbations for 4p - 4s transitions in Ar II (2mm bore, 10 A, 0.3 Torr)

A Single frequency oscillation at 4880 Å

B Single frequency oscillation at 5145 Å

Table 5.2

Level Designation Upper	Lower	Wavelength (Å)	A (%)	B (%)	$\rho_{1m} \times 10^{-6} s^{-1}$ $(4p^2D_{5/2})$	$\rho_{1m} \times 10^{-6} s^{-1}$ $(4p^4D_{5/2})$	$Q_{1m}^{(n)} \times 10^{+14}$ $cm^2(4p^2D_{5/2})$	$Q_{1m}^{(n)} \times 10^{+14}$ $cm^2(4p^4D_{5/2})$	$Q_{1m}^{(e)} \times 10^{+16}$ $cm^2(4p^2D_{5/2})$	$Q_{1m}^{(e)} \times 10^{+16}$ $cm^2(4p^4D_{5/2})$	B/A
$4d^4P_{5/2}$	$4p^4S^o_{3/2}$	3869	2.7	10	0.5	1.6	0.2	0.8	0.9	3.2	3.8
$4d^4D_{7/2}$	$4p^4D^o_{7/2}$	3781	2.3	10	1.0	4.0	0.5	2.0	1.9	8.0	4.3
$4d^4F_{9/2}$	$4p^4D^o_{7/2}$	3588	2.5	9	0.9	3.0	0.4	1.5	1.8	6.0	3.9
$4d^4F_{7/2}$	$4p^4D^o_{5/2}$	3577	4.9	12	1.7	4.0	0.9	2.3	3.4	9.0	2.4
$4d^2F_{7/2}$	$4p^2D^o_{5/2}$	3559	5.5	8	1.0	1.4	0.4	0.7	1.6	2.8	1.4
$4d^4D_{5/2}$	$4p^4P^o_{3/2}$	3514	2.7	11	0.8	2.8	0.4	1.4	1.5	5.6	4.4
$4d^4D_{5/2}$	$4p^4P^o_{5/2}$	3477	2.6	10							3.8

Table 5.2 Normalized fractional perturbations for 4d - 4p transitions in Ar II (2mm bore, 10 A, 0.3 Torr)

A Single frequency oscillation at 4880 Å

B Single frequency oscillation at 5145 Å

Figure 5.1 Normalized fractional perturbation at 5145 Å ($4p\ ^4D_{5/2} - 4s\ ^2P_{3/2}$) due to laser oscillation at 4880 Å as a function of discharge current . Pressure 0.2 Torr, 2 mm bore tube, sidelight from laser discharge.

Figure 5.2 Normalized fractional perturbation at 4380 Å ($4p\ ^4D_{1/2} - 4s\ ^4P_{1/2}$) due to lasing at 4880 Å as a function of discharge current. Pressure 0.2 Torr, 2 mm bore tube, sidelight from laser discharge.

Figure 5.3 Normalized fractional perturbation at 3559 Å ($4d\ ^2F_{7/2} - 4p\ ^2D_{5/2}$) due to laser radiation at 4880 Å as a function of discharge current. Pressure 0.15 Torr, 4 mm bore tube, external cell.

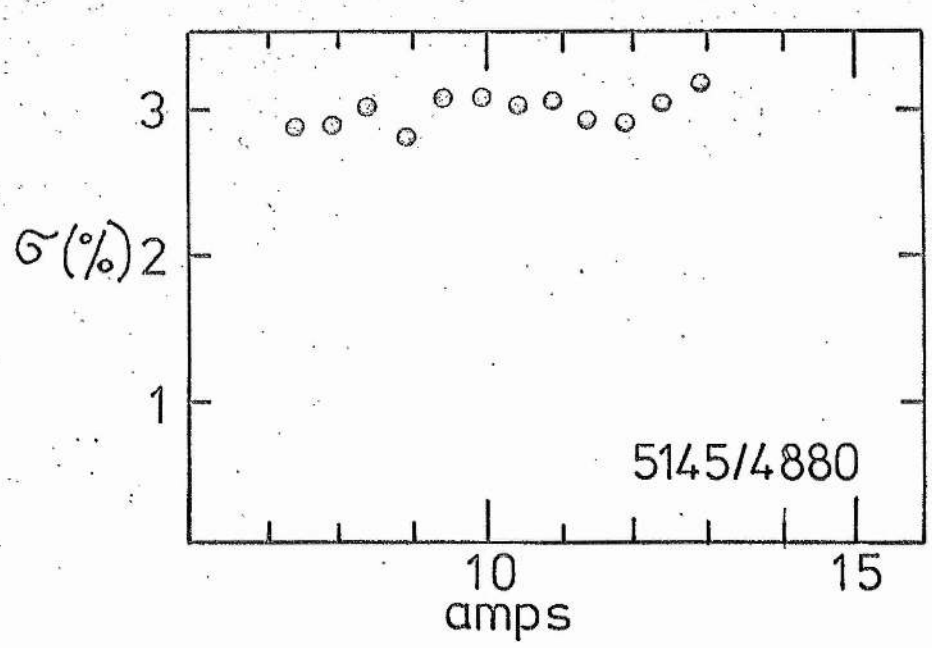

Figure 5.1

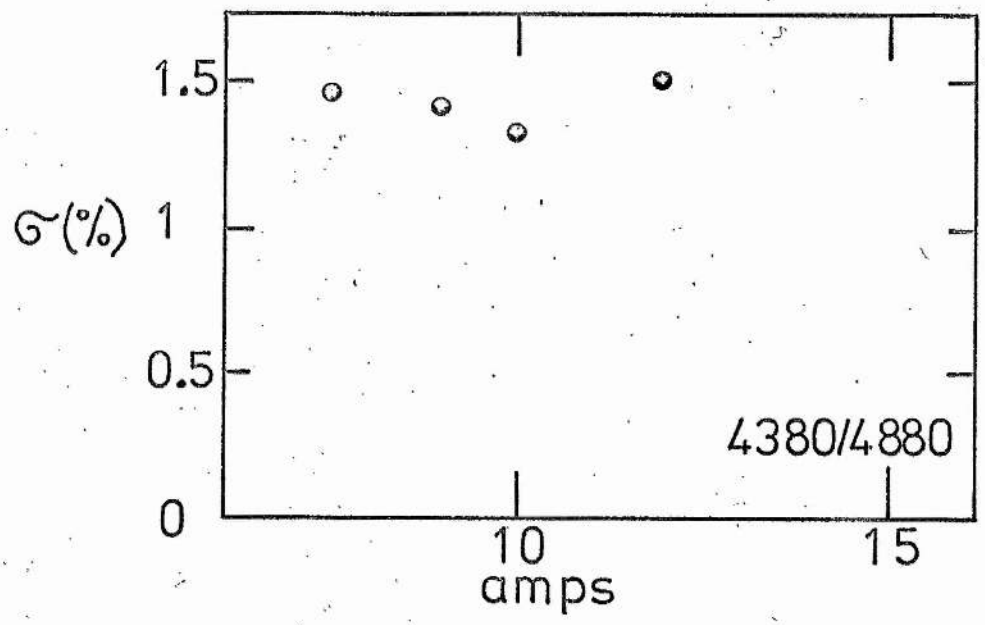

Figure 5.2

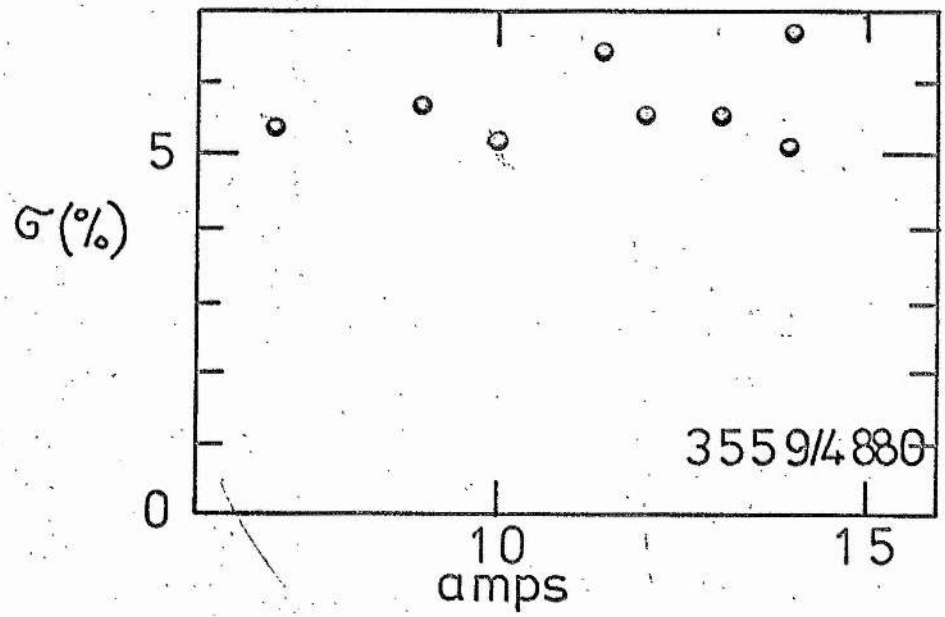

Figure 5.3

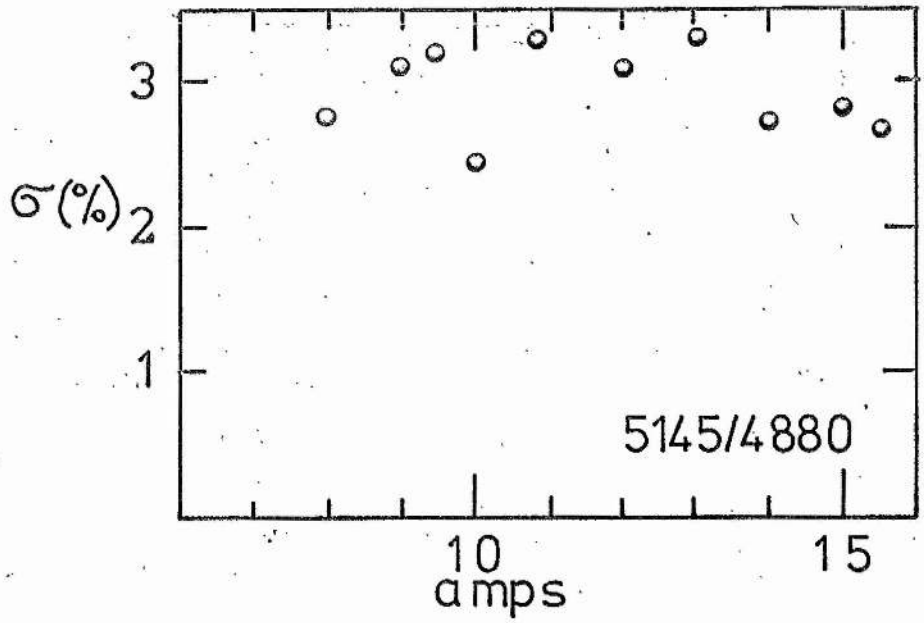

Figure 5.4

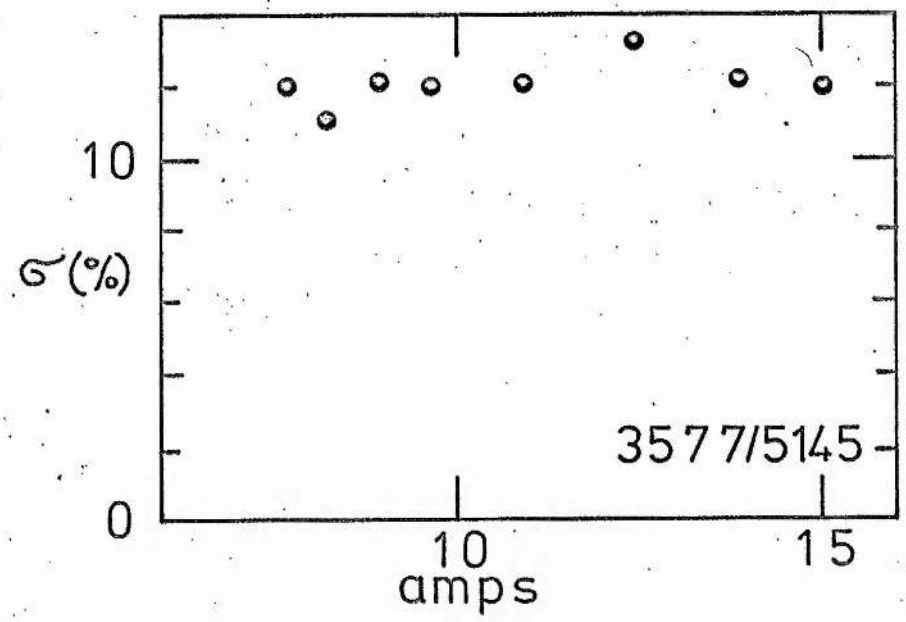

Figure 5.5

Figure 5.4 Normalized fractional perturbation at 5145 Å ($4p\ ^4D_{5/2} - 4s\ ^2P_{3/2}$) due to laser radiation at 4880 Å as a function of discharge current. Pressure 90 mTorr, 4 mm bore, external cell.

Figure 5.5 Normalized fractional perturbation at 3577 Å ($4d\ ^4F_{7/2} - 4p\ ^4D_{5/2}$) due to laser radiation at 5145 Å as a function of discharge current. Pressure 150 mTorr, 4 mm bore, external cell.

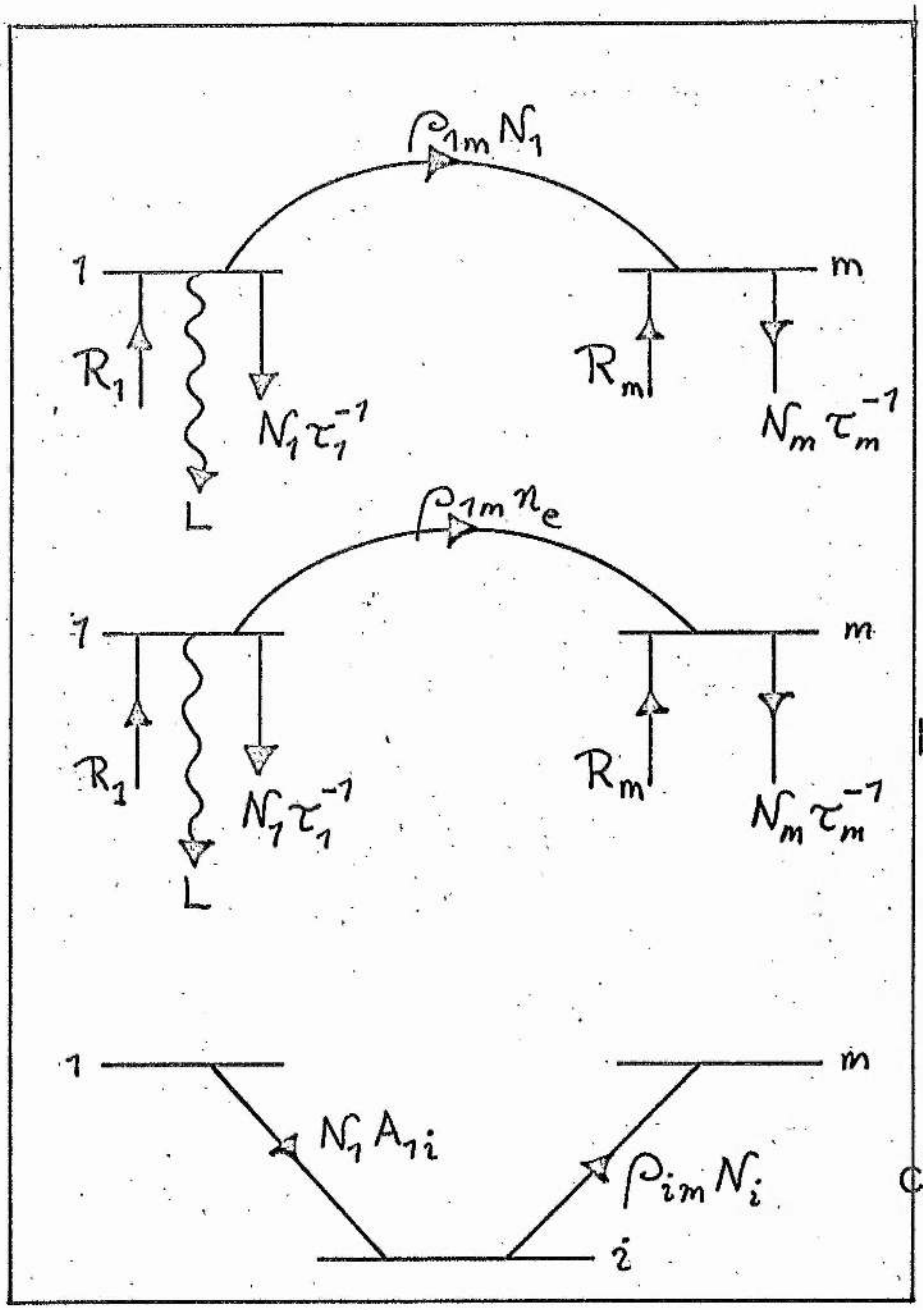

Figure 5.6 Coupling mechanisms between upper laser level and general 4p or 4d level.

APPENDIX A

REVIEW OF THE ARGON ION LASER

A.1 Historical Introduction

Ion lasers are important as practical sources of ultra violet, visible and near infra-red coherent radiation. In all ion lasers the active medium is an electrically excited gas (or vapour), but they may be classified into four principal categories depending on their mode of excitation and the nature of the active ion. Excitation of the active medium may be by current pulses leading to a pulsed coherent output, or by a dc current leading to continuous wave (cw) coherent output. The active ion may be that of a noble gas (Ar, Ne, Xe, Kr) or that of a metal vapour (Hg, Zn, Cd, Se, Mg etc.) which is usually introduced into a noble gas discharge. This review is restricted to one of the cw noble gas lasers, namely the cw argon ion laser.

The argon ion laser provides the highest cw coherent power (up to 100 watts) at present available directly from an active medium in the blue-green region of the spectrum. In the eight years since the discovery of pulsed laser oscillation in the argon ion by Bridges (1964)[1] and Convert et al (1964)[2] the argon ion laser has been developed to the stage of a commercial instrument, and its present day applications cover the fields of holography, non-linear optics, light scattering, image and data recording, doppler velocity measurement, biological research, etc.

The development of the cw argon ion laser can be conveniently considered from three viewpoints; namely, the discovery of new transitions and modes of excitation of the active medium, improvements in discharge tube technology, and finally the increasing understanding of the processes leading to population inversions. It is this latter aspect that is the most relevant here, but before going on to consider it in detail, brief consideration will be given to the first two.

In the spring of 1964, Bridges[1] and Convert et al[2] reported pulsed laser oscillation on ten transitions of the argon ion in the range

4500 - 5300Å; all but one of these transitions being from the (^{3}P) 4p to the (^{3}P) 4s configuration. This was soon followed by reports from Bennett (1964)[3] and Gordon et al (1964)[4] of quasi-continuous and true continuous laser oscillation on these transitions. Gordon et al[4] also reported cw oscillation on twenty visible transitions of krypton and xenon.

The active medium of the argon ion laser is the positive column region of a low pressure (0.2 - 0.7 Torr) dc discharge in argon. In the first generation of argon lasers, the positive column was constricted by a quartz capillary tube (bore 1.25 - 4 mm) to produce the high current densities (100Acm^{-2}) necessary to create population inversions. The capillary was usually between 25 cm and 1 m long.

Since high currents have to be passed into the gas, hot oxide-coated cathodes were employed to keep discharge voltages and cathode sputtering to a minimum. Voltage gradients in the positive column are around 10 volts cm^{-1} and so the power dissipation in the capillary even at an operating current as low as 1 A is around 10 watts cm^{-1}. A power dissipation of 25 watts cm^{-1} is sufficient to heat the quartz discharge tube to incandescence within a few seconds, so that for prolonged running at high currents, water cooling of the constricted region of the discharge is essential.

The optical cavity is in general formed from dielectric mirrors with reflectivities peaked in the range 4500Å to 5500Å. Usually one mirror has a transmission between 3% and 6% (through which the coherent power is coupled), the other being almost totally reflecting. The mirrors are usually external with tube ends terminated by Brewster angled windows.

The optimum argon filling pressure is about 0.5 Torr (for a 2 mm bore tube) and varies only slightly between the different transitions.

The E/p ratio for the positive column is therefore around 20 volts cm^{-1} $Torr^{-1}$.

For discharge tubes of the dimensions given above total power outputs on all transitions of the order of 150 mW were reported (Gordon et al[4]) from a 20 cm long tube at currents of the order of 10 A (300 A cm^{-2}). The transition exhibiting the highest gain is at 4880Å ($4p\ ^2D^o_{5/2}$ - $4s\ ^2P_{3/2}$) with a threshold current of 0.5 A (20 A cm^{-2}), while maximum power is obtained from the 5134Å transition ($4p\ ^4D^o_{5/2}$ - $4s\ ^2P_{3/2}$).

Over the next four years (1964 - 8) considerable progress was made in improving the power outputs available from a fixed volume of active medium, both through the development of improved discharge tubes and through the use of longitudinal magnetic fields; and in producing stable, single mode or mode locked outputs. None of these developments, however, altered the basic discharge processes responsible for population inversions, apart from the use of a longitudinal magnetic field. Results from experiments on quartz capillary discharges are therefore equally relevant to argon lasers employing more sophisticated methods of containment.

Some of the more important developments in argon laser technology during this period are now summarized.

Bridges and Halstead (1966)[5] reported total output powers of up to 8.5 watts from a 46 cm long 4 mm bore quartz discharge tube at a current of 45 A (350 A cm^{-2}) in the presence of a longitudinal magnetic field of 1000 gauss. In 1965, Labuda et al[6] established that laser power output increases monotonically with increasing discharge current, and that the power output is limited through the current limitation set by the destruction of the quartz capillary under positive ion bombardment (maximum power dissipation in quartz approximately 140 W cm^{-2}).

By using a ceramic discharge tube (3.5 mm bore, 50 cm long) Paananen (1966)[7] was able to overcome the current limitation set by

the quartz capillary, and reported a total output power of 14 watts at a current of 75 A (800 A cm^{-2}) in the presence of a magnetic field. There was evidence at these current densities that the output saturated and then decreased with increasing current. Using a similar discharge to the above, Paananen (1966)[8] also reported cw oscillation in Ar III at 3511Å. An output power of 13 mW was obtained at a discharge current of 72 A.

Labuda et al[6], Rigden[9], Hernqvist and Fendley[10] and McMahan[11] investigated a range of materials in attempts to replace quartz as the confinement material for the discharge. These included molybdenum, aluminium, tantalum and pyrolytic graphite. Since the wall of the discharge tube is electrically conducting when such materials are used, it must be constructed in the form of short segments, each segment being insulated by a suitable spacer material from its neighbours. (In the case of pyrolytic graphite, it is also possible to use a continuous wall[11].)

By going to larger bore quartz discharge tubes (10 mm) Boersch et al[12] in July 1967 succeeded in producing continuous output powers of the order of 100 watts at currents of the order of 300 A (400 A cm^{-2}) in the absence of a magnetic field. In October 1968 the same group (Banse et al[13]) reported non-resonant laser oscillation at 4880Å and 5145Å. Output powers of the order of 1.5 watts were achieved without the need for cavity mirrors. The single pass gain in this mode of operation is about 10 dB m^{-1}. This compares with single pass gains of the order of 1 dB m^{-1} for narrow bore tubes at current densities around 300 A cm^{-2} (Sayers[14]).

In order to reach the current densities that produce saturation of power output in the large bore tubes, Boersch et al (1970)[15] devised an argon ion laser where the capillary was constructed in anodized aluminium segments (bore 12 mm). Power output was found to depend on

the product of current density with tube radius (JR) and to reach a maximum value at around JR = 170 A cm^{-2} (400 A cm^{-2}). Maximum power output on all transitions of Ar II was 105 W m^{-1} at filling pressures around 1 Torr. The saturation of power output for transitions of Ar II was found to correspond to the threshold for Ar III oscillation, and for JR values around 250 A cm^{-1} (420 A cm^{-2}) two Ar III transitions (3511, 3638Å) produced a total coherent output power of 3.0 W. It appears that excitation to Ar III states is responsible for the depletion of the population inversion of Ar II states. Other investigations involving Ar II and Ar III excitation with large bore tubes have been reported by Banse et al[16] and Herziger and Seelig[17].

Two novel methods for the electrodeless excitation of cw argon ion lasers are due to Goldsborough et al[18,19]. Both involve using rf electric fields to excite the discharge; in the one case the power being coupled in using the transformer principle, while in the other through cyclotron resonance. Neither of these methods have proved as convenient as dc excitation.

In summary, therefore, the principal stages in the development of the cw argon ion laser have been:

(i) the development of narrow bore (1.5 - 4 mm) discharge tubes to the limit set by quartz erosion (350 A cm^{-2});

(ii) the replacement of quartz by ceramic or segmented metal tubes to allow high current densities to be achieved (100 A cm^{-2}) combined with the use of a longitudinal magnetic field;

(iii) finally, the development of large bore (10 - 15 mm) discharge tubes in either quartz or segmented aluminium sections not requiring magnetic fields but requiring large total currents (I = 500 A, J = 500 A cm^{-2}).

If large total output powers (100 watts) are required then large bore tubes with large discharge currents must be used, but if more

moderate powers are sufficient (10 watts) the narrow bore tube with axial magnetic field is much more convenient.

At present fourteen cw laser transitions of Ar II are known, and these are listed in table A.1 together with level designations.

In the next section (§ 2) basic data on the energy level structure, transition probabilities and lifetimes associated with the Ar II ion are considered, and this is then followed in § 3 by a review of the experimental and theoretical investigations on the argon ion laser discharge. These two sections provide the background necessary for § 4 where excitation mechanisms are discussed. Practical details about the construction of quartz envelope argon ion lasers are given in Ch. 2.

A.2 The Argon Ion

A.2.1 Argon II energy levels

The most comprehensive investigation of the Ar II spectrum is due to Minnhagen[20], who observed some 2000 lines, ascribable to 320 Ar II energy levels, in the wavelength range 200 - 12500Å.

The configurations of Ar II of relevance to the argon ion laser are of the form $3s^2\ 3p^4\ n\ell$. The parent configuration (Ar III), $3s^2\ 3p^4$, is essentially governed by LS coupling, so that the designation of the parent levels is $^3P_{2,1,0}$, $^1D_2$, $^1S_0$. A consequence of the predominantly LS coupling is that the splittings of the ^3P levels due to spin-orbit coupling are small compared to the separations of the ^3P, ^1D and ^1S terms. When the outer electron of Ar II is added to the Ar III parent its associated coupling energies are larger than the spin-orbit energy of the $3p^4$ core for low n and ℓ values and hence are describable by LS coupling, whereas for high n and ℓ values they are smaller than the spin-orbit energy of the $3p^4$ core and so must be described in terms of $J_c\ell$ or J_cj coupling depending on the magnitude of the spin-orbit interaction

of the outer electron. The configurations of principal interest here (3d, 4s, 4p, 4d, 5s) correspond to the former case. In general the coupling of the outer electron is smaller than the mututal electrostatic interaction of the core electrons, but in the $3p^4$ 3d case it becomes of comparable magnitude, and so in this latter case the parent term assignment is less significant.

In the argon ion laser the configurations of particular interest are all associated with the ^3P parent term, which, following Hund's rule, is the ground term of Ar III. Since transitions involving core changes are much less probable than transitions between configurations with the same core, only the ^3P parent term need by considered in this context.

The following configurations are of particular interest (Figure A.1): the $3p^4$ (^3P) 4p configuration since it contains the majority of the upper laser levels of Ar II, the $3p^4$ (^3P) 4s configuration since it contains the short lived lower laser levels as well as metastable levels of interest in relation to the pumping cycle, the $3p^4$ (^3P) 3d configuration since it also contains metastable levels of relevance to the pumping cycle, the $3p^4$ (^3P) 4d configuration since this is a source of cascade pumping to the 4p levels, and finally the $3p^5$ ground configuration with levels $^2P_{1/2,3/2}$.

The excited configurations contain both doublet and quartet terms (Figure A.2). In the case of pure LS coupling, radiative transitions involving spin changes are forbidden, and so transitions between doublet and quartet levels are only to be expected when deviations occur from pure LS coupling.

In the case of the 4d configuration LS coupling is in general a valid approximation, particularly for the quartet levels. Irregularities in the positions of the (^3P) 4d ^2D and (^3P) 4d ^2P terms indicate strong perturbations, probably due to interactions with the (^1D) 3d ^2D and

(^{1}S) 3d ^{2}D terms in the former case and the (^{1}D) 3d ^{2}P term in the latter.

The levels of the 3d configuration are distributed over a very large energy range (19000 cm^{-1}), which is about ten times the energy range covered by the $^3P_{2,1,0}$ parents), and hence an LS coupling scheme is in order here. The quartet terms of this configuration exhibit zero non-diagonal matrix elements due to electrostatic interactions, and small non-diagonal elements due to spin-orbit coupling, which means that they do not interact to any extent with other terms belonging to this or any other configuration. In the case of the doublet terms, however, the (^{3}P) 3d ^{2}P and (^{1}D) 3d ^{2}P exhibit a very strong mutual interaction, and the (^{3}P) 3d ^{2}D, (^{1}D) 3d ^{2}D and (^{1}S) 3d ^{2}D terms as well as exhibiting mutual interactions are also thought to be subject to extra-configurational interactions. In particular it is thought that in the case of (^{3}P) 3d ^{2}D the extra configurational interaction is with the (^{1}D) 4s ^{2}D term, and in the case of (^{1}S) 3d ^{2}D with the (^{3}P) 4d ^{2}D term. The anomalously high position of the (^{1}D) 3d $^2S_{1/2}$ level is considered to be due to extra-configurational interactions with deeper quantum levels.

In the 4p configuration the electrostatic coupling energies associated with the external electron are now much smaller than in the 3d case, but they are still larger than the spin-orbit energy of the core, and so the LS coupling scheme is adequate for their description. The quartet terms do not interact electrostatically with one another or with other terms.

In the 4s configuration the coupling is also well described by the LS scheme.

A.2.2 Transition probabilities

Shortly after the discovery of the Ar II laser transitions in 1964, Statz et al[21] calculated transitions probabilities for transitions

between levels of the $3p^4$ (^3P) 4p and $3p^4$ (^3P) 4s configurations and the $3p^4$ (^3P) 4s and $3p^5$ configurations of Ar II. This was an extension of earlier work of Garstang[22]. In 1967, Rudko and Tang[23] extended the calculations of Statz et al to cover all transitions from the 4p levels (transitions to 3d levels now being included), as well as transitions from the 5s and 4d configurations to the 4p configuration (with the aim of assessing the part played by the 4d and 5s levels in cascade pumping of the 4p levels). In 1968, Koster et al[24] published corrections to the original transition probabilities of Statz et al for transitions from the $3p^4$ (^3P) 4s to the $3p^5$ configuration; finding that the transition probabilities for transitions from the 4s lower laser levels were a factor of 5 larger than originally thought. These calculations have been confirmed by Kitaeva et al[25]. In tables A.2 - A.4 transition probabilities for the 4p - 4s, 4p - 3d, 4s - $3p^5$ and 4d - 4s transitions are listed using the previous references as the sources.

Experimental investigations on relative intensities of transitions in Ar II were firstly carried out by Olsen[26]. Comparison of the relative intensities of transitions originating from a common upper level provides an experimental method for determining relative transition probabilities (provided the source is optically thin). Unfortunately the original work of Olsen was too incomplete to allow this to be done effectively, but Rudko and Tang carried out detailed spectroscopic measurements of absolute spontaneous intensities for transitions from all 4p to all 4s and 3d levels, and for transitions from 4d and 5s levels to 4p levels. In the greater majority of cases, calculated and experimentally deduced transition probabilities agree to better than 30%. From the experimentally determined absolute spontaneous intensities and the theoretical values for the transition probabilities, Rudko and Tang[23] calculated population densities and pumping rates for the 4p, 4d and 5s levels under discharge conditions appropriate

to the Ar II laser. These values for the 4p and 4d levels are also tabulated in tables A.2 and A.4 respectively.

Kitaeva et al[25] have calculated population densities for the 4p and 4s configurations using theoretically-determined pumping rates. Since these calculations depend on electron density and electron temperature, as well as calculated excitation cross-sections, they will be considered later in § 4.

Bennett et al[27] have determined experimentally total radiative lifetimes for the 4p states, and these are given in table A.2. The total radiative lifetime measurements of Bennett agree closely (20%) with the calculated values due to Statz et al[21].

The following general statements regarding transition probabilities in the argon ion can be summarized from the data given in tables A.2 - A.4:

(i) For transitions between the same pair of configurations, transition probabilities are roughly an order of magnitude smaller for transitions involving spin changes compared with transitions not involving spin changes. (The former only occur at all because of deviations from pure LS coupling.)

(ii) In the $3p^4$ (^3P) 4s configuration the levels are $^2P_{1/2,3/2}$ and $^4P_{1/2,3/2,5/2}$. Since the ion ground states are doublet states, and since LS coupling is valid approximately, the decays of the quartet 4s states to the ground states are slow compared to the decays of the doublet 4s states to the ground states. As a consequence there is two orders of magnitude difference in radiative lifetime between quartet and doublet 4s states; the latter being short lived enough to be lower laser levels for transitions from the 4p configuration.

(iii) Transition probabilities for 4d - 4p transitions are generally about half an order of magnitude greater than for 4p - 4s transitions. (The influence of spin change considered in (i) applies to both these

sets of transitions.)

Average values for transition probabilities between different configurations are summarized in fig. 1A. These refer to transitions not involving spin changes.

A.3 Argon Laser Discharge

Comprehensive investigations of the basic plasma parameters of the argon discharge operating as the active medium of a laser have been carried out by three groups; namely that under the direction of V. F. Kitaeva at the Lebedev Physics Institute, Moscow (source R)[25,28-32, 41], that under the direction of W. R. Bennett, Jr. at Yale University, New Haven (source Y)[27, 39, 42-44, 46], and that at Bell Telephone Laboratories, Murray Hill (source B)[4,6,33,38,45,47,49,51], involving E. I. Gordon, E. F. Labuda, R. C. Miller, C. E. Webb and A. N. Chester. In this section the findings of these different groups are critically compared, starting with those plasma parameters that can be more or less directly deduced from experimental observation and progressing to those where a theoretical model of the discharge has to be invoked. Background data which relates to argon discharges and which is generally agreed upon by the different groups is first of all summarized. By typical discharge conditions in the following is meant a quartz walled 2 mm capillary diameter discharge in argon gas at a filling pressure of 0.5 Torr and a current of 10 A.

A.3.1 Gas atom density

Since the gas temperature in the constricted region of the discharge is considerably higher than room temperature (A.3.4), and this region is connected to larger volumes containing cold gas, the gas density in the capillary is reduced from that corresponding to the filling pressure. Assuming gas-pressure equilibrium, the number density under discharge conditions can be estimated from the gas law

$$N_o = N_o^{(o)} (300/T_o) \qquad (A.1)$$

where $N_o^{(o)}$ is the number density at the filling pressure and T_o is the neutral atom temperature during operation. However, this relation must be treated with some caution for several reasons. First, at the lower pressures the atom mean free path (A.3.2) can become comparable to the tube radius, so that gas-pressure equilibrium is not a realistic assumption. Second, radial inhomogeneities in gas atom density can occur at large current densities[34,49]. Webb[49] reports evidence from X-ray absorption measurements that the average gas density in the active discharge is greater at low pressures (< 1 Torr) than predicted by equation A.1. Finally, under certain conditions to be discussed in A.3.7 a pressure gradient can arise along the capillary axis.

A.3.2 Mean free paths, Debye length

Chester[33] and Webb[49] have summarized theoretical and experimental data on argon atom and argon ion mean free paths. On the assumption that equation A.1 is valid, the argon atom mean free path is given by

$$\lambda_o \text{ (mm)} \simeq 0.05 \ (T_o/300)/p_o \qquad \text{(A.2)}$$

where p_o is the filling pressure in Torr. The argon ion mean free path, determined by charge exchange collisions, is similarly given by

$$\lambda_i \text{ (mm)} \simeq 0.03 \ (T_o/300)/p_o \qquad \text{(A.3)}$$

Hence in a typical argon laser discharge atom and ion mean free paths are comparable and of the order of the capillary bore.

Momentum transfer cross-sections for electrons in argon have been reviewed and measured by Frost and Phelps[52]. In the electron energy range 1 - 10 eV, the momentum transfer (or total elastic) collision cross-section for electrons with neutral argon is approximately $10^{-16} E_e$ cm^2 where E_e is the electron energy in eV. The electron mean free path for elastic collisions with neutral argon is therefore

$$\lambda_e \text{ (mm)} \simeq (3/p_o \ E_e)(T_o/300) \qquad \text{(A.4)}$$

The electron mean free path against Coulomb scattering through greater than 90° (single collision) by the argon ions can readily be calculated as[52]

$$\lambda_{e-i} \text{ (mm)} \approx 2 \times 10^{14} E_e^2/N_e \text{ (mm)} \qquad (A.5)$$

where N_e is the electron density (cm^{-3}). Under typical operating conditions therefore the electron-ion and electron-neutral mean free paths are comparable and somewhat larger than the capillary diameter.

Another important parameter is the plasma shielding distance or Debye length. This is related to electron density (N_e cm^{-3}) and electron temperature (T_e eV) by[53]

$$\lambda_d \sim 7 \times 10^2 (T_e/N_e)^{\frac{1}{2}} \text{ cm} \qquad (A.6)$$

Under typical discharge conditions the Debye length is much less than the capillary diameter.

The axial electric field in the capillary region of the discharge depends only weakly on discharge current and filling pressure, and varies inversely as the tube bore[33]. Its behaviour is summarized by the empirical formula

$$X \text{ (volts cm}^{-1}) = 12.3/D \text{ (mm)} \qquad (A.7)$$

The observed variation of X/p with pressure for a 2 mm bore tube is shown in fig. A.24.

A.3.3 Gas temperature

Gas temperatures in the discharge have been determined from the linewidths of Ar I transitions. These transitions exhibit a predominantly Doppler profile. Measurements have been carried out by all three groups (source R[29], source B[33] and source Y[39,50]) and there is reasonable agreement over gas temperatures so deduced. A comparison is made in fig. A.3. The gas temperature is roughly independent of pressure in the range 0.1 - 0.6 Torr, and increases linearly with current. Chester has summarized the findings of the Bell Lab. investigators by the empirical formula[33]

$$T_o/300 = 1 + 0.02 \, J \, D^{\frac{1}{2}} \qquad (A.8)$$

where J is the current density (A cm^{-2}) and D is the tube bore (mm), and this relation is confirmed by the other investigators. There is

some evidence (source Y[50]) that in going to higher pressures (> 0.6 Torr) the gas temperature decreases by about 20%.

A.3.4 Ion temperature

Ion temperatures have been deduced by a Voigt profile analysis of several Ar II line profiles observed axially (Ar II line profiles observed radially are complicated by ion drift velocities due to the large radial electric field in the discharge - see A.3.6 and A.3.7). Measurements are reported in both source R[29] and Y[39,50]. The ion temperature increases approximately linearly with current density in a similar fashion to the gas temperature. At the lower pressures (< 0.6 Torr) it is invariably higher than the gas temperature (source Y[50] by about 500 K, source R[29] by about 1500 K), and is approximately independent of pressure. At higher pressures it falls with pressure to approach the gas temperature as expected (source Y[50]). The behaviour of ion temperature with discharge current is summarized in fig. A.4.

A.3.5 Electron density

Electron densities in the argon discharge have been determined by (i) introducing small amounts of hydrogen into the discharge and measuring the Stark broadening of the H_α and H_β lines (source R[29], source B[38]), (ii) probe measurements - these being confined to lower discharge currents (source B[38]), (iii) microwave cavity techniques (Pleasance and George[40]) and (iv) Voigt analysis of the Ar I line profiles, ascribing the extracted Lorentz widths to Stark broadening (source Y[50]). The various measurements are summarized in figs. A.5 - A.7.

A direct comparison is not immediately possible since different discharge conditions are covered by different investigators. However the Bell Lab. investigators observe that electron density is proportional to the product of discharge current density and filling pressure ($J\ p_o$) except in the low current, low pressure range where the discharge exhibits an instability. In fig. A.8 electron density has been plotted as a

function of J p_o to allow the measurements of different investigators to be compared. The linear dependence in J p_o is seen by all investigators. There are however discrepancies in absolute magnitudes, most notably the Yale results which are a factor of ten larger than those of others. In view of the assumptions about the Stark broadening mechanism for the Ar I transitions and difficulties in extracting small Lorentz widths from the Ar I line profiles, too much reliance cannot be placed on the Yale results. Other investigators agree on absolute magnitudes to within a factor of three. Kitaeva et al have also deduced electron densities from their measurements of electron temperature (A.3.6) and plasma conductivity[37]. Electron densities so derived were found to agree to within a factor of two with their values obtained directly by Stark broadening (fig. A.5).

Electron density measurements in argon ion laser discharges may be summarized by the empirical formula[33]

$$n_e = \text{const. } J\ D\ p_o \qquad (A.9)$$

where the symbols have their usual meanings. Apart from uncertainties over absolute magnitudes there is general agreement over the dependence of electron density on discharge parameters.

A.3.6 Electron temperature

Electron temperatures have been determined by (i) probe measurements (B[38]) and (ii) linewidth (R[29,31]) and line profile (Y[50]) measurements on argon II transitions.

Because of erosion problems, probe measurements are restricted to low current densities (< 100 A cm^{-2}). The results are summarized in fig. A.9 and indicate that the electron temperature is approximately independent of discharge current density and decreases with increasing pressure. Under typical operating conditions the electron temperature as indicated by probe measurements is around 30000 K. The dependence of electron temperature on p_oD product was also investigated using probes

and these results are shown in fig. A.10. At constant discharge current, the electron temperature is independent of p_oD for values of p_oD above about 4 Torr-mm.

The above findings are at variance with estimates of electron temperature using linewidth or line profile techniques. In both these spectroscopic techniques the broadening of Ar II transitions when viewed transverse to the discharge tube axis is measured. The additional broadening so observed is a consequence of a drift velocity superimposed on the ion random velocity by the strong radial electric field in the plasma. This radial electric field may be related to electron temperature - roughly speaking the radial potential drop between tube axis and the beginning of the wall sheath is of the order of $k\,T_e/q_e$ where q_e is the electronic charge, but the exact details depend on the discharge model assumed.

Kitaeva et al[29,31] analysed their experimental measurements using the Kagan-Perel[35,36] theory of the discharge, which relates the transverse ion temperature ($T_\perp$) to the electron temperature T_e by

$$T_\perp = 0.56\,T_g + 0.13\,T_e \qquad (A.10),$$

where T_g is the gas temperature and the condition of an ion mean free path greater than the tube bore is assumed. Electron temperatures so deduced are shown in fig. A.9 as a function of current density with filling pressure as a parameter. The observed linear increase of electron temperature with current density is at variance with the findings of Labuda et al.

More recently Sze and Bennett[50] have repeated the linewidth measurements using a Fabry-Perot system with a much higher finesse than that of Kitaeva et al, so that detailed line profiles were obtained for the Ar II transitions. These profiles were then analysed in terms of a distribution of drift velocities superimposed on the distribution of ion random velocities. The distribution of drift velocities for

the excited ions was calculated on the basis of an ion free fall model and an assumed dependence of radial electric field on radial position in the plasma region of the discharge. Hence from the measured profiles the radial electric field was calculated, therefore allowing electron temperatures to be deduced. The measurements of Sze and Bennett are also shown in fig. A.9. In this case the electron temperature is observed to increase initially with increasing current density, but then to saturate above about 200 A cm^{-2}. Magnitudes are comparable to those reported by Labuda et al (30000 K), but are about a factor of two to three down on those of Kitaeva et al.

The behaviour of electron temperature with discharge parameters, in particular current density, is therefore a region of controversy at present. Discrepancies may have arisen due to the use of different discharge tube geometries - in particular the inclusion or otherwise of a gas return path. In the absence of such a return path, the number density of neutral argon atoms in the capillary would decrease with increasing current due to gas pumping and this could in itself lead to an increase in electron temperature with increasing discharge current. As well as this experimental uncertainty, the different discharge models assumed in interpreting the line profile data also lead to different conclusions about electron temperature (see for example Sze and Bennett[50]).

A.3.7 Drift velocities, gas pumping

The axial drift velocity of the electrons can readily be calculated knowing the electron density and the discharge current density. Drift velocities determined in this way from the electron density measurements due to the investigators at Bell Labs. are shown in fig. A.11. Electron drift velocity is inversely proportional to p_oD product, and is independent of discharge current density.

Ion and neutral atom axial drift velocities have been investigated both by Ballik et al[39] and by Kitaeva et al[30,41] by observing the shifts of line centres as seen from opposite ends of the discharge tube. There are discrepancies between the measurements of the different investigators.

In the case of the neutrals, Ballik et al reported no measurable drift velocity, but Kitaeva et al[41] reported drift velocities comparable to those of the ions. The results of Kitaeva et al are summarized in fig. A.12, and show that the neutral drift velocities are of the order of 10^4 cm sec^{-1}, and increase both with increasing current and decreasing pressure. A possible explanation of the discrepancy between the two is the role played by a gas return path in the discharge tube. The mechanism of gas transfer from the cathode to the anode regions of the argon discharge has been extensively studied both theoretically and experimentally by Chester[33,42]. In the absence of a return path from anode to cathode the gas pressure increases in the anode region and decreases in the cathode, the equilibrium pressure difference corresponding to a reduction of the neutral drift velocity to zero. If a gas return path is included, a pressure difference cannot build up, so there is a continual transfer of neutral gas atoms from cathode to anode, and hence a drift velocity associated with the neutrals. If simple kinetic theory arguments are used to relate the pressure difference, Δp, between anode and cathode with no gas return path, to the neutral atom drift velocity, v_g, with a gas return path, namely

$$\Delta p/p_o = W v_g^2 / (2RT_g) \qquad (A.11)$$

where p_o is the gas filling pressure, W the molecular weight and T_g the gas temperature in the capillary, then pressure differences so deduced from the measured drift velocities of Kitaeva et al[41] are in reasonable agreement with pressure differences experimentally observed by Chester[33]. Also, the variation of neutral atom drift velocity with

discharge current and discharge pressure is consistent with the observed variation in pressure difference with these parameters.

In the case of the ion axial drift velocity, experimental results of different investigators do not agree, although it is in general difficult to make direct comparisons. In fig. A.13, the later results of Kitaeva et al (1970)[41] for the variation of ion drift velocity (from cathode to anode) with discharge current and discharge pressure are shown.

The ion axial drift velocity is observed to decrease with increasing current and to increase with increasing pressure. These findings are not consistent with earlier measurements of Kitaeva et al (1967)[30] which were made on a 1.6 mm bore as opposed to a 2.8 mm bore tube. In the earlier measurements and for the current density regime shown in fig. A.13, the ion drift velocity was reported to be about one order of magnitude greater (3×10^4 cm sec^{-1}) and to decrease with increasing pressure. A comparison of the two sets of measurements due to Kitaeva et al with those of Ballik et al is made in fig. A.14. Ballik et al's measurements of ion drift velocity show a distinct maximum in their variation with pressure, and this behaviour is not seen in any of the measurements due to Kitaeva et al. Ion drift velocities therefore need re-investigation in view of the considerable discrepancies between investigators.

The difficulty may in part be due to the sensitivity of ion drift velocity to the ratio of ion mean free path to tube bore. If the ion mean free path is greater than the tube bore ($\lambda_i > D$) momentum loss is through free fall to the walls under the influence of the radial electric field, whereas if the mean free path is less than the tube bore ($\lambda_i < D$), momentum loss is through collisions within the volume of the tube. In the former case the loss rate is dominated by the variation of radial electric field with discharge conditions. Since this decreases with increasing pressure and increases with increasing current, the loss

rate decreases with increasing pressure and increases with increasing current, and as a consequence the ion drift velocity is expected to increase with increasing pressure and decrease with increasing current. This is the behaviour observed in the later work of Kitaeva et al (1970)[41]. In the latter case when volume effects are significant an increasing pressure leads to an increasing loss rate and so a decreasing ion drift velocity. When the ion mean free path is comparable to the tube diameter, the condition prevailing in the laser discharge, the behaviour of ion drift velocity is likely to be sensitive to the precise boundary conditions on the discharge.

Since little reliance can be placed on ion axial drift velocity measurements their use by Kitaeva et al[41] to calculate ionization rates for the electrons is open to question.

The special case of the radial drift velocity for the ions has already been discussed in section A.3.6. Typically radial drift velocities (10^5 cm s^{-1}) are a factor of 10 larger than the axial drift velocities (10^4 cm s^{-1}).

A.3.8 Influence of environment on homogeneous linewidths and lifetimes

If the spontaneous emission lineshape associated with an Ar II transition is investigated by high resolution spectroscopy, it can be analysed as the convolution of a Doppler (inhomogeneous) profile with a much narrower Lorentzian (homogeneous)profile. The homogeneous linewidth is related to the decay rates of the upper (1) and lower (2) levels of the transition according to

$$\Delta\nu = (A_1 + C_1 + A_2 + C_2)/2\pi,$$

where the A's are radiative decay rates and the C's describe collisional effects. As well as deducing ion temperatures from the line profile, it is also possible, therefore, to investigate decay rates of the upper and lower levels of the transition.

High resolution spectroscopy of the Ar II transitions has been carried out by Bennett et al[44,46,50] and by Webb and Miller[45], using scanning Fabry-Perot interferometers. The interpretation of the earlier measurements[44] of Bennett et al on homogeneous linewidths is confused by the use of incorrect calculated values for the radiative lifetimes of the lower levels, so only the later work of this group[46,50] together with the work of Webb and Miller[45] will be considered here.

Webb and Miller investigated the homogeneous linewidths of the 4880Å ($4p\ ^2D_{5/2}$ - $4s\ ^2P_{3/2}$) and 4348Å ($4p\ ^4D_{7/2}$ - $4s\ ^4P_{5/2}$) transitions in Ar II as a function of discharge filling pressure. For both these transitions the radiative lifetimes of the upper levels, as calculated, are comparable (9 nS), but the former transition has a lower level with a lifetime (0.4 nS), much shorter than the lifetime of its upper level, while the latter transition has a lower level with a lifetime much longer than the lifetime of its upper level. In the case of the 4880Å transition, therefore, the homogeneous linewidth is expected to be due predominantly to the radiative lifetime of its lower level (430 MHz) together with broadening due to environmental effects (Stark effects, collisions, etc.), while in the case of the 4348Å transition the linewidth is expected to be due predominantly to its upper level lifetime (27 MHz) together with environmental effects. If environmental effects are similar for both transitions (i.e. $C_1 = C_1'$, $C_2 = C_2'$), the difference between their homogeneous linewidths is independent of discharge conditions and is determined predominantly by the radiative lifetime of the $4s\ ^2P_{3/2}$ level. This was found to be the case by Webb and Miller; the experimentally determined difference in linewidths (480 MHz) agreeing closely with that expected from the $4s\ ^2P_{3/2}$ level lifetime, and being independent of filling pressure over the range 0.2 to 5.0 Torr. The latter finding is evidence that transitions from the $4s\ ^2P_{3/2}$ level to the ground state do not experience radiation trapping up to a pressure of 5.0 Torr.

The homogeneous linewidth of the 4348Å transition was found to be much greater than expected if due only to the radiative lifetime of the upper level. It also varied with discharge filling pressure (fig. A.15) exhibiting a minimum of about 200 MHz in the pressure range 1 - 2 Torr, and increasing with both increasing and decreasing pressure.

Bennett et al[46,50] have also reported a dependence of homogeneous linewidth on discharge conditions, having investigated the current dependence of homogeneous linewidth for seven Ar II transitions (4579Å, 4880Å, 4658Å, 4965Å, 4727Å, 5145Å, 4765Å). The results for all seven transitions are similar and those for the 4765Å transitions ($4p\ ^2P_{3/2}$ - $4s\ ^2P_{1/2}$) are shown in fig. A.16. Bennett et al also observe a decrease in width with increasing pressure for the lower pressures (fig. A.15), but their measurements do not extend to high enough pressures to see the subsequent increase in width reported by Webb and Miller.

The explanation of the changes in the homogeneous width is by no means clear at present. Bennett has considered two mechanisms.

(i) Small angle ion-ion scattering producing phase interuptions during the radiative lifetimes of the 4p states and hence an increase in homogeneous widths. Since the ion-ion scattering rate varies as $N_i(T_i)^{-3/2}$, the homogeneous width would hence be expected to decrease with increasing current (since both N_i and T_i increase approximately linearly with current) whereas the experimental indications are that it increases.

(ii) Stark broadening through electron impacts. Experimental and theoretical determinations of the Stark broadening coefficients by Roberts[60,61] indicate values larger by a factor of about three than those originally predicted by Griem [54]. The half width (full width at half maximum intensity) due to Stark broadening by electron impacts is given by

$$\Delta\nu_s = \Omega(T_e)\ N_e\ ,$$

where $\Omega(T_e)$ is a strongly varying function of T_e. For T_e = 30000 K, Roberts gives a value for Ω of approximately 2 x 10^{-13} MHz cm^3 for the 4880Å transition. The measured increase in homogeneous width of this transition at 150 A cm^{-2} is 200 MHz. An electron density of about 10^{15} cm^{-3} is hence required to explain the increase in terms of Stark broadening. Measured values of electron density range from 2.5 x 10^{13} to 2.5 x 10^{14} cm^{-3} - the upper limit being the value given by Bennett using Stark broadening measurements on neutral argon transitions. The observed increase in homogeneous linewidth can therefore only be explained in terms of Stark broadening if the higher values for electron density are accepted. Even then the observed dependence of homogeneous linewidth on discharge parameters does not correlate well with the variation of electron density with discharge parameters.

Vladimirova et al[62] have investigated the collisional destruction of the 4p states by a perturbation spectroscopy technique. In fig. A.17 the dependences of the lifetimes of the 4p $^2D_{5/2}$ and 4p $^4D_{5/2}$ states on discharge current and pressure are shown. The decrease in lifetime with both increasing pressure and increasing current implies that electron collisions are responsible for the collisional decay of the states. For discharge conditions appropriate to laser oscillation the collisional decay constants for the 4p $^4D_{5/2}$ and 4p ^{2} $_{5/2}$ levels are estimated at 10^{-6} N_e s^{-1} and 6 x 10^{-7} N_e s^{-1} respectively where N_e is the electron density (cm^{-3})†. Estimates of 4p to 4s de-excitation cross-sections by

† These decay constants were calculated from the lifetimes using the electron density measurements of Kitaeva et al. In discussing the variation with discharge parameters of the broadening due to de-excitation it is better, therefore, to revert to the basic lifetime data, since then uncertainties in the electron density measurements are avoided.

applying detailed balancing to the results of Beigman et al suggests that these decay constants only depend weakly on electron temperature,

changing by less than 10% over the range 2 - 8 eV. For the 4p $^2D_{5/2}$ level the contribution that the collisional destruction process makes to the homogeneous linewidth is hence

$$\Delta\nu_c \sim 10^{-13}\ N_e\ \text{MHz},$$

where $\Delta\nu_c$ is the full width at half maximum intensity. Since the upper level lifetime changes at most by a factor of about two and the lower level lifetime dominates the homogeneous linewdith, the collisional destructive process has little effect on the homogeneous linewidth and hence cannot explain its variations with discharge conditions. It should be pointed out that the Stark broadening calculations of Griem and Roberts specifically exclude collisional de-excitation (neglect of back reaction) which must hence be considered as a separate process.

It is apparent that more detailed experimental and theoretical considerations of the mechanisms of line broadening for the argon ion laser transitions are required so that the different contributions can be more realistically assessed.

Bennett et al[50] have also investigated the homogeneous linewidths of neutral argon transitions in the discharge. Observed widths on the three 5p - 4s transitions studied (4201Å, 4259Å and 4702Å) were enormously larger than expected on the basis of radiative decay alone. Bennett et al used the Griem theory of Stark broadening by electron collisions to deduce electron densities from the measured homogeneous widths of the above neutral argon lines, and these measurements have already been discussed in section A.3.5.

A.3.9 Level populations

The variations in the populations of excited states of Ar I and Ar II with conditions in the capillary bore of the argon discharge are important in studying excitation mechanisms in the argon ion laser. The most extensive investigation to date is by Gordon et al[38,47], but work has also been carried out by Rudko and Tang[23] and Vladimirova et al[63].

The distribution of populations within an Ar II configuration under discharge conditions appropriate to laser oscillation exhibits a thermal character, making it possible to define for each configuration an effective "intra-configurational" temperature[47,23]. This temperature varies from configuration to configuration; decreasing progressively in going to the higher configurations (fig. A.18). Even the higher intra-configurational temperatures (e.g. 0.5 eV for the 4p configuration) are far removed from the electron temperature in the discharge, which suggests that if thermalization is occurring within a configuration, it is brought about by colder species in the discharge (ion-neutral, ion-ion collisions) as opposed to the electrons.

Gordon et al[38] and Vladimirova et al[63] have studied the dependence on discharge conditions of the populations of radiating levels of neutral and ionic argon by emission spectroscopy, and of metastable neutral and ionic levels by the Ladenburg-Reiche absorption technique. Typical behaviour of the populations of these four classes of levels as a function of discharge current is summarized in figs. A.19 - A.22. The general conclusions that can be drawn about level populations from these observations are;

(i) Up to the 5d configuration the populations of the radiating levels of neutral argon are only weakly dependent on current density, showing a tendency to decrease slowly with increasing current density. For the 5d configuration and above level populations increase with increasing current density (fig. A.19).

(ii) Metastable level populations of neutral argon are only weakly dependent on current density, again showing a tendency to decrease with increasing current density (fig. A.20).

(iii) Populations of radiating levels of Ar II are a quadratic function of discharge current density (fig. A.21).

(iv) Metastable level populations of Ar II are a linear function of discharge current density (fig. A.22).

By a consideration of a simple rate equation describing the steady state populations of the excited levels, Gordon et al were able to draw several important conclusions regarding excitation and relaxation mechanisms for these levels. These conclusions may be summarized as follows:

(i) Since the populations of both radiating and metastable levels of neutral argon effectively saturate with discharge current, electron de-excitation is the dominant loss mechanism for both. In the case of radiating levels it predominates over losses due to radiative decay, and in the case of metastable levels it predominates over losses due to diffusion to the walls. These conclusions are based on the assumption that the electron temperature, and hence also electronic excitation and de-excitation rates, are independent of discharge current.

(ii) The linear dependence on discharge current of the populations of both the ion ground state and the ion metastable levels is consistent with the metastable levels being created by electron impact excitation from the ion ground level and being destroyed by electron impact de-excitation. In other words, the populations of the ion metastable levels are saturated relative to the population of the ion ground level, in just the same way as the populations of the neutral metastable levels are saturated relative to the population of the neutral ground level.

(iii) The quadratic dependence of the populations of the radiating levels of the ion on discharge current is consistent with these levels being populated by electron impact excitation from the ion ground level as before, but being destroyed by radiative decay. Since, like the ion ground level, the ion metastable levels are linearly dependent on current, the radiating levels could equally be created by electron impact excitation from metastable levels and still show a quadratic current dependence.

As part of the present study, the spontaneous emission intensities of transitions originating on 4p and 4d levels of the ion were measured over extended pressure and current ranges. Spontaneous emission intensities for all the transitions investigated were found to exhibit similar dependence both on discharge current and filling pressure. Since the discharge is optically thin when viewed from the side this implies that the populations of different 4p and 4d levels vary in a similar way with discharge parameters. Intensity variation with filling pressure at a fixed discharge current of 10 A (4 mm bore tube) is illustrated in fig. A.23, while fig. A.24 shows the intensity variation with discharge current at three different pressures. At low pressures (< 0.05 Torr) the populations increase approximately quadratically with current, but as the pressure is increased the current dependence progressively changes until it is greater than cubic at the higher pressures (0.3 Torr).

A summary of the basic parameters associated with the argon ion laser discharge is given in table A.5.

As may be seen from the above, in deducing electron density, electron temperature, etc. from the basic spectroscopic data, various assumptions must be made about the discharge (i.e. a model of the discharge must be adopted). As well as this the deduced parameters are often interrelated. In order to clarify the approaches adopted by the different investigators, two flow diagrams are included (figs. A.26, A.27) which contrast the methods of Kitaeva et al and Bennett et al.

A.3.10 Radial profiles

Webb[49] has investigated the radial variation of Ar I and Ar II excited state populations using a novel "end-on" collimation technique. The principal conclusions that may be drawn from these studies are the following:

(i) In the pressure range 0.2 - 2 Torr the populations of all excited Ar I states are fully saturated across the whole tube diameter at

current densities in excess of 30 A cm^{-2} (A.3.9).

(ii) In the pressure range 0.2 - 2 Torr there is no appreciable radial variation of gas atom number density or of electron energy.

(iii) At the higher pressures 15 - 20 Torr the gas atom number density exhibits a minimum on tube axis and there is a radial variation of mean electron energy.

(iv) Mean electron energy increases slowly with current (A.3.6).

(v) The Ar II excited states decay by predominantly radiative processes and their excitation rate is quadratic in discharge current (electron) density.

A.3.11 Laser power output

The dependence of laser power output on discharge parameters may be summarized as follows:

(i) Sufficiently far from the threshold the laser power output (multimode, multiline) increases approximately quadratically with discharge current. Close to threshold the power output varies more rapidly with current. Typical behaviour is illustrated in fig. A.28. At very high current densities (> 400 A cm^{-2}) - higher than can be observed in a water-cooled quartz tube - the power output starts to saturate with respect to current. The above findings apply to discharge tubes up to 15 mm in bore.

(ii) The laser power output exhibits an optimum with respect to pressure at fixed discharge current. This optimum lies in the range approximately 0.1 - 0.6 Torr for capillary diameters 2 - 4 mm (no magnetic field). Optimum pressure increases slowly with increasing discharge current due to gas pumping. For JD < 100 A cm^{-1}, the optimal pressure is related to tube bore by[12,16]

$$p_o \sim 0.5\ D^{-1}\ (\text{Torr}) \qquad (A.12)$$

where D is in mm and p_o is the filling pressure.

(iii) Power output per unit length of discharge at fixed discharge current density and optimal pressure varies linearly with capillary diameter.

A.4 Excitation mechanisms

Numerous excitation pathways have been proposed to explain the 4p - 4s population inversions in the argon ion laser. It is convenient to consider five distinct mechanisms, although in the active medium excitation probably involves more than one of these mechanisms. The proposed excitation pathways may be summarized as follows (fig. A.29):

(i) Direct electron excitation from the $3p^6$ neutral argon ground state to the 4p upper laser level (mechanism I).

(ii) Electron excitation to an intermediate Ar I metastable state ($1s_{2-5}$) followed by electron impact excitation from this state to the 4p state (mechanism II).

(iii) Electron impact excitation to the Ar II ground state ($3p^5$) followed by electron impact excitation from this ion ground state to the 4p state (mechanism III).

(iv) Electron impact excitation to the Ar II ground state followed by electron impact excitation to a 4d or higher state, followed by radiative cascade to the 4p state (mechanism IV).

(v) Electron impact excitation to the Ar II ground state, followed by electron impact excitation to an intermediate ion metastable state (4s, 3d), followed by electron impact excitation to the 4p state (mechanism V).

Obviously combinations of these excitation processes are possible (for example IV & V).

A.4.1 Mechanism I:

The direct electron impact excitation of the Ar II upper laser states from the neutral atom ground state has been studied extensively both experimentally and theoretically. Koozekanani [55] has applied the sudden perturbation method to calculate cross-sections as a function of electron energy and Vainshtein and Vinogradov[59] have applied Born

approximation calculations taking into account the non-orthogonality of initial and final state wavefunctions. Bennett et al[56], Hammer and Wen[57] and Feltsaw and Povch[58] have measured the cross-sections experimentally by investigating the spontaneous emission radiation from argon gas excited by mono-energetic electrons. In the experimental methods allowance must be made for cascade contributions - i.e. direct electron impact excitation to 4d or 5s states followed by radiative cascade to the 4p state.

Values obtained by different investigations are compared in table A.6, where the cross-sections quoted are those corresponding to the peak in the excitation curve. Below their peak values the cross-sections vary approximately linearly with electron energy and their behaviour may be summarized by the expression

$$Q(E) = Q(\text{peak value}) \times (E - E_{th})/E_{peak} ,$$

where E_{th} is the threshold energy for direct excitation and E_{peak} is the energy corresponding to the peak in the excitation cross-section.

The behaviour with electron energy of the excitation cross-sections for doublet states is contrasted with that for quartet states in fig. A.30.

As a consequence of the large electron energy required to reach threshold in the direct excitation process (35eV) compared to the mean electron energy in the cw laser discharge, the direct excitation process makes a negligible contribution. It is however much more significant in the case of the pulsed argon ion laser.

A.4.2 Mechanisms II-V

In considering these excitation mechanisms, excitation rates for the following processes are required

(a) $Ar + e \rightarrow Ar$ (metastable) $+ e$

(b) $Ar + e \rightarrow Ar^{+} + e$

(c) Ar (metastable) + $e \rightarrow Ar^{+} + e$

(d) Ar (metastable) + $e \rightarrow Ar^{+*} + e$

(e) $Ar^{+} + e \rightarrow Ar^{+}$ (metastable) + e

(f) $Ar^{+} + e \rightarrow Ar^{+*}$ (4p, 4d etc) + e

(g) Ar^{+} (metastable) + $e \rightarrow Ar^{+*}$ (4p, 4d etc) + e

The various proposed excitation mechanisms are different combinations of the above processes.

Webb has analysed excitations and collisional destruction rates for the $1s_{2-5}$ metastable (and quasi metastable) levels of Ar I (processes a & c). His findings are summarized in fig. A.31, where it may be seen that the predominant loss rate from these levels for electron energies above about 1eV is through ionization (process c). Also shown in fig. A.31 is the total population of all $1s_{2-5}$ Ar I levels (expressed as a fraction of the neutral ground state population) deduced from these rates. This should be compared with fig. A.20 which shows the population of the $1s_5$ level as a function of current density as determined by a line absorption technique. The experimental values are consistent with calculated values if an electron temperature of 1.5 eV is assumed for the discharge conditions appropriate to fig. A.20 (2mm bore, 0.45 Torr). It should be emphasized that the $1s_{2-5}$ populations saturate with current at very low currents, and that the saturated values are very sensitive to electron temperatures (fig. A.31). Since metastable destruction is due predominantly to ionization, the production rate for argon ground state ions via metastable states is equal to the metastable production rate.

It is now necessary to compare the two step production process for argon ions with the single step process (c). The cross-section for this process has been measured by Bleakney (1930)[64], and just above threshold ($15.7 < E_e \leq 45$eV) may be approximated by

$7(E_e - 15.7) \times 10^{-18}$ cm^2 where E_e is the electron energy (eV). Assuming a Maxwellian electron velocity distribution direct excitation rates have been calculated from this cross-section as a function of electron temperature and these also are shown in fig. A.31. It may be seen that for the electron temperature range 1-3eV the direct ionization rate is at least an order of magnitude less than that through the $1s_{2-5}$ metastables. Although excitation of the ion ground state is therefore predominantly a two step process, its population is still expected to be a linear function of discharge current since the intermediate populations ($1s_{2-5}$ metastables) are saturated relative to the neutral ground state. The approximately linear dependence of electron density (and hence ion density) on discharge current that is observed experimentally is consistent with this excitation mechanism for the ion ground state.

Excitation processes from the ion ground state either directly to the 4p upper laser levels or through intermediate states are now considered.

Beigman et al[65] (1967) have calculated in the Born-Coulomb approximation pumping rates between the argon ion configurations, and their calculations are illustrated by fig. A.32 (a), which shows absolute rate coefficients ($\langle\sigma v\rangle$) calculated for two electron temperatures, and fig. A.32 (b), which shows relative rate coefficients for the same two electron temperatures. The values quoted refer to excitation to all three core states (^3P, ^1D and ^1S) and the excitation rates for the (^3P) core are approximately 0.6 of the quoted values. Also, the coefficients refer exclusively to the doublet terms in the configuration since pure L-S coupling has been assumed. In order to determine the pumping rate per unit statistical weight, the coefficients should further be divided by 6 for the 4s configuration and 18 for the 4p configuration, these being the total statistical weights associated

with all doublet levels in the 4s and 4p configurations respectively. Using the pumping rates of Beigman et al[65] and their own measurements of electron temperature and electron density, Kitaeva et al[41] have calculated populations (per unit statistical weight) for the 4s and 4p configurations as a function of discharge parameters. In these calculations allowance was made for radiation trapping effects between the ion ground state and 3d states as well as 4s states. The calculations are summarized in table A.8 and are discussed more fully in chapters 3 and 5.

Brandi[66] (1972) has investigated theoretically the distribution of populations between the different 4p levels arising from direct excitation from the ion ground state (process f), assuming the discharge parameters (electron temperature and density) reported by Kitaeva et al. The relative pumping rates for the 4p states are shown in table A.7, where it may be seen that in general pumping rates to the quartet 4p states from the ion ground state are a factor of 2-3 greater than those for the doublet states. This is contrary to the findings of Beigman et al[65], who estimated that pumping rates to the quartet 4p states directly from the ion ground state were a factor of 5-10 less than those to doublet states.

Since pumping rates to individual 3d, 4d, etc. states have not been calculated, it is not possible to compare in detail the direct excitation process from the ion ground state with processes involving intermediate states. Further it is not possible to decide between the different excitation processes on the basis of the current dependence of the 4p populations. This is because the intermediate metastable state populations are saturated relative to the ion ground state (see §A.3.9), and hence like the ground state population increase linearly with discharge current. For both direct and indirect excitation processes a quadratic dependence of 4p populations on discharge current is to be expected.

The excitation process involving radiative cascade from above (process IV) has been investigated experimentally by Rudko and Tang[67,23]. By comparing the total spontaneous emission intensity of transitions terminating on a 4p state with the total spontaneous emission intensity of transitions originating from that state, the relative pumping due to cascade from above may be determined. For example, 50% of the 4p $^2D_{5/2}$ state population appears to be due to cascade from above. Since the populations of the states (4d, etc.) from which cascade pumping takes place also exhibit a quadratic current dependence (see §A.3.9), the overall cascade pumping process is expected to lead to a quadratic current dependence for the 4p populations and thus cannot be distinguished from the other proposed excitation processes. The contribution of cascade from above to the pumping of various 4p states is summarized in table A.7.

Pumping processes from neutral argon metastable levels either directly to the 4p states (process II) or via metastable ion states (but not the ion ground state) have not been investigated theoretically. It has been suggested (Borisova et al 1967)[68] that the magnitude of the ion axial drift velocity implies that the ionic state must exist for at least 10^{-7} sec and that therefore the ion ground state must be involved in the excitation process. In view of the considerable uncertainty regarding ion axial drift velocities, this conclusion must be treated with some caution. Koozekanani[69] has compared direct excitation from neutral argon metastable states (process II) with direct excitation from the ion ground state (process III), and finds the ratio of the former to the latter to be

$$0.8 \times 10^{-2} \quad \frac{\langle \sigma_{mu}(E) v \rangle}{\langle \sigma_{iu}(E) v \rangle} \frac{N_m}{N_i} \quad ,$$

where N_m is the neutral argon metastable density, N_i the ion density, $\sigma_{mu}(E)$ the cross-section for removal of the metastable electron, and

σ_{iu} the cross-section for process III. The neutral metastable atom has a cross-section about a factor of 10 larger than that of the ion ground state. The total neutral metastable population under typical operating conditions has been shown to be of the order of 3×10^{12} cc^{-1}, whereas the ion ground state density is of the order of 3×10^{13} cc^{-1} (see A.3.5), and so the advantage of larger cross-section is offset by an adverse population ratio. Also, the energy gap involved in excitation from the neutral metastable states is significantly larger than that associated with excitation from the ion ground state, which means that even fewer of the high energy electrons can partake in the process. It would appear, therefore, that direct excitation from neutral metastables is not significant. This is borne out by the observed current dependence of the 4p populations - direct excitation from neutral metastable states implies a linear dependence of 4p population on current, since the metastable populations are saturated with respect to current.

The significance of the different excitation mechanisms introduced here is discussed fully in the context of chapter 5.

References (Appendix A)

1 Bridges W B 1964 Appl Phys Lett 4 128

2 Convert G, Armand M and Martinot-Lagarde P 1964 C R Acad Sci 258 4467-9

3 Bennett W R, Knutson J W, Mercer G N and Detch J L 1964 Appl Phys Lett 4 180-2

4 Gordon E I, Labuda E F and Bridges W B 1964 Appl Phys Lett 4 178-80

5 Bridges W B and Halstead A S 1966 IEEE J Quant Elec QE-2 84

6 Labuda E F, Gordon E I and Miller R C 1965 J Quant Elec QE-1 273

7 Paananen R 1966a Appl Phys Lett 9 34-5

8 Paananen R 1966b Appl Phys Lett 9 34-5

9 Rigden J D 1965 IEEE J Quant Elec QE-1 221

10 Hernqvist K G and Fendley J R Jr 1967 IEEE J Quant Elec QE-3 66

11 McMahan W H 1968 Appl Phys Lett 12 383

12 Boersch H, Herziger G, Seelig W and Volland I 1967 Phys Lett 24A 695-6

13 Banse K, Boersch H, Herziger G, Schafer G and Seelig W 1968a Phys Lett 28A 6-7

14 Sayers M D 1969 Phys Lett 29A 591-2

15 Boersch H, Boscher J, Hoder D and Schafer G 1970 Phys Lett 31A 188-9

16 Banse K, Herziger G, Schafer G and Seelig W 1968b Phys Lett 27A 682-3

17 Herziger G and Seelig W 1969 Z Physik 219 5-31

18 Goldsborough J P 1966 Appl Phys Lett 8 218

19 Goldsborough J P 1966 Appl Phys Lett 8 137

20 Minnhagen L 1963 Arkiv f Fysik 25 203

21 Statz H, Horrigan F A, Koozekanani S H, Tang C L and Koster G F 1965 'Transition probabilities for some Ar II laser lines' J Appl Phys 36 2278-86 see also Physics of Quantum Electronics 1966 ed Kelley P L et al 674-87

22 Garstang R H 1954 Monthly Notices Roy Astron Soc 114 118

23 Rudko R I and Tang C L 1967 J Appl Phys 38 4731-9

24 Koster G F, Statz H, Horrigan F A and Tang C L 1968 J Appl Phys 39 4045-6

25 Kitaeva V F, Osipov Yu I, Rubin P L and Sobolev N N 'On oscillation mechanisms in the CW Ion Argon Laser' private comm (May 1968)

26 Olsen H N 1963 J Quant Spectr Radiative Transfer 3 59

27 Bennett W R Jr, Kindlmann P J, Mercer G N and Sunderland J 1964 Appl Phys Lett 5 158-60

28 Kitaeva V F, Osipov Yu I and Sobolev N N 1966 IEEE J Quant Elec QE-2 635-7

29 Kitaeva V F, Osipov Yu I and Sobolev N N 1967 Sov Phys - Doklady 12 55-6

30 Kitaeva V F, Osipov Yu I, Sobolev N N and Rubin P L 1967 Sov Phys - Tech Phys 12 850-1

31 Kitaeva V F, Osipov Yu I and Sobolev N N 1966 Sov Phys - JETP Letters 4 146-8

32 Kitaeva V F, Osipov Yu I, Rubin P L and Sobolev N N 1968 Private Communications P N Lebedev Physical Institute Moscow

33 Chester A N 1968 Phys Rev 169 (1) 184

34 Caruso A and Cavaliere A 1964 Brit J Appl Phys 15 1021

35 Kagan Yu M and Perel V I 1958 Optika i Spectroskopiya 4 3 and 285

36 Kagan Yu M 1958 Izv Akad Nauk USSR Ser Phys (Bull of Acad of Sci of the USSR Phys Series) 22 699

37 Kolesnikov V N 1964 Trudy FIAN 30 66

38 Labuda E F, Webb C E, Miller R C and Gordon E I A Study of Capillary Discharges in Noble Gases at High Current Densities Bell Telephone Laboratories Private communication

39 Ballik E A, Bennett W R Jr and Mercer G N 1966 Appl Phys Lett 8 214

40 Pleasance L D and George E V 1971 Appl Phys Lett 18 557

41 Kitaeva V F, Odintsov A N and Sobolev N N 1970 Soviet Physics USPEKHI 99 699

42 Bennett W R Jr, Ballik E A and Mercer G N 1966 Phys Rev Lett 16 603-5

43 Bennett W R Jr Collision Processes in the Argon Ion Laser, The Physics of Electronic and Atomic Collisions, Fifth International Conference on 1967 AF-AFOSR 69-0036TR

Mercer G N, Chebotayev V P and Bennett W R Jr 1967 Appl Phys Lett 10 177-9

44 Bennett W R Jr, Ballik E A and Mercer G N 1966 Phys Rev Lett 16 603

45 Webb C E and Miller R C 1968, 1968 International Quantum Elec Conf paper 12L-6

46 Sze R C, Antropov Ye T and Bennett W R Jr 1972 Applied Optics 11 197-8

47 Miller R C, Labuda E F and Webb C E Excited Level Populations in High Current Density Argon Discharges Bell Syst Tech J 1967 281-4

48 Dunn M H and Ross J N 1973 Phys Lett 44A 247

49 Webb C E 1968 J Appl Phys 39 5441

50 Sze R C and Bennett W R Jr 1972 Phys Rev A5 837

51 Chester A N 1968 Phys Rev 169 (1) 172

52 Frost L S and Phelps A V 1964 Phys Rev A136 1538

53 Delcroix J L 1960 Introduction to the Theory of Ionized Gases, Interscience New York

54 Griem H R 1964 Plasma Spectroscopy McGraw-Hill New York p493

55 Koozekanani S H 1966 IEEE J Quant Elec QE-2 770

56 Bennett W R Jr, Mercer G N, Kindlmann P J, Wexler B and Hyman H 1966 Phys Rev Lett 17 987

57 Hammer J M and Wen C P 1967 J Chem Phys 46 1225

58 Feltsan P V and Povch M M 1970 Opt and Spectroscopy 28 119

59 Vainshtein L A and Vinogradov A V 1967 JETP Letters 5 269

60 Roberts D E 1966 Physics Letters 22 417

61 Roberts D E 1968 J Phys B1 53

62 Vladimirova N M, Konkov I D, Rovinskii R E and Cheburkin N V 1970 Sov Phys JETP 30 813

63 Vladimirova N M, Konkov I D, Rovinskii R E and Cheburkin N V 1971 Optics & Spectroscopy 31 91

64 Bleakney W 1930 Phys Rev 36 1303

65 Beigman I L, Vainshtein L A, Rubin P L and Sobolev N N 1967 JETP Letters 6 343

66 Brandi H S 1972 Phys Rev Lett 29 1539

67 Rudko R I and Tang C L 1966 Appl Phys Lett 9 41

68 Borisova M S, Ischenko Ye F, Ladygin M V, Molchashkin M A, Nasedkin Ye F and Ramazonova G S 1967 Radio Eng & Elec Phys 3 529

69 Koozekanani S H 1967 Appl Phys Lett 11 107

Wavelength in air (Å)		Designation
4371	(^{1}D)	4p $^2D^o_{3/2}$ - 3d $^2D_{3/2}$
4482		4p $^2D^o_{5/2}$ - 3d $^2D_{5/2}$
4545		4p $^2P^o_{3/2}$ - 4s $^2P_{3/2}$
4579		4p $^2S^o_{1/2}$ - 4s $^2P_{1/2}$
4727		4p $^2D^o_{3/2}$ - 4s $^2P_{3/2}$
4765		4p $^2P^o_{3/2}$ - 4s $^2P_{1/2}$
4880		4p $^2D^o_{5/2}$ - 4s $^2P_{3/2}$
4889		4p $^2P^o_{1/2}$ - 4s $^2P_{1/2}$
4965		4p $^2D^o_{3/2}$ - 4s $^2P_{1/2}$
5017	(^{1}D)	4p $^2F^o_{5/2}$ - 3d $^2D_{3/2}$
5142	(^{1}D)	4p $^2F^o_{7/2}$ - 3d $^2D_{5/2}$
5145		4p $^4D^o_{5/2}$ - 4s $^2P_{3/2}$
5287		4p $^4D^o_{3/2}$ - 4s $^2P_{1/2}$
1.09 μ		4p $^2P^o_{3/2}$ - 3d $^2D_{5/2}$

cw laser transitions in Ar II

(All levels have a ^{3}P core except where otherwise indicated)

Table A.1

Upper $(^3P)4p$ state	Lower $(^3P)4s$ state	A_{mn} x 10^{-6} sec^{-1}	For decay to all 3d states A x 10^{-6} sec^{-1}	Radiative Lifetime of 4p state x 10^9 sec	Population of 4p state x 10^{-9} cc^{-1}	% cascade pumping	Total Pumping rate to 4p state x 10^{-17} cc^{-1} s^{-1}
$^4P_{5/2}$	$^4P_{3/2}$	15		6	8	24%	14
	$^4P_{5/2}$	83	71				
$^4P_{3/2}$	$^4P_{1/2}$	22					
	$^4P_{3/2}$	15	34	6	6	19%	9
	$^4P_{5/2}$	61					
$^4P_{1/2}$	$^4P_{1/2}$	9.7	70	6	2	13%	3.5
	$^4P_{3/2}$	86.5					
$^4D_{7/2}$	$^4P_{5/2}$	135	20	6	7	31%	10
$^4D_{5/2}$	$^2P_{3/2}$	9.2					
	$^4P_{3/2}$	95	16	6 (7.5)	5	18%	7
	$^4P_{5/2}$	21					
$^4D_{3/2}$	$^2P_{1/2}$	2					
	$^4P_{1/2}$	62	18	6	3	19%	5
	$^4P_{3/2}$	63		(7.4)			
	$^4P_{5/2}$	2					
$^4D_{1/2}$	$^4P_{1/2}$	117	18	6	2	18%	2.5
	$^4P_{3/2}$	15					
$^2D_{5/2}$	$^2P_{3/2}$	85					
	$^4P_{3/2}$	13	4	9 (9.1)	5	27%	4
	$^4P_{5/2}$	4					
$^2D_{3/2}$	$^2P_{1/2}$	46					
	$^2P_{3/2}$	46	1	9 (9.8)	2	33%	2.0
	$^4P_{1/2}$	3					
	$^4P_{3/2}$	3					
	$^4P_{5/2}$	0.4					

4p	4s	A_{mn}	3d	Lifetime	Popn	Cascade	P
$^2P_{1/2}$	$^2P_{1/2}$	13	0.7	9 (8.7)	1	4%	0.6
	$^2P_{3/2}$	86					
$^2P_{3/2}$	$^2P_{1/2}$	45		9 (9.4)	3	14%	1.2
	$^2P_{3/2}$	52					
	$^4P_{3/2}$	0.7					
	$^4P_{5/2}$	0.9					
$^4S_{3/2}$	$^2P_{3/2}$	1	1	5	3	17%	5
	$^4P_{1/2}$	43					
	$^4P_{3/2}$	69					
	$^4P_{5/2}$	85					
$^2S_{1/2}$	$^2P_{1/2}$	90		7 (8.8)	1	4%	1.5
	$^2P_{3/2}$	23					

TABLE A.2. Columns 3 and 4: Transition probabilities for 4p to 4s and 4p to 3d transitions in Argon II.

Columns 5,6,7,8: Radiative lifetimes, populations and pumping rates for 4p states[21,23]. The lifetimes shown in brackets in column 5 are those measured by Bennett et al[27].

Upper (^{3}P) 4s State	Lower (^{3}P) 3p State	A_{mn} x 10^{-19} sec^{-1}	Radiative Lifetime of 4s state x 10^9sec
$^2P_{3/2}$	$^2P_{3/2}$	2.3	0.4
	$^2P_{1/2}$	0.4	
$^4P_{3/2}$	$^2P_{3/2}$	0.030	27
	$^2P_{1/2}$	0.006	
$^2P_{1/2}$	$^2P_{3/2}$	0.9	0.4
	$^2P_{1/2}$	1.8	
$^4P_{1/2}$	$^2P_{3/2}$	0.004	90
	$^2P_{1/2}$	0.007	

Table A.3 Transition probabilities and radiative lifetimes for (^{3}P) 4s states in Argon II[24]

Upper $(^3P)4d$ state	Radiative Lifetime $\times 10^4$ sec *	State & A coefficient for principal decay $\times 10^{-8}$ sec^{-1}	Population of 4d state $\times 10^{-8}$ cc^{-1}	Pumping Rate to 4d state $\times 10^{-17}$ cc^{-1} sec^{-1}
$^4D_{7/2}$	2.5	3 ($^4P_{5/2}$)	5	2
$^4D_{5/2}$	2.5	1.7($^4P_{3/2}$)	3.4	1.4
		1.6($^4P_{5/2}$)		
$^4D_{3/2}$	2.5	2.2($^4P_{3/2}$)	2.5	1
$^4D_{1/2}$	2.5	2.5($^4P_{1/2}$)	0.2	0.1
$^4F_{9/2}$	2.5	3.9($^4D_{7/2}$)	4.3	1.7
$^4F_{7/2}$	2.5	3.6($^4D_{5/2}$)	4.3	1.7
$^4F_{5/2}$	2.5	3.0($^4D_{3/2}$)	2.5	1
$^4F_{3/2}$	2.5	1.8($^4D_{1/2}$)	1.1	0.4
$^4P_{1/2}$	2.4	2.0($^4P_{3/2}$)	0.5	0.2
$^4P_{3/2}$	2.5	1.1($^4S_{3/2}$)	1.2	0.5
$^4P_{5/2}$	2.5	1.9($^4S_{3/2}$)	2.0	0.8
$^2F_{7/2}$	2.5	3.9($^2D_{5/2}$)	2.2	0.9
$^2F_{5/2}$	2.5	3.4($^2D_{3/2}$)	1.9	0.8
$^2P_{1/2}$	2.1	3.4($^2P_{1/2}$)	0.1	0.03
$^2P_{3/2}$	2.1	1.7($^2P_{3/2}$)	0.1	0.07
$^2D_{5/2}$	1.7	4.4($^2P_{3/2}$)	0.1	0.05
$^2D_{3/2}$	1.7	1.8($^2S_{1/2}$)	0.1	0.05

Table A.4 Lifetimes, transition probabilities, populations and pumping rates for the 4d states of Argon II[23].

(*Against decay to 4p states only)

Parameter		Source
Lifetimes	4p levels: 6-9 ns 4s quartet levels ($^4P_{3/2,1/2}$): 30-90 ns 4s doublet ($^2P_{3/2,1/2}$): 0.4 ns 4d levels: 2.5 ns	21,23, 24,27
Transition Probabilities	4p (doublet,quartet) → 4s (doublet, quartet):1 - 10 x $10^7 s^{-1}$ 4d → 4p: 1 - 4 x $10^8 s^{-1}$	21,23
	4s (quartet) → ion ground state: 4 - 30 x $10^6 s^{-1}$ 4s (doublet) → ion ground state: 2 x $10^9 s^{-1}$	24
Populations	4p level: 2 - 8 x $10^9 cc^{-1}$ (0.3 Torr,D = 2 mm, 160 A cm^{-2}) 4d level: 4 x $10^8 cc^{-1}$ (0.3 Torr, D = 2 mm, 160 A cm^{-2})	23
Gas Temperature (T_o)	2000 K (160 A cm^{-2}, D = 2 mm) Increases with increasing current Independent of pressure in range 0.1-0.6 Torr $T_o/300 = 1 + 0.02\ J\ (A\ cm^{-2})\ \{D(mm)\}^{\frac{1}{2}}$	29,39 33,38
Gas Density (N_o)	$N_o(cc^{-1}) = 10^{19}.p_o(Torr)/T_o(^oK)$ where p_o is filling pressure and T_o gas temp during operation	33,38
Ion/electron Density (N_e)	$N_e \sim 2.5 \times 10^{13} cc^{-1}$ (0.4 Torr, D = 1.6 mm, 200 A cm^{-2} $N_e(cc^{-1}) = K\ J\ (A\ cm^{-2})\ p_o\ (Torr)\ D(mm)$ where K = 1.6 x 10^{11} (Kitaeva et al) = 1.7 x 10^{11} (Gordon et al) = 2.7 x 10^{11} (Pleasance and George) = 2.0 x 10^{12} (Sze and Bennett)	29 33 29 38 40 50

Parameter		Source
Electron Drift Velocity (axial)	$v(\text{cm s}^{-1}) = 3.7/\{p_o(\text{Torr})\ D(\text{mm})\}$ (Gordon et al)	38
Atom/Ion Mean Free Paths (λ_o/λ_i)	$\lambda_o(\text{mm}) \sim \lambda_i(\text{mm}) \sim 0.05\ (T_o/300)/p_o(\text{Torr})$	33
Ion Temperature (along axis) (T_i)	$T_i \sim 1.5$ x (gas temperature) Similar dependence on discharge parameters	29
Electron Temperature (T_e)	Increases with decreasing pressure	31,35
	Current dependence uncertain	36,38,50
	$T_e \sim 3 \times 10^4\ ^oK$ (0.5 Torr, D = 2 mm, 160 A cm^{-2})	
Atom/Ion Drift Velocities	Discrepancies between investigators	
	Atom drift velocities:	
	Kitaeva et al: 7×10^3 cm s^{-1} (0.5 Torr, 160 A cm^{-2}, D = 2.8 mm)	30,41
	Bennett et al: undetectable	39
	Ion drift velocities (axial):	
	Bennett et al: 16×10^3 cm s^{-1} (0.5 Torr, 200 A cm^{-2}, D = 2 mm)	39
	Kitaeva et al: 16×10^3 cm s^{-1} (0.5 Torr, 200 A cm^{-2}, D = 1.6 mm)	30
	5×10^3 cm s^{-1} (0.5 Torr, 200 A cm^{-2}, D = 2.8 mm)	41

Parameter		Source
Populations Dependence on Discharge Parameters	Ar I (radiating): decreases slowly with increasing current	38
	Ar I (metastable): decreases slowly with increasing current ($1s^5$, $3.5 \times 10^{11} cc^{-1}$ for 0.45 Torr, 100 A cm^{-2}, D = 2.0 mm)	38
	Ar II (radiating) (4p,4d): quadratic function of discharge current at low pressures, cubic function at high pressures. Distribution of populations within a configuration is thermal. Show maxima in variation with pressure, peaking at 0.05-0.07 Torr (100 A cm^{-2}, D = 4 mm)	38,48
	Ar II (metastable): linear function of discharge current $3d\ ^4F_{9/2}$, $4.5 \times 10^{10} cc^{-1}$, for 200 A cm^{-2}, 0.45 Torr D = 2 mm)	38
Axial Electric Field	X (volts cm^{-1}) = 12.3/D(mm) Only weakly dependent on current and pressure	33
Debye Length	$\lambda_d(cm) = 7 \times 10^2\ T_e(eV)/\{N_e(cm^{-3})\}^{\frac{1}{2}}$	52
Electron Mean Free Path	electron-neutral: $\lambda_e(mm) \sim (3/p_o\ E_e)(T_o/300)$ where E_e is electron energy (eV)	51
	electron-ion: $\lambda_{e-i}(mm) \sim 2 \times 10^{14}\ E_e^2 / N_e$	52

Table A.5 Summary of discharge parameters

4p state	Threshold (eV)	E_{peak} (eV)	Q_{peak} x 10^{19} cm^2 {55}	{56}	{57}	{58}	Cascade* {57}
$^2S_{1/2}$	35.72	60	2.1	6.8	3.6	-	50%
$^2P_{1/2}$	35.55	97	8.1	14.1	5.5	3.6	0
$^2P_{3/2}$	35.62	97	7.8	24.6	13.5	10.2	25%
$^2D_{3/2}$	35.51	60	3.9	16.5	9.9	6.8	50%
$^2D_{5/2}$	35.42	60	0	15.0	8.3	11.5	30%
$^4D_{5/2}$	35.30	60	-	-	-	4.6	-

Table A.6 Maximum values of cross-sections for direct electron impact excitation of Ar II 4p states. {55} theoretical, no cascade, {56} - {58} experimental including cascade from above. * Estimate of cascade contribution to cross-section given by {57}.

State (^3P) core	(a) Pumping Rate (arbitrary units)	(b) % cascade pumping
$^4P_{5/2}$	1.7	24%
$^4P_{3/2}$	0.5	19%
$^4P_{1/2}$	0.7	13%
$^4D_{7/2}$	0	31%
$^4D_{5/2}$	1.8	18%
$^4D_{3/2}$	0.4	19%
$^4D_{1/2}$	0.3	18%
$^2D_{5/2}$	0.5	27%
$^2D_{3/2}$	0.2	33%
$^2P_{1/2}$	0.5	4%
$^2P_{3/2}$	0.1	15%
$^4S_{3/2}$	1.0	17%
$^2S_{1/2}$	0.3	4%

Table A.7

(a) Relative pumping rates ($\langle \sigma(E) \quad v \rangle$) for 4p levels by process III (Brandi[66])

(b) Percentage cascade pumping in 2 mm bore tube, filling pressure 0.3 Torr, current 5 A (Rudko and Tang[23])

p_o Torr	j A/cm²	T_e, 10^4 K; N_e, 10^{13} cm^{-3}	Pumping rate, 10^{17}cm^{-3} sec^{-1}				Total pumping rate 10^{17}cm^{-3} sec^{-1}		Population of configuration 10^9 cm^{-3}		Population of doublet system per USW, 10^8 cm^{-3}		Inversion per USW, 10^8 cm^{-3}
			3p→4s	3p→4p	3p→4d→4p	3p→3d→4p	4p	4s	4p	4s	4p	4s	
0.21	160	T_e = 5.6 N_e = 2.9	1.7	2.4	0.14	0.02	2.6	4.3	2.0	0.12	1.1	0.2	0.9
	330	T_e = 9.2 N_e = 2.9	7	10.8	0.91	0.06	11.8	18.8	8.3	0.66	4.6	1.1	3.5
0.37	160	T_e = 5.2 N_e = 5.4	5.2	5.8	0.36	0.29	6.5	11.7	4.7	0.42	2.6	0.7	1.9
	330	T_e = 9.0 N_e = 5.2	23	31.6	2.7	0.90	35.2	58.2	25.6	2.0	14.2	3.3	10.9
0.62	160	T_e = 3.2 N_e = 14.4	4.6	4.0	0.10	3.06	7.1	11.8	2.9	1.6	1.6	2.6	-1.0
	330	T_e = 6.5 N_e = 14	61	99.6	6.2	35	141	202	80.3	15.4	44.6	25.6	19.0

Table A.8 Pumping rates and populations for the 4s and 4p configurations as a function of discharge parameters. 2 mm bore. (Kitaeva et al[41])

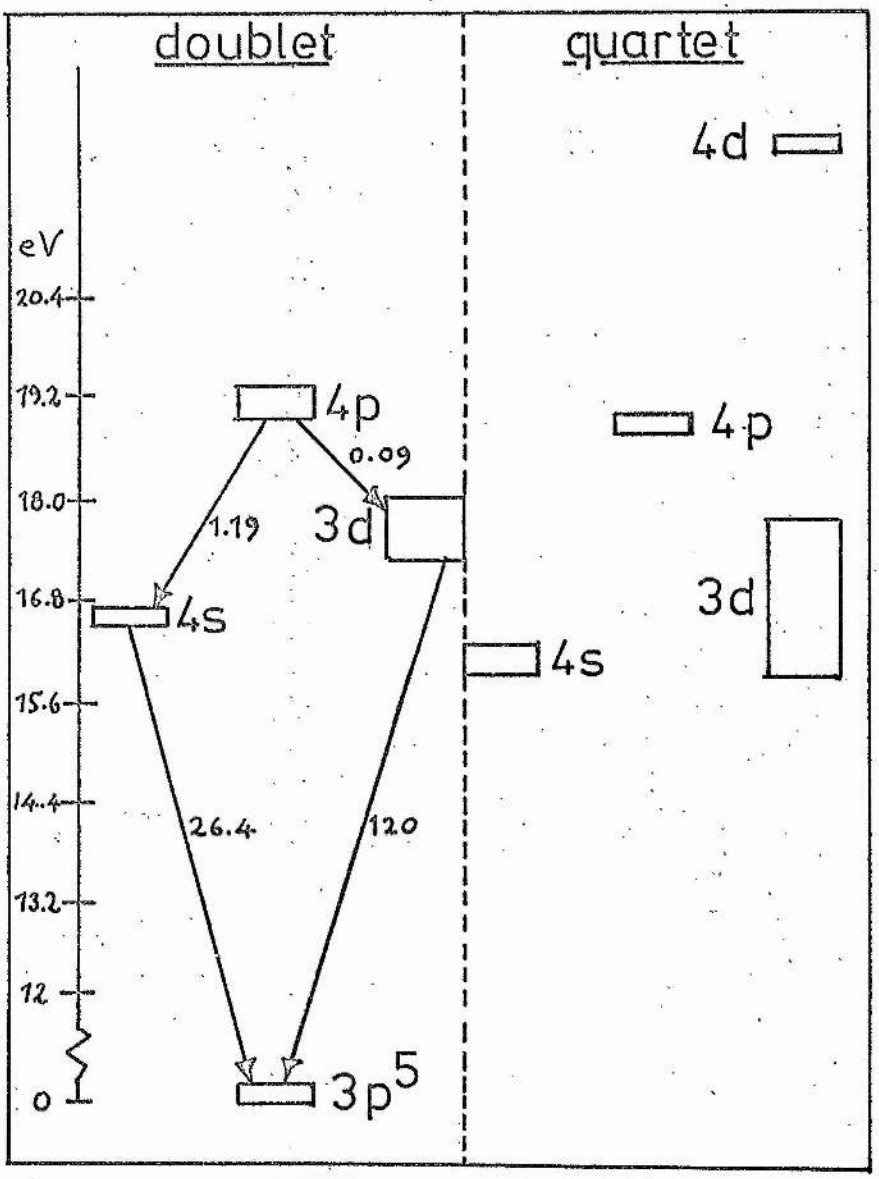

Figure A.1. Configurations in Argon II. All have the ^3P as parent term. The vertical extension of each block indicates the energy range associated with levels of the configuration. The numbers at the arrows designate the radiative transition probabilities ($\Delta S = 0$) in units of 10^8 s^{-1}.

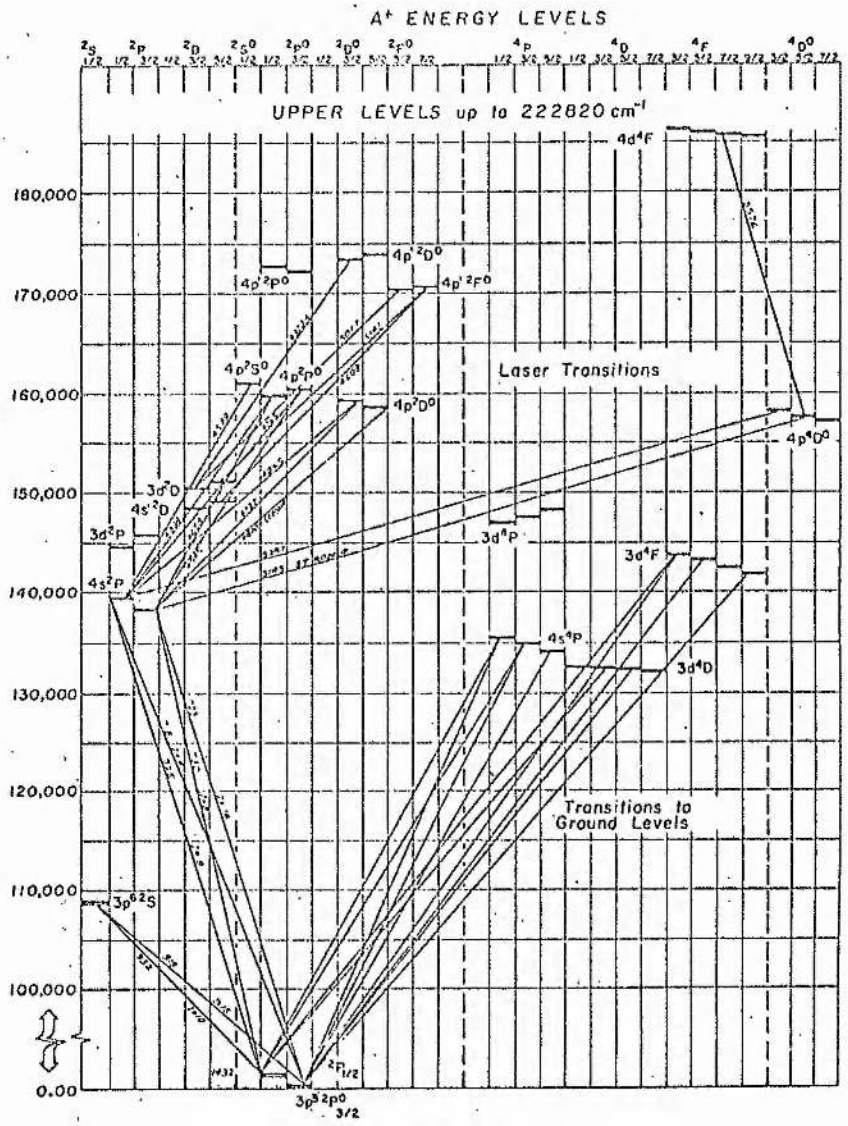

Argon Ion Laser Transitions

Figure A.2 Energy levels of Argon II.

A.3

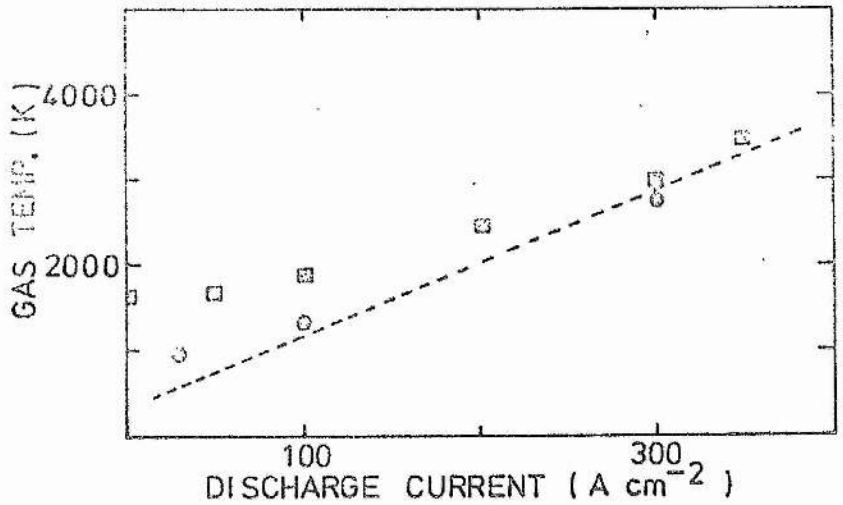

A.4

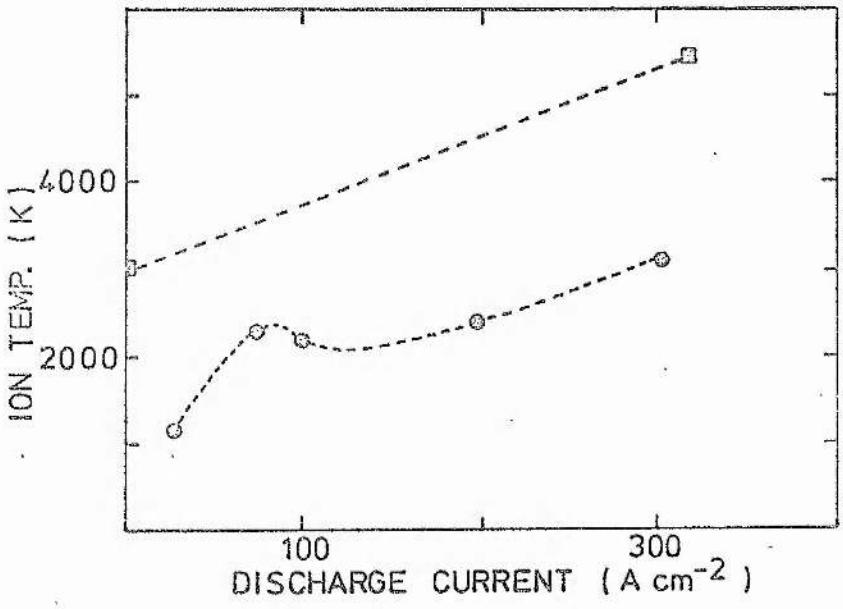

Figure A.3 Gas temperature (K) as a function of discharge current (A cm^{-2}). ▣ Kitaeva et al[29] (0.1 - 0.37 Torr, 1.6 mm bore), ◉ Bennett et al [39,50] (0.2 - 1.5 Torr, 2 mm bore), ---- Chester's empirical formula[33] (2 mm bore).

Figure A.4 Ion temperature (K) as a function of discharge current (A cm^{-2}). ▣ Kitaeva et al[29] (0.1 - 0.37 Torr, 1.6 mm bore), ◉ Bennett et al[39,50] (0.2 - 1.5 Torr, 2 mm bore).

A.5

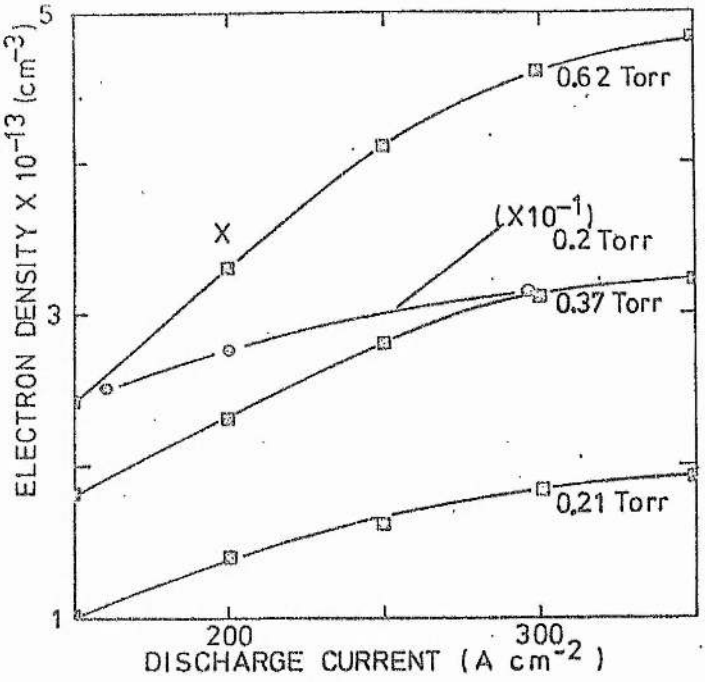

A.6

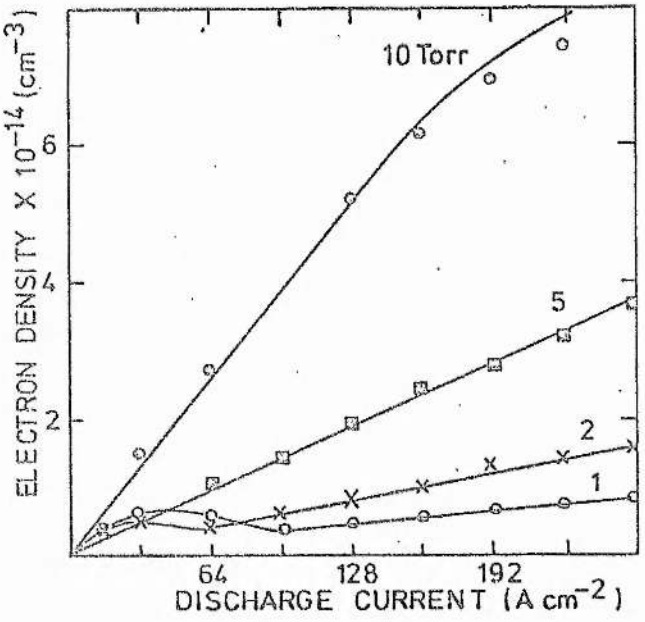

Figure A.5 Electron density (cm^{-3}) as a function of discharge current (A cm^{-2}). ⊙ Sze and Bennett[50] (0.2 Torr, 2 mm bore), ▩ Kitaeva et al[29,37] as deduced from electron temperature measurements (1.6 mm bore), × Kitaeva et al[29] as deduced from Stark broadening (0.4 Torr, 1.6 mm bore).

Figure A.6 Electron density as a function of discharge current, Labuda et al[38]. ⊙ 10 Torr, ▩ 5 Torr, × 2 Torr, o 1 Torr (2 mm bore).

A.7

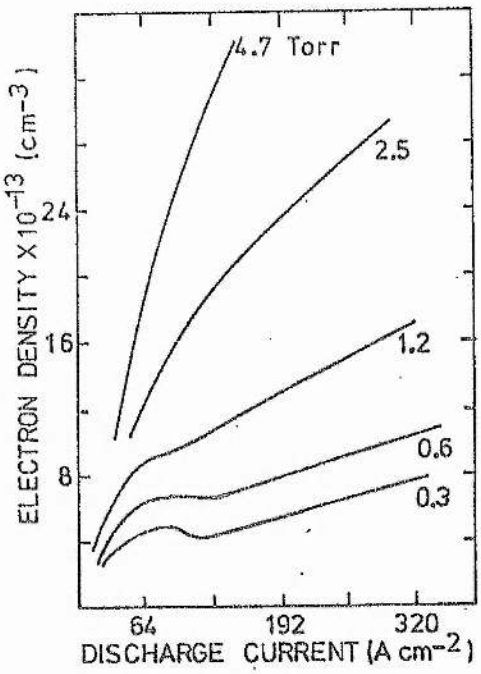

A,8

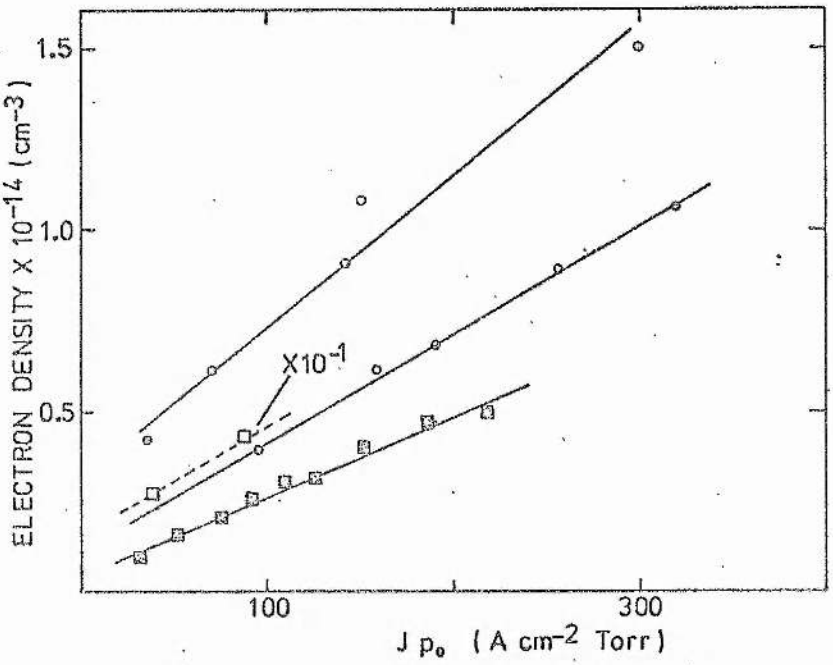

Figure A.7 Electron density (cm^{-3}) as a function of discharge current (A cm^{-2}). Pleasance and George[40] (2mm bore).

Figure A.8 Electron density (cm^{-3}) as a function of J p_o (A cm^{-2} Torr). o Labuda et al[38] (2 mm bore), ⊙ Pleasance and George[40] (2 mm bore), ▣ Kitaeva et al[29,37] (1.6 mm bore), □ Sze and Bennett[50] (2 mm bore).

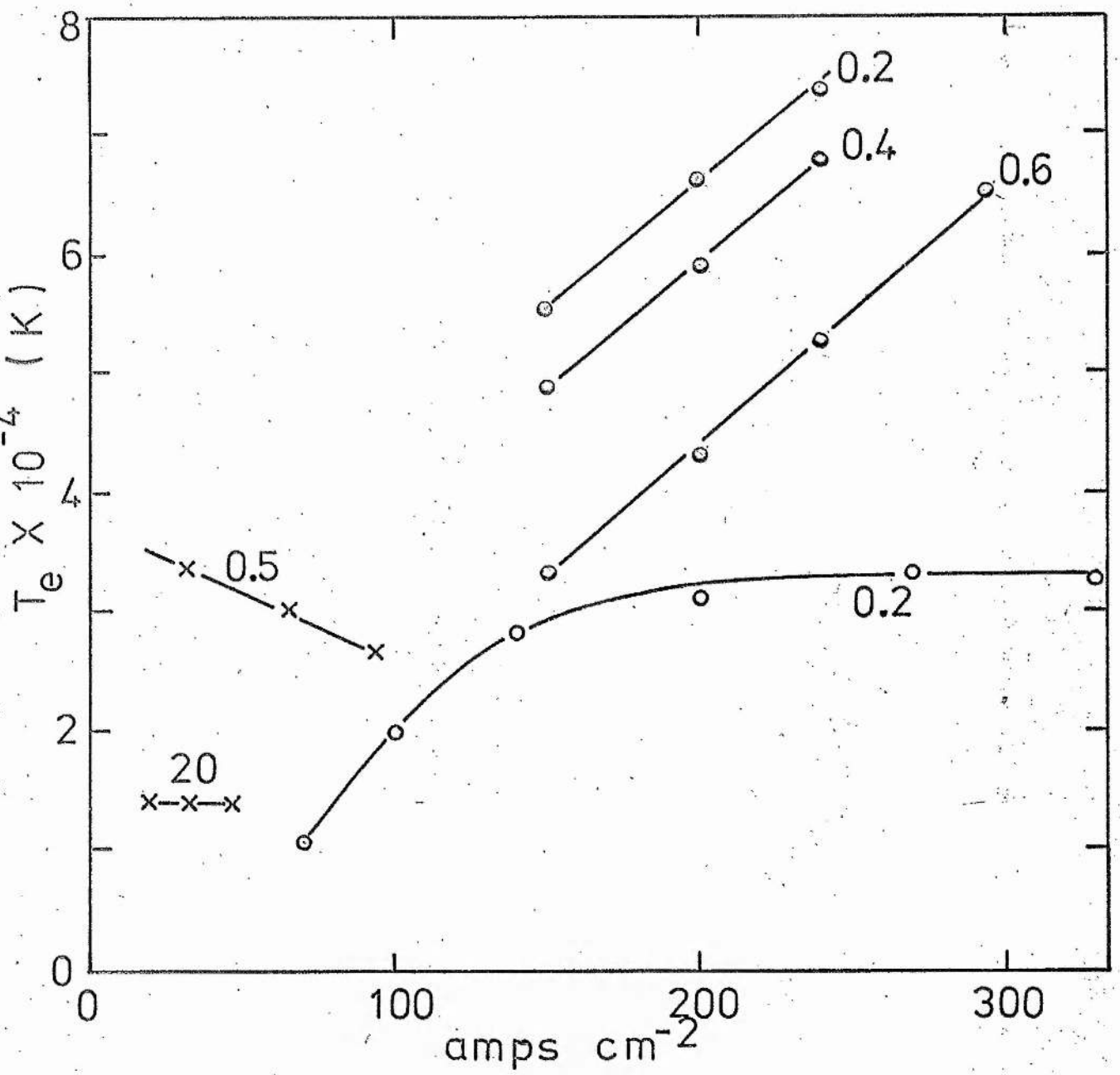

Figure A.9 Electron temperature (K) as a function of discharge current (A cm^{-2}) with pressure as parameter.(Torr).

X Labuda et al. [38] (2 mm bore)

O Sze and Bennett [50] (2 mm bore)

⊙ Kitaeva et al. [29, 31] (1.6 mm bore)

A.10

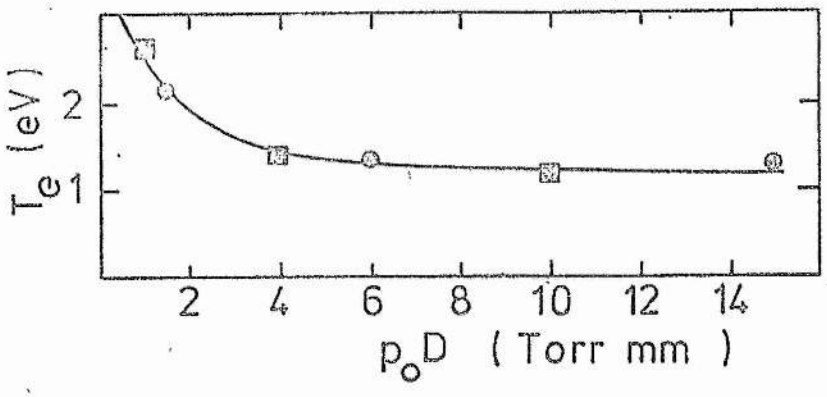

A.11

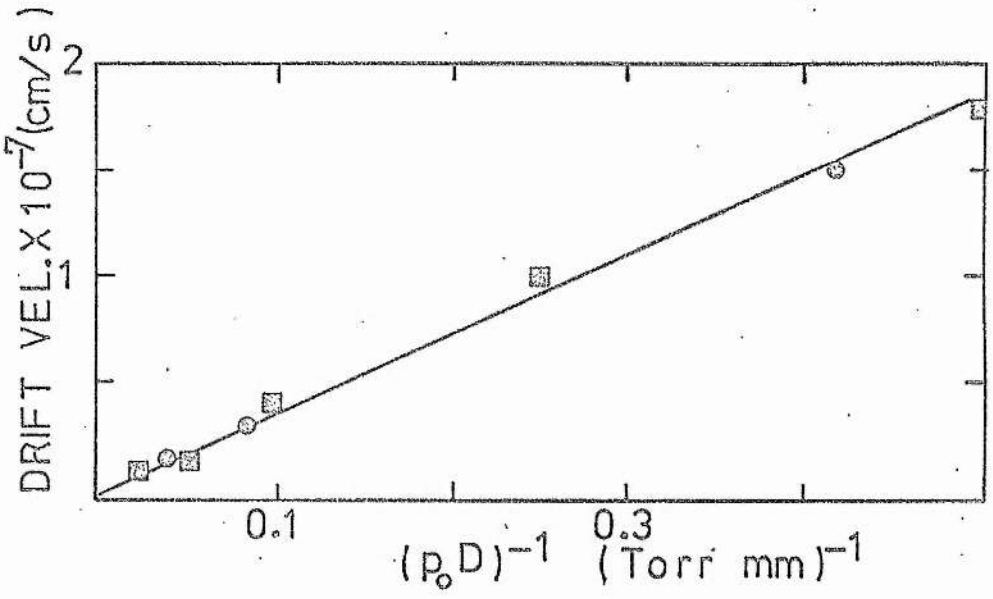

Figure A.10 Electron temperature (T_e, eV) as a function of the product of discharge tube filling pressure (p_o, Torr) with tube bore (D, mm) at constant current. ▩ 2 mm bore, o 3 mm bore. Labuda et al.[38]

Figure A.11 Axial draft velocity (cm/s) of electrons as a function of the inverse of the filling pressure (p_o, Torr) tube bore (D, mm) product. ▩ 2 mm bore, o 1.2 mm bore. Labuda et al.[38]

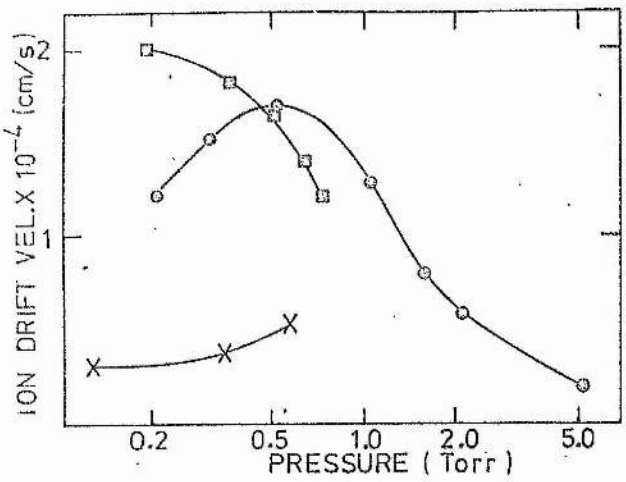

A.12

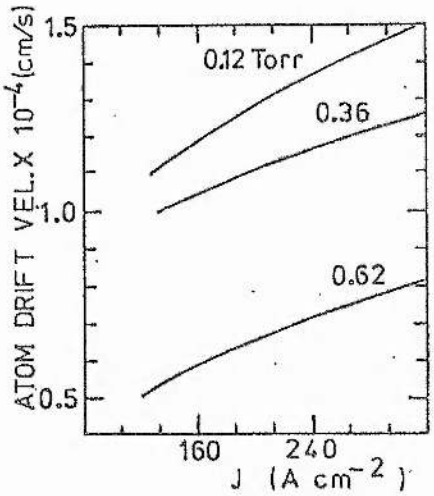

A.13

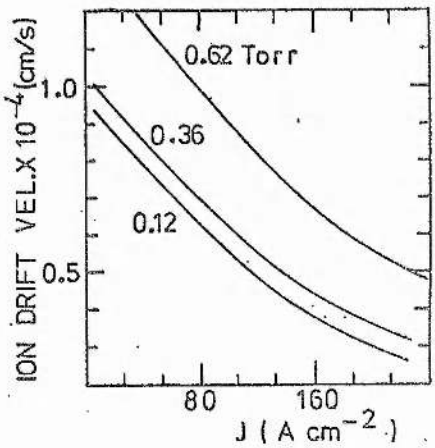

A.14

Figure A.12 Axial drift velocity of atoms (cm s^{-1}) as a function of current density (J, A cm^{-2}). 2.8 mm bore. Kitaeva et al.[30,41]

Figure A.13 Axial drift velocity of ions (cm s^{-1}) as function of current density (J, A cm^{-2}). 2.8 mm bore. Kitaeva et al.[41]

Figure A.14 Comparison of ion drift velocity (cm s^{-1}) measurements by various investigators. ⊙ Ballik et al[39] (2 mm bore, (200 A cm^{-2}), ⊠ Kitaeva et al[30] (1.6 mm bore, 200 A cm^{-2}), × Kitaeva et al[41] (2.8 mm bore, 200 A cm^{-2}).

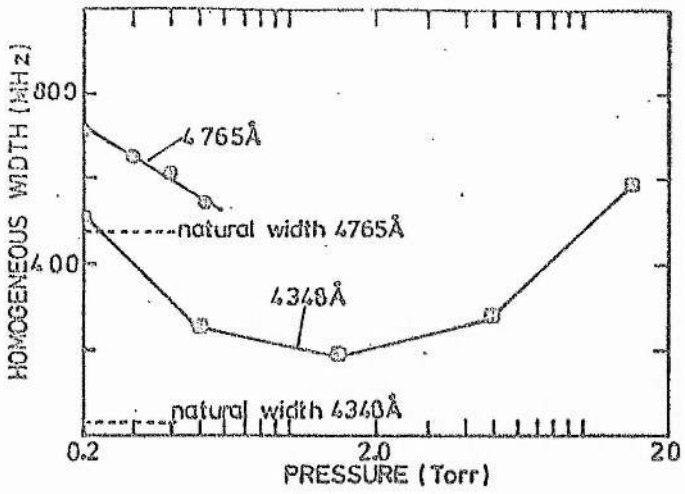

A.15

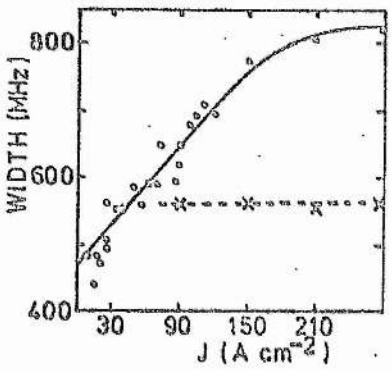

A.16

A.17

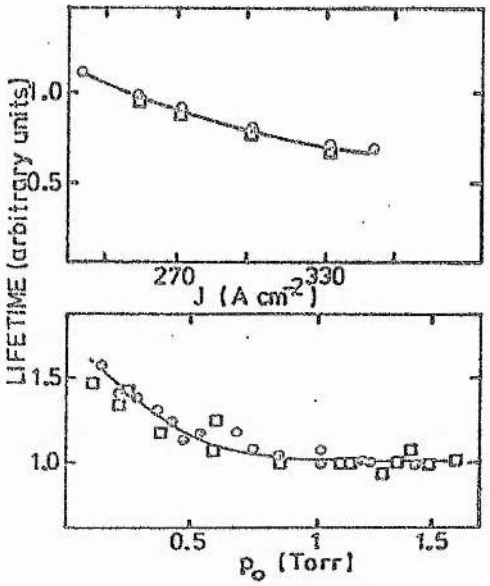

Figure A.15 Homogeneous linewidths at 4765Å (o, Bennett[44], 2 mm bore) and 4348Å (▫ Webb and Miller[45], 3 mm bore). Current density approximately 150 A cm^{-2}.

Figure A.16 Variation of homogeneous width (MHz) of 4765Å line with discharge current (A cm^{-2}). o — o 0.2 Torr 2 mm bore, × -- × 0.5 Torr 2 mm bore. (Bennett et al[46]).

Figure A.17 Depen dence of level lifetime (arbitrary units) on (a) discharge current (A cm^{-2}) at constant pressure 0.7 Torr, and (b) pressure (Torr) at constant current 10 A. 2 mm bore. ▫ 4p $^2D_{5/2}$, o 4p $^4D_{5/2}$. (Vainshtein and Vinogradov[59]).

A.18

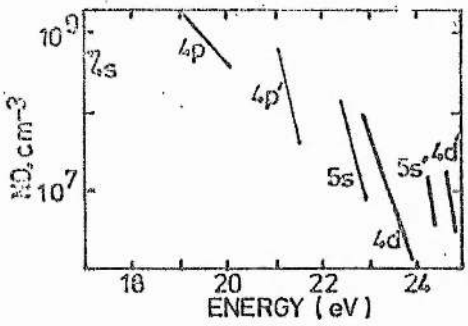

A.21

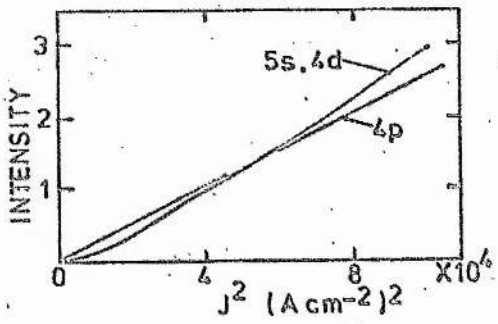

A.19

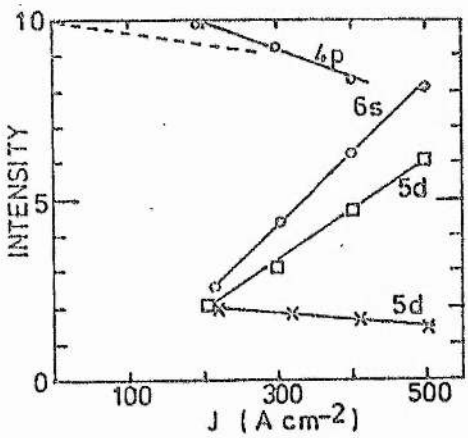

A.22

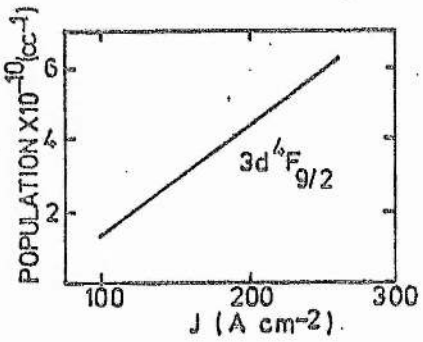

A.20

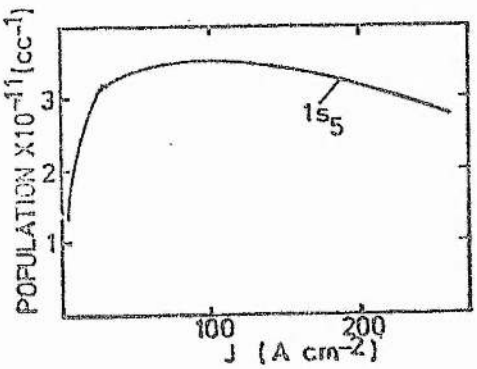

Figure A.18 Population per unit statistical weight per unit volume (cm^{-3}) of levels in various ArII configurations as a function of energy (eV) above ion ground state. (Rudko and Tang[26]).

Figure A.19 Populations of ArI radiative transitions as a function of discharge current (A cm^{-2}). × 5d (6719Å), □ 5d (6827Å), ⊙ 6s (7206Å), o 4p. Filling pressure 0.7 Torr, 2.5 mm bore. (Vladimirova et al[63]). The dashed line refers to measurements made by Labuda et al[40].

Figure A.20 Population of the $1s_5$ level of ArI (cc^{-1}) as a function of discharge current (A cm^{-2}). Filling pressure 0.45 Torr, 2 mm bore. (Labuda et al[40]).

Figure A.21 Populations of 5s, 4d, 4p levels of ArII (arbitrary units) as a function of the square of discharge current (A^2 cc^{-2}). Filling pressure 0.45 Torr, tube bore 2 mm. (Labuda et al[40]).

Figure A.22 Population of 3d $^4F_{9/2}$ level of ArII (cc^{-1}) as a function of discharge current (A cm^{-2}). Filling pressure 0.45 Torr, tube bore 2 mm. (Labuda et al[40]).

A.23

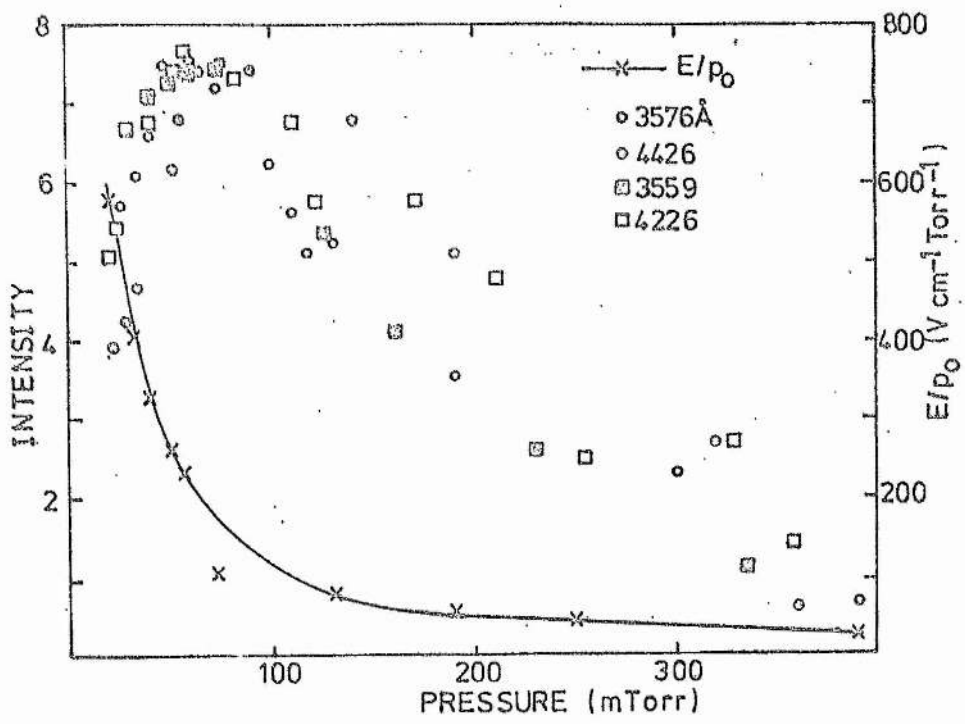

A.24

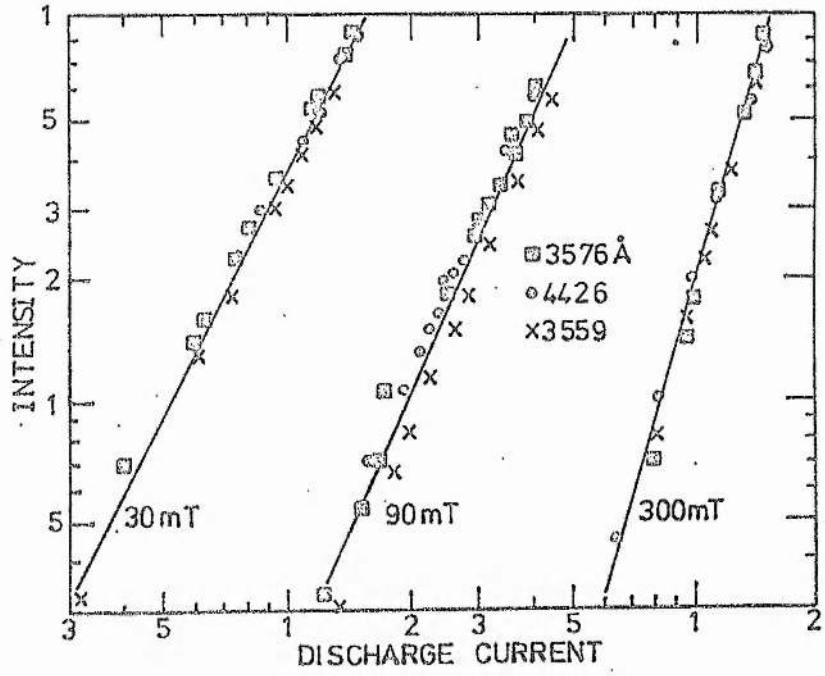

Figure A.23 Populations of various 4p levels of ArII (arbitrary units) as a function of filling pressure (m Torr), and E/p_o (V cm^{-1} Torr^{-1}) value as a function of filling pressure. Discharge current 10 A in a 4 mm bore tube.

Figure A.24 Intensity variations of three ArII lines with discharge current over a range of approximately 3 - 15 A for each pressure, in a 4 mm bore tube.

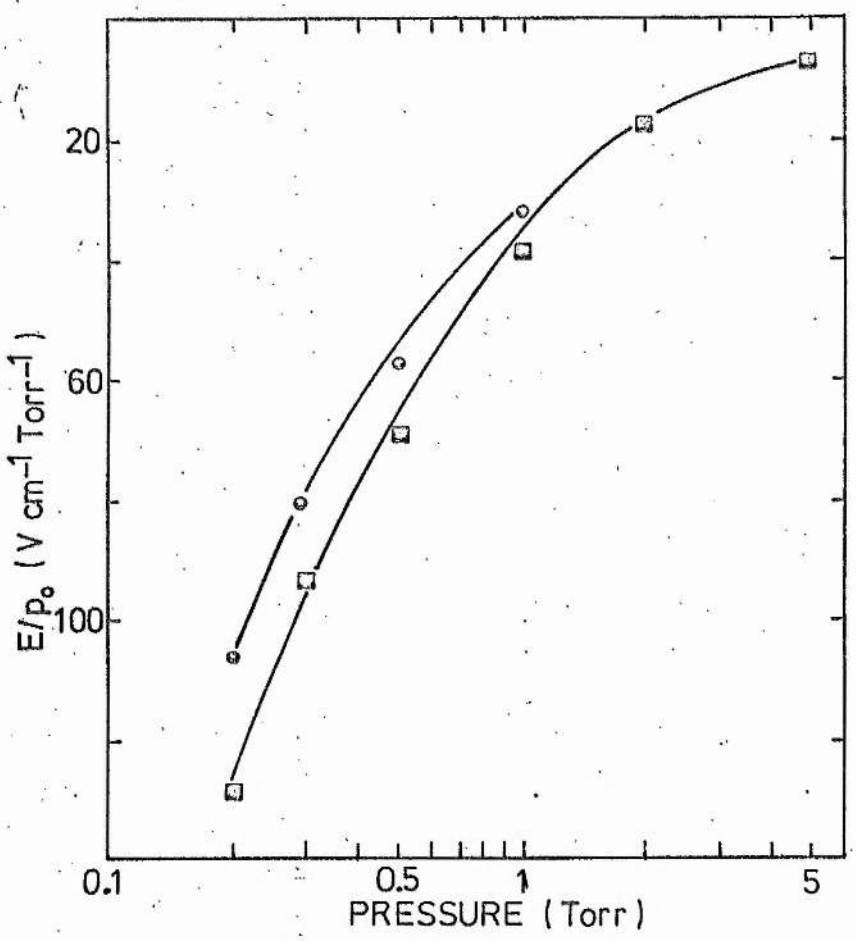

Figure A.25 Variation of E/p_o (volts cm^{-1} $Torr^{-1}$) with pressure (Torr). ○ at 5 Amps, ▣ at 7 Amps. Tube bore 2 mm. Ballik et al. [39]

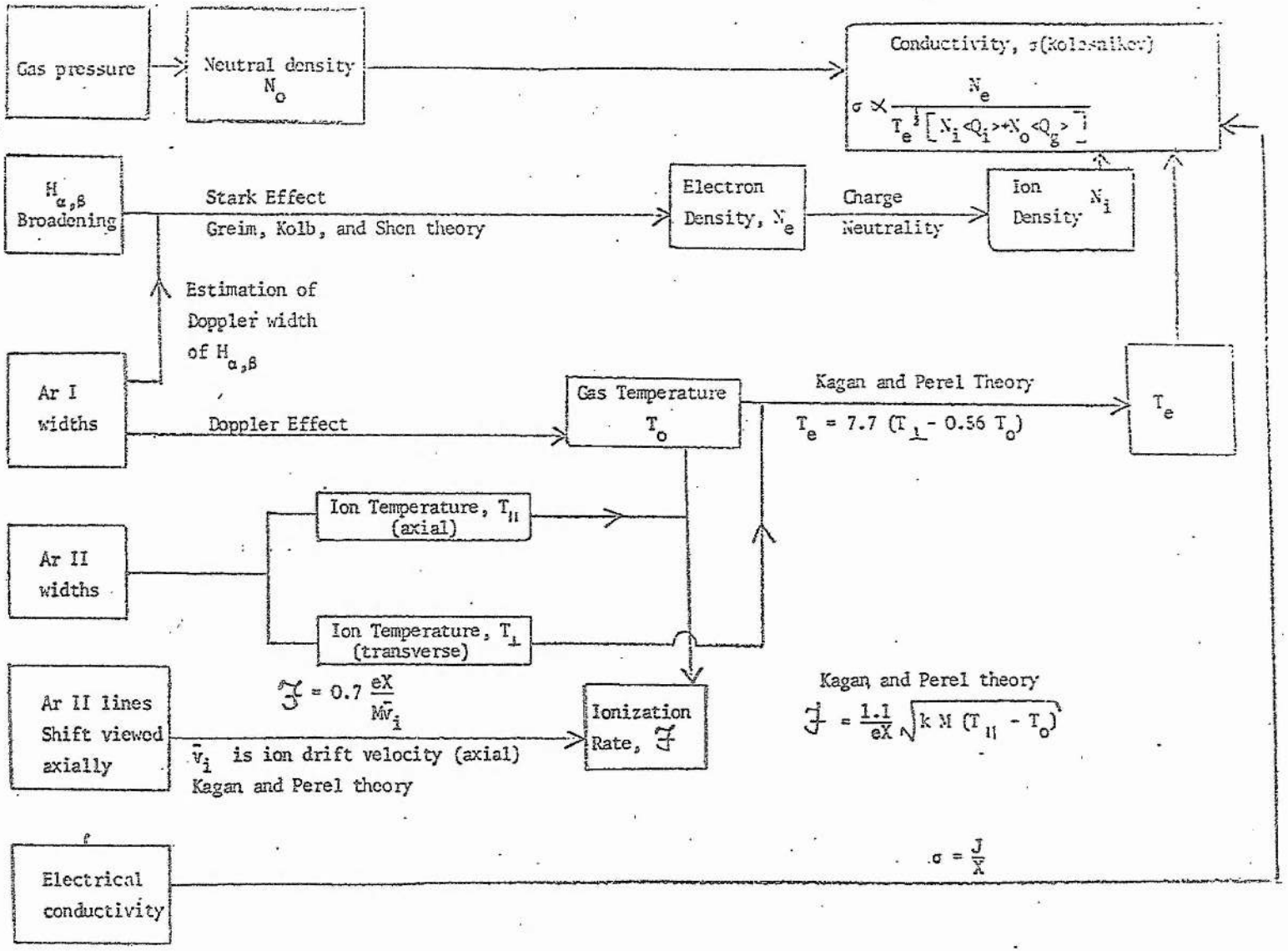

Fig. A.26. Approach of Kitaeva et al to argon ion laser diagnostics

Fig A.27. Approach of Bennett et al to argon ion laser diagnostics.

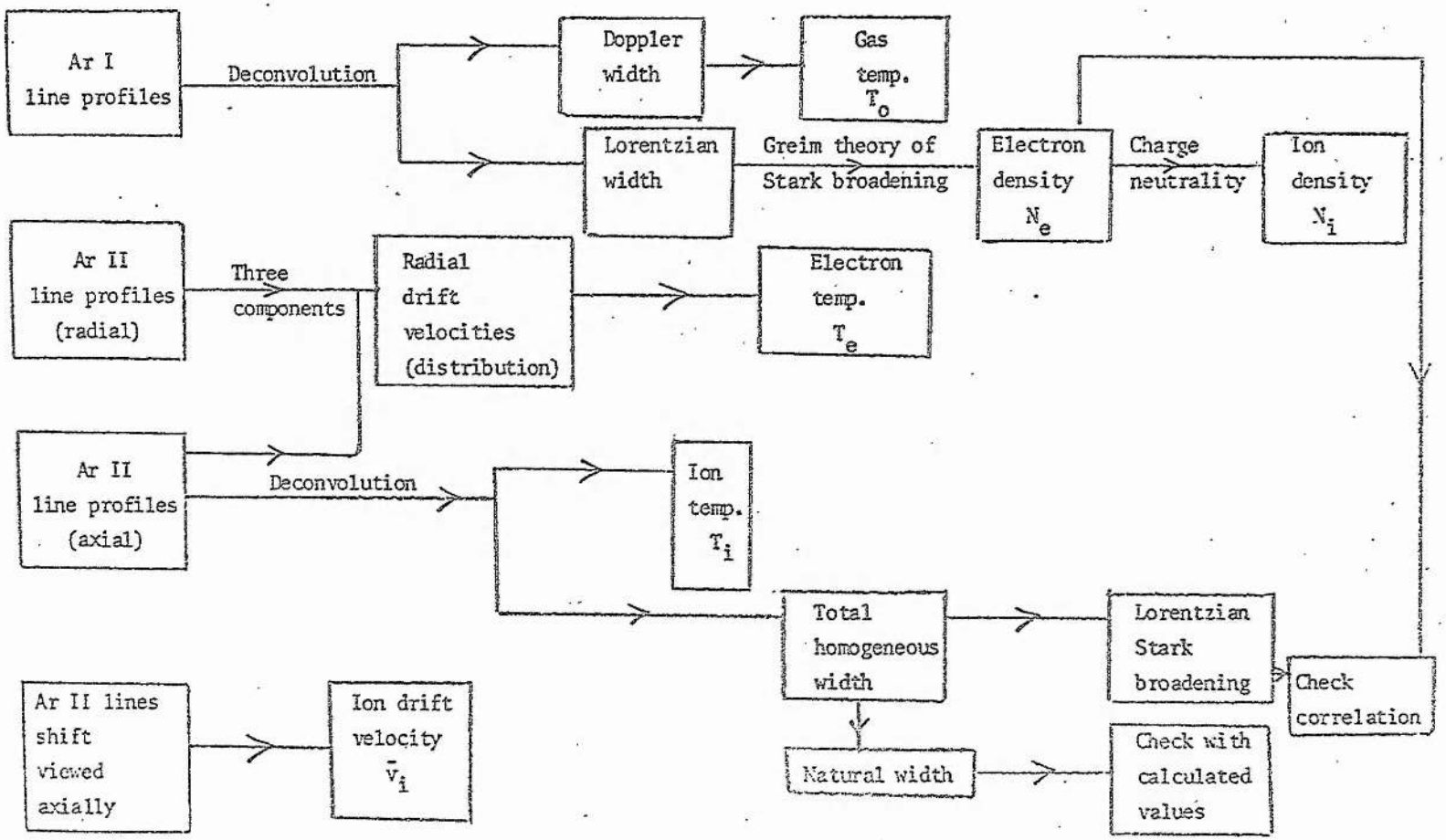

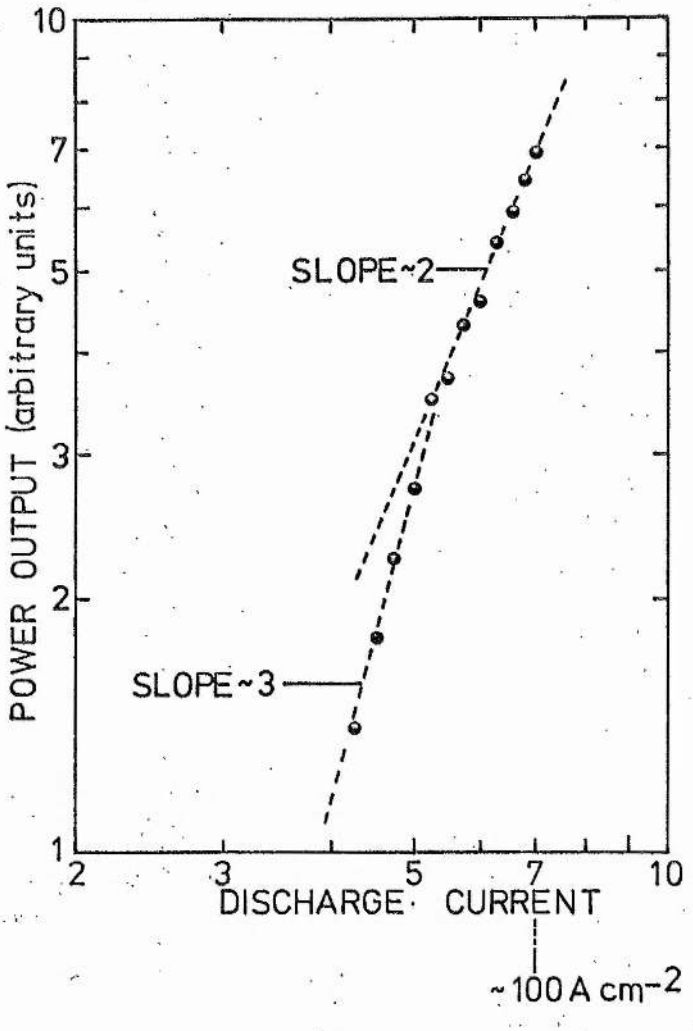

Figure A.28 Laser power output as a function of discharge current (filling pressure 0.1 Torr, bore 3 mm.)

A.29

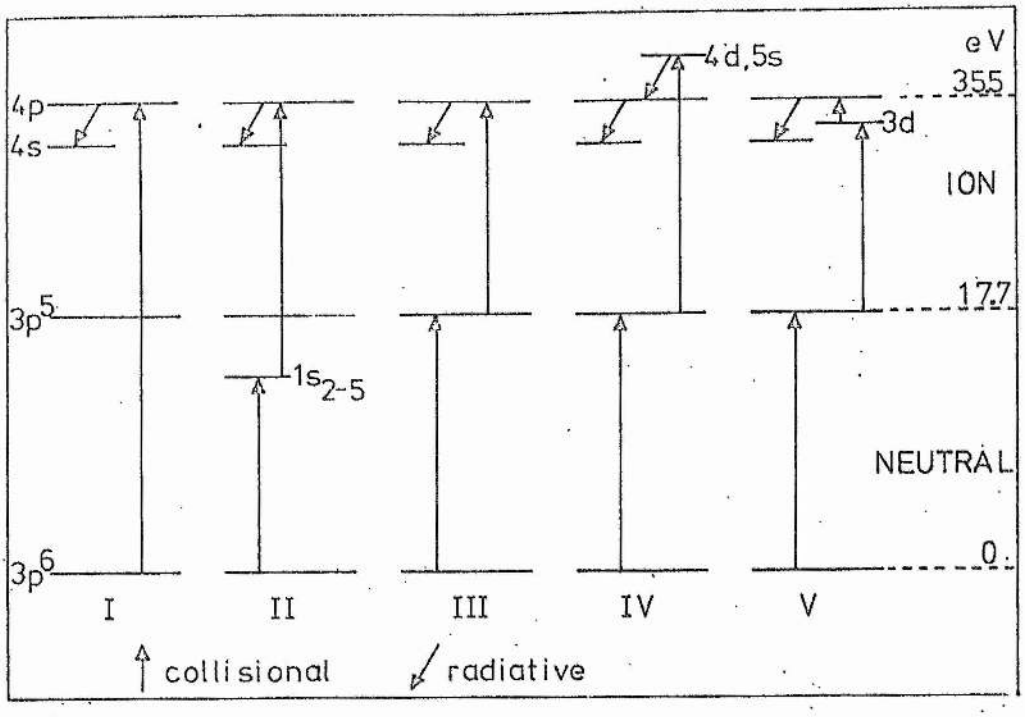

A.30

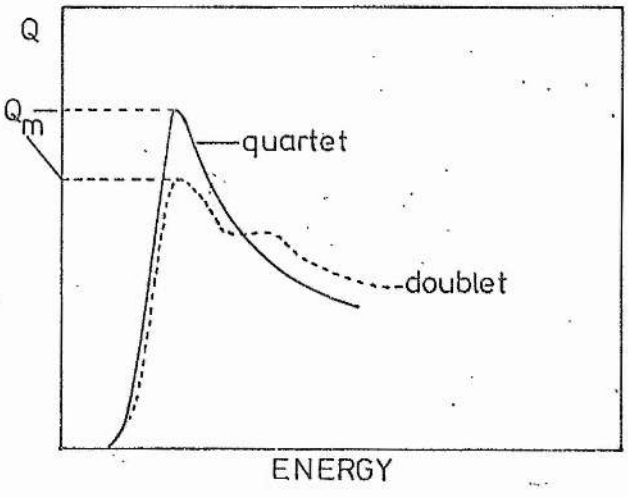

Figure A.29 Excitation pathways for 4p states of ArII.

Figure A.30 The variation with electron energy of the excitation cross-section (Q) for quartet 4p states and doublet 4p states of ArII.[58]

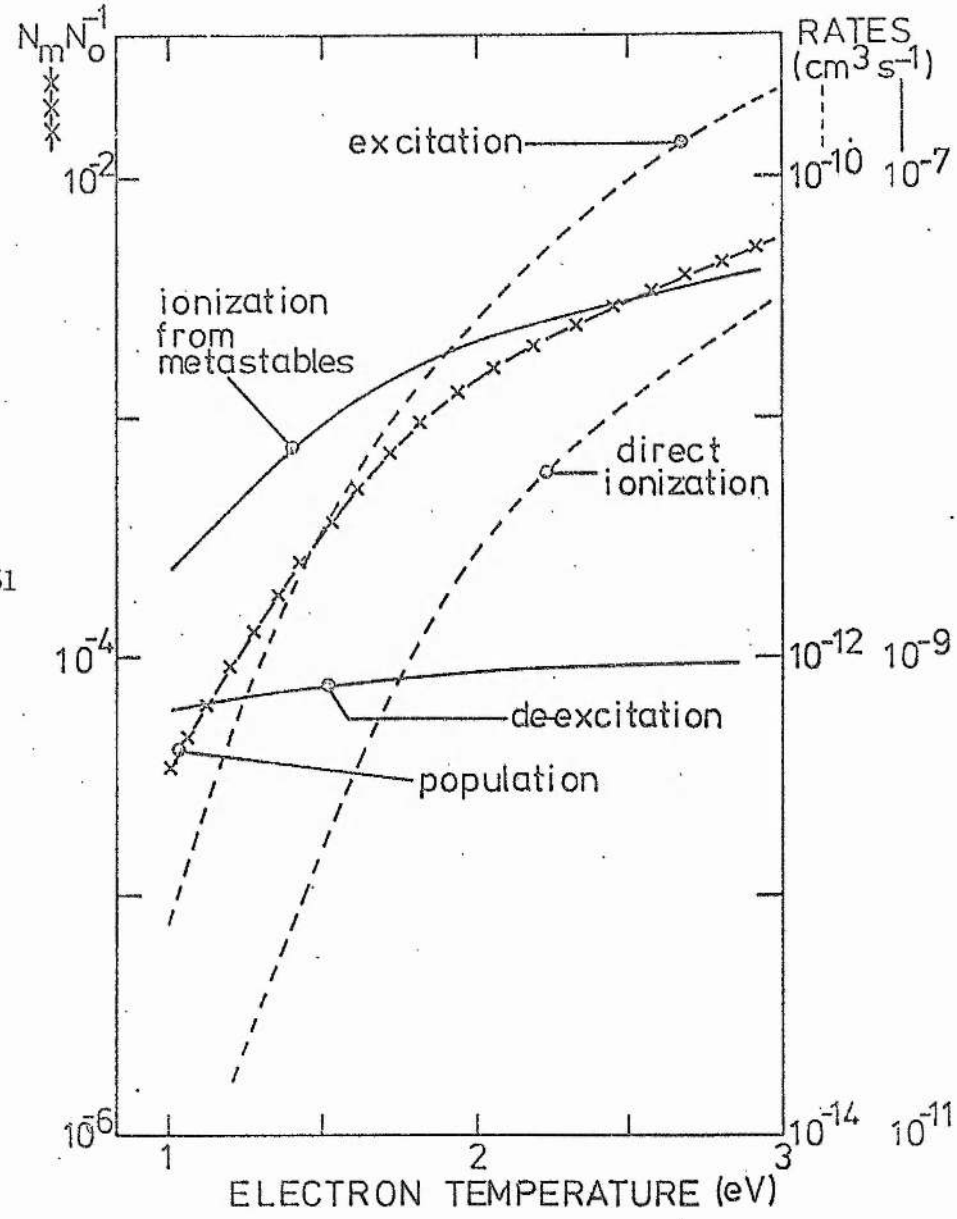

A.31

Figure A.31 The variation with electron temperature (T_e) of (a) the excitation rate ($cm^3\ s^{-1}$) to the $1s_{2-5}$ states of ArI, (b) the ionization rate ($cm^3\ s^{-1}$) from the ArI ground state, (c) the ionization rate ($cm^3\ s^{-1}$) from the $1s_{2-5}$ states, (d) the de-excitation rate ($cm^3\ s^{-1}$) from the $1s_{2-5}$ states to the ground state, and (e) the fractional population of the $1s_{2-5}$ states. The excitation rate is for all the $1s_{2-5}$ states, whereas the de-excitation rate and ionization rate refer to only one of the states. The population is therefore the total population of all the $1s_{2-5}$ states. (After Webb).

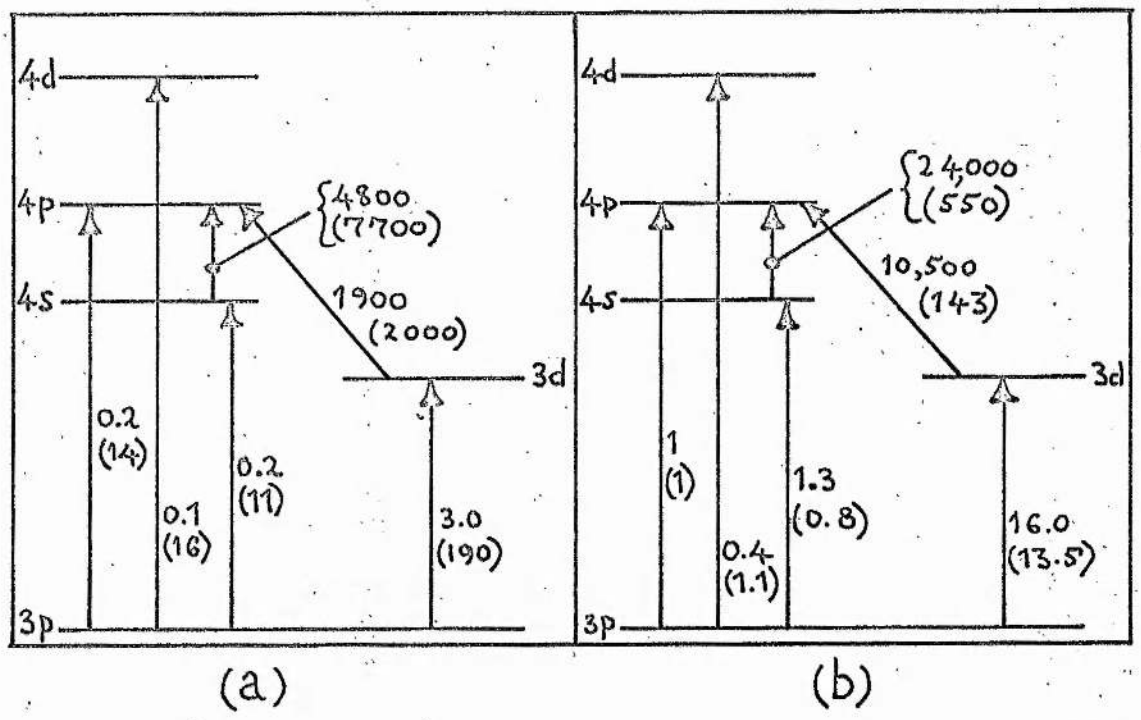

Figure A. 32. Excitation rates ($\langle v_e \sigma \rangle$) between various configurations in Argon II. (a) The numbers give the excitation rates in units of 10^{-10} cm^3 s^{-1}; the unbracketed numbers refer to an electron temperature of 30,000K and those in brackets to an electron temperature of 80,000K. Beigman et al.[65] (b) As in (a) but normalized on the 3p - 4p transition.

APPENDIX B

FLOW GRAPH TECHNIQUES

B.1 Introduction

Flow graph techniques are widely used in the analysis of electrical microwave circuits (eg Mason, 1953[1]; Hunton, 1960[2]; Robichaud et al, 1962[3]; Kuhn, 1963[4]; Adam, 1969[5]). Here we show how they can also provide a convenient method for describing excitation and decay processes between energy levels in complex systems, such as gas discharges. Under these circumstances, solution of the flow graph enables populations to be determined in terms of the coupling processes between levels. The flow graph technique is particularly convenient in this context since it allows the population of a particular level in a multi-level system to be calculated directly rather than by the elimination of unwanted populations from a set of coupled rate equations. Also, changes in populations brought about by the variation of a particular excitation or decay mechanism can readily be calculated. The clear display which the method gives for the various processes which determine the population of an energy level enables the magnitude of a given contribution to be assessed readily and the solution to be approximated to the required order as the analysis proceeds.

We first describe the construction of flow graphs to represent the population dynamics of multi-level systems and then summarize the well known topographical and analytical methods for the solution of the resulting flow graphs showing how they yield, in this case, the level populations required.

B.2 Construction of the Flow Graph

Each energy level is represented by a node in the flow graph of the system. A particular coupling process between a pair of energy levels is represented by a branch in the flow graph connecting the corresponding nodes. Pumping (or decay) processes to the level

system from levels not explicitly considered are represented by open ended branches terminating (or originating) on the appropriate nodes.

Consider the simple two level system illustrated in fig. B.1a. The two levels are pumped from unspecified sources at rates R_1 and R_2 as shown. The upper level (1) can either decay to the lower level (2), or to unspecified levels outside the system, with probabilities f_{12} and f_{10}, respectively. These probabilities are coefficients called branching ratios. The lower level decays only to unspecified levels outside the system, and so the value of f_{20} is unity. The flow graph of this simple system is illustrated in fig. B.1b. The pumping processes are represented by the open ended branches of value R_1 and R_2 terminating on the nodes 1 and 2 which represent the respective levels. The coupling process between the two levels is represented by the branch from node 1 to node 2 of value f_{12}. Finally the decay processes to levels outside the system are represented by open ended branches of value f_{10} and f_{20}, from the appropriate nodes.

An open ended branch represents an external source (pumping process) or sink. The value to be given to an open ended branch entering at a node of the flow graph system is that of a rate. A branch between nodes is given the value of a branching ratio. An open ended branch leaving the system at a node is also given the value of a branching ratio according to the process it represents.

Once the flow graph has been constructed it must be manipulated into a form suitable for calculating the population of interest. To do this, the total pumping rate into the level is determined by evaluating the various paths in the flow graph which connect the level to the external pumping processes. The product of the total pumping rate with the level lifetime then gives the population of the level. Either topographical or analytical techniques may be used in the manipulation of the flow graph. The topographical method is better

for retaining a physical picture of the process but is longer than the analytical method. The topographical method will be described first and will then be used to solve the simple flow graph in fig. B.1b.

B.3 Topographical Method of Solution

The use of topographical methods for the solution of flow graphs has been discussed by Kuhn, 1963[4]. A flow graph consists of a network of branches and nodes. The value to be assigned to a branch is that of a pumping rate or a branching ratio. For the purposes of describing the rules for solving flow graphs, we shall use the term 'coefficient' to mean pumping rate or branching ratio. There are four basic rules for solving flow graphs.

Rule 1 A node which has only one branch entering it and one branch leaving it, may be eliminated by replacing the two branches with a single branch whose coefficient is the product of the coefficients of the original two branches (fig. B.2a).

Rule 2 Two branches in parallel entering one common node may be combined into a single branch whose coefficient is the sum of the coefficients of the two branches (fig. B.2b).

Rule 3 If a node has a self-loop (ie a branch which begins and ends on that node), a self-loop may be eliminated by dividing the coefficients of every other branch entering that node by $(1 - S_{nn})$, where S_{nn} is the coefficient of the self-loop (fig. B.2c).

Rule 4 A node may be split into two nodes, which are subsequently treated as separate nodes, provided the resulting flow graph contains once, and only once, every combination of separate input and output branches that connect to the original node. In splitting the node, each of the two nodes must have at least one input and one output branch. If the original node has a self-loop attached to it, this must be attached to each of the separate nodes formed in the duplication.

An example of node splitting is given in fig. B.2d.

A more detailed introductory discussion together with proofs of these four rules has been given by Adam, 1969[5].

On using the above rules to solve the flow graph of an energy level system, the node representing the level whose population is being calculated must not be split or eliminated.

To calculate the population of the lower level in fig. B.1a, rule 4 is first used to split node 1 into two separate nodes (fig. B.3a). Then the application of rule 1 followed by rule 2 leads to the flow graph shown in fig. B.3b. By inspection of this flow graph the pumping rate of the lower level can be written down as $(R_1 f_{12} + R_2)$. The population of the level is therefore $\tau_2(R_1 f_{12} + R_2)$ where τ_2 is the level lifetime.

B4. Analytical Method of Solution

The analytical method for the solution of flow graphs has been discussed by Lorens, 1956[4]. The procedure involves two main steps:
(a) recognising all the paths between the external pumping processes and the node representing the population under investigation; and
(b) recognising all the loops of various orders in the flow graph.
To illustrate the analytical method of solution we consider the three level system shown in fig. B.4a, with its associated flow graph fig. B.4b.

A path is defined as a collection of consecutive branches in series (and all in the same direction) that connects the node under investigation to an external pumping process. A particular path must pass only once through each node involved, and the value of a path is the product of the coefficients of all the branches involved. In the flow graph of fig. B.4b, there are three paths connecting the node representing level m to the external pumping processes; these are the path consisting of a single branch of value R_m, the path via node 1

of value $R_1 f_{1m}$, and the path via nodes 1 and 2 of value $R_2 f_{21} f_{1m}$.

A loop is a path which starts and finishes in the same node. In considering the topographical approach we have seen that loops are important (rule 3). It is now necessary to examine loops in more detail, and to introduce the definitions of first, second, and higher order loops.

A first order loop is defined as a loop that comes to a closure with no node passed more than once. Its value is given by the product of the coefficients of the branches making up the loop.

A second order loop is defined as being made from two first order loops that have no nodes in common (ie two non-touching first order loops), and its value is the product of the values of the two first order loops from which it is made up. (The loops making up a second order loop are still regarded separately as two first order loops.)

Third and higher order loops are similarly defined as being three or more non-touching, first order loops, and their values are again given by the product of the values of the first order loops from which they are made. Because the coefficients are necessarily less than unity, third and higher order loops can frequently be omitted as a first approximation.

A general expression relating the net pumping rate for any one node (level) in the flow graph to the external pumping processes is given by

$$R = \frac{\sum_n P_n \left(1 - \Sigma L(1)^{(n)} + \Sigma L(2)^{(n)} - \ldots. \right)}{1 - \Sigma L(1) + \Sigma L(2) - \Sigma L(3) + \ldots} , \qquad (B.1)$$

where P_n is the value of the nth path from an external pumping process to the node considered. The sum over n extends over all paths connecting the external pumping processes to the node; $\Sigma L(1)$ is the sum over the values of all the first order loops in the flow graph, $\Sigma L(2)$ is the sum

over the values of all the second order loops in the flow graph, etc: and $\Sigma L\,(1)^{(n)}$ is the sum over the values of all the first order loops in the flow graph not touching the nth path (ie having no nodes in common with the nth path), etc.

The loop occurring in fig. B.4b is the first order loop of value $f_{m1}f_{1m}$. It touches all three paths connecting node m to the external pumping processes. Equation B.1 can be applied directly to give the total pumping rate to level m as,

$$R = (R_m + R_1 f_{1m} + R_2 f_{21} f_{1m}) \;/\; (1 - f_{m1} f_{1m}).$$

Multiplication of this equation by the level lifetime (τ_m) gives the population of the level as

$$N_m = \tau_m \{R_m + (R_1 + f_{21} R_1) f_{1m}\} / (1 - f_{m1} f_{1m}). \qquad (B.2)$$

B.5 Flow Graphs for Closed Systems

In the above, we have examined the situation in which a group of energy levels is pumped by external pumping processes originating from outside the system. In this section the case in which all the pumping processes are between levels explicitly included in the system is considered. Under such a condition the populations are subject to the constraint

$$\sum_i N_i = N, \qquad (B.3)$$

where the sum extends over all energy levels in the system. The flow graph for such a system is closed.

If in the example given in fig. B.1a, the level from which pumping is taking place is included in the system, then the energy level diagram and flow graph are as shown in fig. B.5a, b. Since the level from which pumping occurs is now explicitly included, the pumping rates to the higher levels are described in the flow graph in terms of branching ratios (and not by pumping rates as previously).

The flow graph can now be solved to obtain the population of

any one level in terms of the population of any other level. Suppose that the population of level 2 in terms of the ground level population is required. A branch in the flow graph emanating from the ground level is opened, and the pumping rate associated with this branch (which involves the population of the ground level) is inserted. The flow graph therefore assumes the appearance of fig. B.6c. If the analytical method is used, then all paths and loops in the graph are identified after the appropriate branch has been opened. The population of level 2 may be obtained by applying either the analytical (equation B.1) or the topographical method to fig. B.5c. We obtain

$$\frac{N_2}{\tau_2} = \frac{N_0 r_{02}}{\tau_0} \frac{(f_{12} + f_{10}\, r_{02})}{(1 - r_{02}\, f_{20})} \qquad (B.4)$$

By opening up different branches it is possible to obtain the population of any one level in terms of any other level. Thus if branch f_{12} between node 2 and node 1 in fig. B.5b is opened, the populations of level 2 and of the ground level in terms of level 1 can be obtained. The use of a closed flow graph in analysing population inversions in laser systems is particularly appropriate, since the population of the upper laser level in terms of the population of the lower laser level can readily be extracted from the flow graph.

References (App. B)

1 Mason S J 1953 Proc IRE 41 1144 - 1156

2 Hunton J K 1960 Trans IRE MTT-8 206 - 212

3 Robichaud L P A, Boisvert M and Robert J 1962 Signal Flow Graphs and Applications (New Jersey : Prentice-Hall)

4 Kuhn N 1963 Microwave Journal November pp 59 - 66

Lorens C S 1956 A proof of the Nonintersecting Loop Rule for the solution of linear equations by flow graphs.Res Lab of Electronics MIT Cambridge Mass Quarterly Progress Report January pp 97 - 102

5 Adam S F 1969 Microwave Theory and Applications (New Jersey: Prentice-Hall) pp 86 - 106

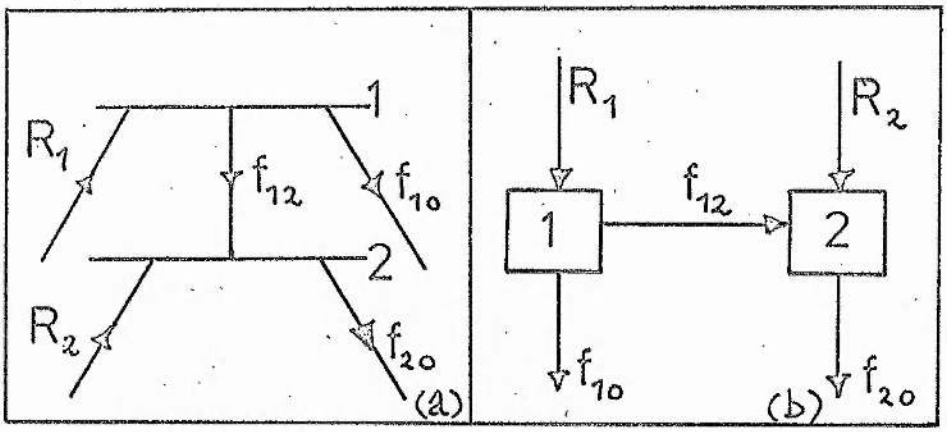

Figure B.1 (a) An open system of two energy levels; (b) flow graph for system .

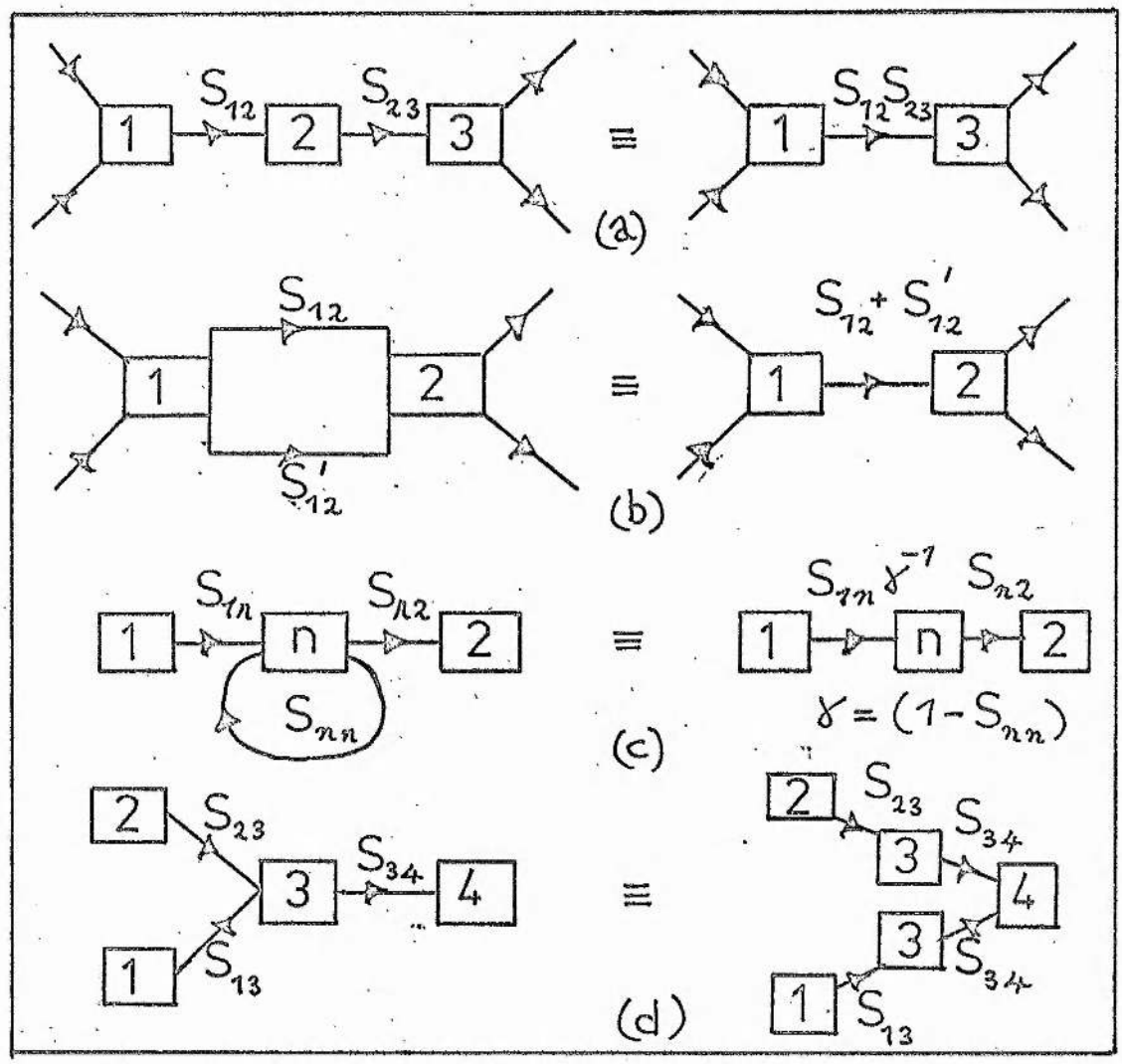

Figure B.2 Topographical rules: (a) branches in series, (b)branches in parallel, (c)elimination of self-loop, and (d)node splitting.

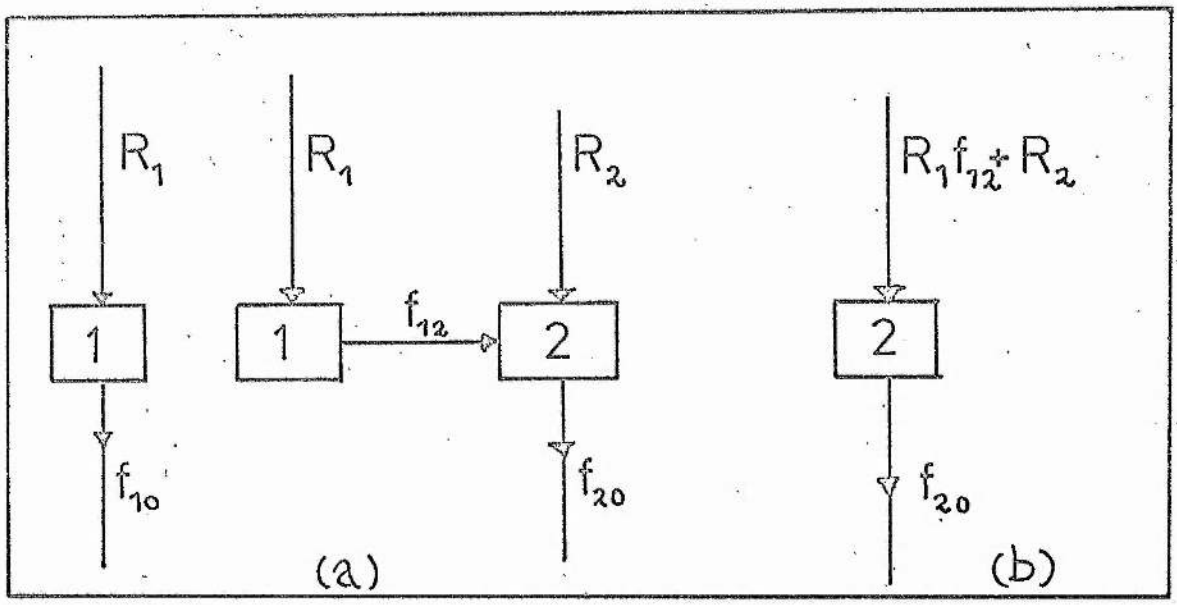

Figure B.3 (a) Application of rule 4 to split node 1 of the flow graph of fig. B.1 (b). (b) Application of rules 1 and 2 to the flow graph of (a).

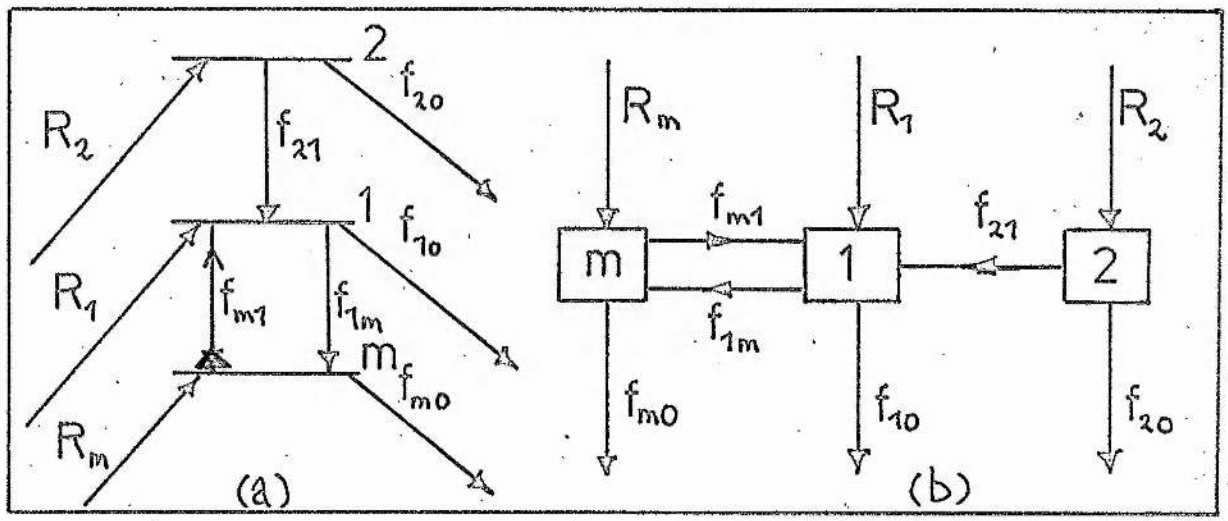

Figure B.4 (a) Coupling processes for three energy levels. (b) Flow graph for (a).

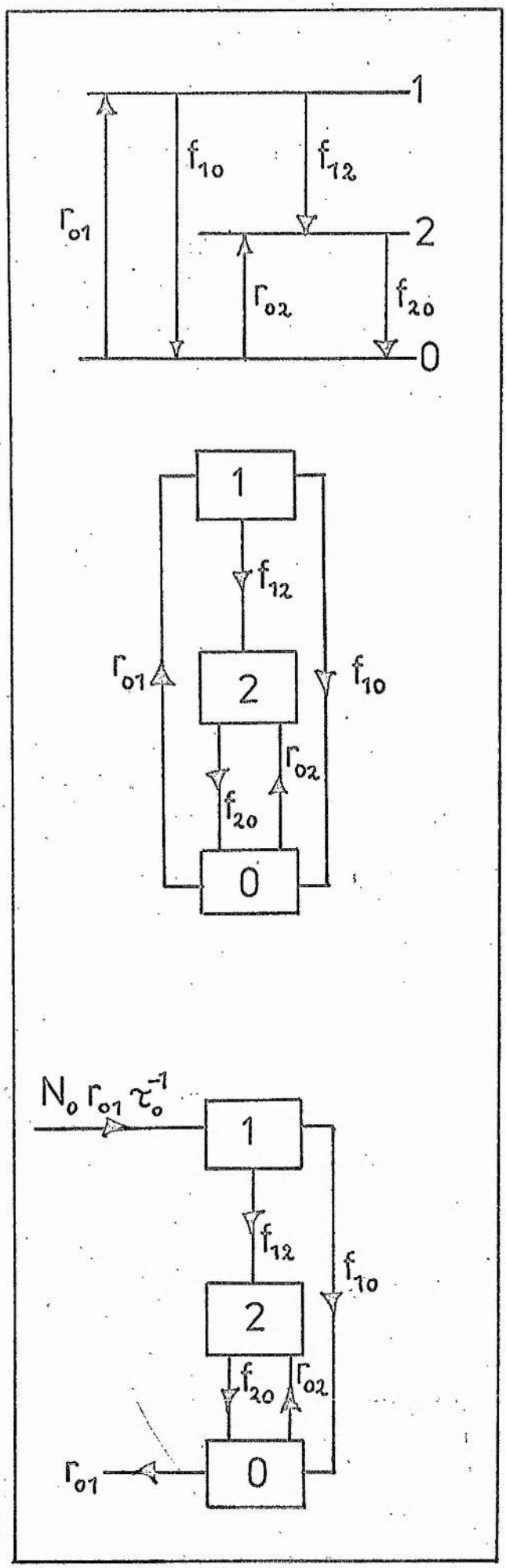

Figure B.5.

(a)A closed energy level system.

(b) Flow graph for (a)

(c)Closed flow diagram of (b) after cutting.